BETA-DECAY STUDIES OF NEUTRON-RICH NUCLIDES AND THE POSSIBILITY OF AN N = 34 SUBSHELL CLOSURE

By

Sean Nicholas Liddick

A DISSERTATION

Submitted to
Michigan State University
in partial fulfillment of the requirements
for the degree of

DOCTOR OF PHILOSOPHY

Department of Chemistry

2004

ABSTRACT

BETA-DECAY STUDIES OF NEUTRON-RICH NUCLIDES
AND THE POSSIBILITY OF AN N = 34 SUBSHELL CLOSURE

By

Sean Nicholas Liddick

An inspection of periodic trends in ionization energies is one manifestation of electronic shells in atoms. Analogously, trends observed in nuclear masses led to the development of the nuclear shell model. Areas of increased stability at the traditional magic nucleon numbers 2, 8, 20, 28, 50, 82, and 126 have been associated with large energy gaps encountered in the filling of shell-model orbitals. The reordering of levels within the shell model is an important question in nuclear structure studies as it may lead to the development of new magic numbers far from stability.

The experimental characterization of the N = 32 subshell closure in Cr, Ti, and Ca isotopes stimulated shell model calculations, using a new effective interaction labeled GXPF1 [1], that also indicated the possibility of an N = 34 subshell closure in the $_{22}$Ti and $_{20}$Ca isotopes. The N = 32 and suspected N = 34 subshell closures were attributed to a strong proton-neutron monopole migration of the $\nu f_{5/2}$ state as protons are removed from the $\pi f_{7/2}$ level. One indication for the subshell closure at N = 34, predicted by GXPF1 calculations, is an energy of ∼1500 keV for the the first excited 2_1^+ state in ^{56}Ti, similar to the energy of the 2_1^+ state in ^{54}Ti at the N = 32 subshell closure.

β decay studies have been performed at the National Superconducting Cyclotron Laboratory on neutron-rich pf-shell nuclides to investigate the possibility of a subshell closure at N = 34. The nuclides that were studied included ^{56}Sc, ^{57}Ti, ^{58,59}V, and ^{60}Cr and were produced through the fragmentation of a 140 MeV/nucleon ^{86}Kr beam on a ^{9}Be target. The nuclides were implanted into a Double-sided Si Strip Detector which was used to detect both implanted ions and decays. Decays were correlated with implanted ions on an event-by-event basis and γ rays were monitored with 12

detectors from the Segmented Germanium Array. For all nuclides studied, half-lives and level schemes were deduced.

The experimental study focused on the β decay of ^{56}Sc, to determine the energy of the 2_1^+ state in $^{56}_{22}$Ti$_{34}$. A value of 1129 keV was determined for the energy of the $2^+ \rightarrow 0^+$ transition in ^{56}Ti, 400 keV lower than predicted, suggesting the absence of a shell closure in the $_{22}$Ti isotopes. The ground state J$^\pi$ assignments for ^{56}Sc and ^{57}Ti along with other nuclides around the N = 32 subshell closure were used to infer the migration of the neutron $f_{5/2}$ state with the removal of protons from the $f_{7/2}$ level using an extreme single-particle model. While the migration of the $f_{5/2}$ agrees qualitatively with calculations, the increase in energy of the $\nu f_{5/2}$ with the removal of protons from the $f_{7/2}$ seems to be overestimated in GXPF1. However, there still exists the possibility that with the removal of the last two protons from the $f_{7/2}$ state, the N = 34 subshell closure develops.

ACKNOWLEDGMENTS

First, I would like to thank my advisor Paul. Without his assistance this dissertation would not have been possible.

I would also like to thank all the members of the beta group for their willingness to help run the beta decay experiment that this dissertation is based on and for the numerous discussions on data analysis that followed.

My fellow graduate students at the lab were also invaluable during my time at the lab. I would be remiss if I did not specifically mention both Bryan and Jeremey. Both of them listened to the numerous problems that were encountered along the way to graduation and both have helped put things into perspective when things seemed overwhelming. Jeremey, I'm sorry to say that there is no personal anecdote anywhere in this dissertation. Thank you Bryan for always giving me an audience practice talks. I'm sure that after listening to my Sc-56 talk more than a dozen times you might be able to write about the beta decay of Sc-56.

Finally I wouldn't have been able to make it had it not been for the constant support from my wife (who is extremely excited about being mentioned in this document and is now jumping up and down) and family. They always had encouraging words, especially when it seemed that the dissertation was always just a few days from being finished.

Contents

List of Figures

List of Tables

Chapter 1

Introduction

1.1 Description of Shell Closures

Discontinuities observed in the ionization energies of atomic electrons as a function of Z, shown in Figure 1.1, have been linked to the filling of electronic shells. After the filling of an electronic shell, the next valence electron is placed into a higher energy orbital decreasing the energy needed to remove the last electron from the atom. Thus, discontinuities in the ionization energies of atoms were correlated with the underlying "shell structure". In studies of the bulk properties of nuclei near the valley of stability, discontinuities in a number of different physical observables involving nuclear masses also suggested an extra stability of the nuclear system at 'magic' nucleon numbers of 2,8,20,28,50,82, and 126. For example, consider the one-neutron separation energies defined by

$$S_n(A, Z) = BE(A, Z) - BE(A - 1, Z) \tag{1.1}$$

where BE is the binding energy of a nucleus, A is the mass number and Z is the atomic number of the nuclide. From equation 1.1 we associate S_n with the energy necessary to remove a neutron from the nucleus. Similar to the atomic case, just after a magic number for an isotopic chain, a sudden drop in S_n is observed. The effect of the magic numbers on the neutron separation energy can be emphasized by taking differences

between one-neutron separation energies between neighboring isotopes, defined as

$$\Delta S_n = BE(A, Z) - BE(A - 1, Z) - [BE(A + 1, Z) - BE(A, Z)] \qquad (1.2)$$

where again BE is the binding energy, A and Z represent the mass number and atomic number of the nuclide, respectively. ΔS_n is shown in Figure 1.1 for all even-even nuclides up to $_{94}$Pu.

Theoretical attempts to reproduce the observed magic numbers gradually led to the development of the nuclear shell model. In contrast to the atomic case, where the electronic shell structure arises from the well known Coulomb potential created by the protons, the potential for the description of nucleons inside the nucleus was poorly understood and various models were tested in an attempt to explain the behavior. A few simple potentials were tried for the nuclear shell model, such as the harmonic oscillator and the square well, but these potentials were not realistic descriptions of the expected nuclear potential especially since both require the potential go to infinity at large radii. In spite of the infinite energy of the harmonic oscillator and square well potentials, both were able to reproduce the shell closures up to 20 and showed that the closures are associated with a large energy spacing between two different single-particle orbits. A more realistic potential approaches zero far from the nucleus, a condition fulfilled by a Woods-Saxon potential of the form:

$$V(r) = \frac{-V_0}{1 + e^{(r - R_0)/a}} \qquad (1.3)$$

where a is the diffuseness of the nuclear surface, R_0 is the mean nuclear radius, r is the distance from the center of the nucleus, and V_0 is the depth of the potential. While the Woods-Saxon potential is more realistic (V→0 at large r) it was still unable to reproduce the magic numbers observed above 20. The problem was finally solved with the introduction of a spin-orbit force that breaks the degeneracy between the pairs of states with $l > 0$ [3, 4]. The spin-orbit force results in the reduction in the
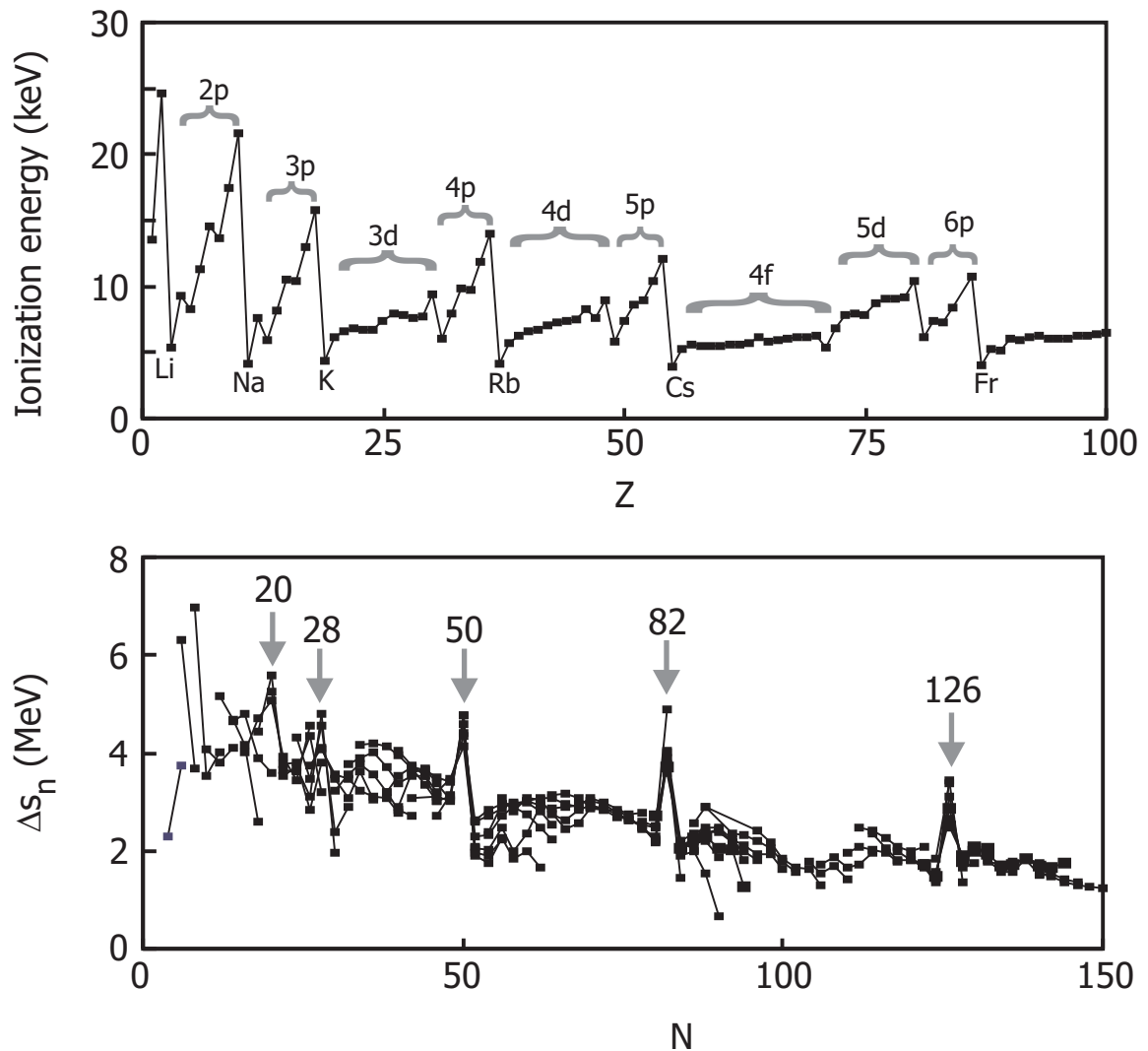
Figure 1.1: In the top of the figure, the ionization energy is plotted as a function of the atomic number. Large drops in the ionization energy occur following the filling of an atomic shell. The bottom part of the figure shows the differential neutron separation energies as a function of neutron number. Lines connect series of isotopes. The peaks located at the magic numbers suggest additional stability that can be associated with the filling of nuclear shells.
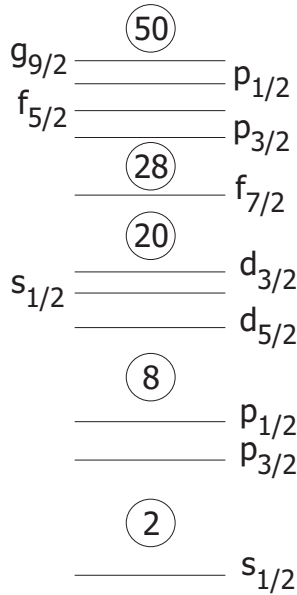
Figure 1.2: Nuclear shell structure up to nucleon number 50 for a Woods-Saxon potential with a spin-orbit interaction. Energies are not to scale and states are labeled by l and j.

energy of the $l+1/2$ state and reproduces the known shell closures. The shell structure described by the Woods-Saxon model with a spin-orbit force is shown in Figure 1.2 up to the nucleon number 50 shell closure [5]. For example, from Figure 1.2 the magic numbers at 28 and 50 are a result of the spin-orbit splitting between the $f_{7/2} - f_{5/2}$ and $g_{9/2} - g_{7/2}$, respectively.

Using the known shell closures, shell model calculations can be performed by dividing the nucleus into an inert core, containing most of the nucleons coupled to 0^+, and a small number of valence particles outside the core. An effective shell model interaction is developed for the valence nucleons to describe the nuclei in a specific region. In this manner, the nuclear shell model, schematically displayed in Figure 1.2, has proven to be very successful in the reproduction and prediction of nuclear properties close to the valley of β stability. It should not be assumed, however, that the relative energies between levels shown in Figure 1.2 are static. The possible rearrangement of single-particle levels is of great interest in shell structure studies and can result in the development of new magic numbers.

1.2   Reordering of Single Particle States

A significant reordering of single-particle states has been observed in nuclei close to stability in the N = 50-82 shell. The reordering involves the migration of the proton $g_{7/2}$ orbit in the Sb isotopes inferred from the shift in energy of the $7/2^+$ state as neutrons are added to fill the neutron $h_{11/2}$, see Figure 1.3 [6]. Notice that when neutrons are added to the $h_{11/2}$ state (beginning around N = 66) the energy of the $g_{7/2}$ state decreases and is reflected in the energy of the $7/2^+$ of Sb, which eventually becomes the ground state in $^{123}_{51}\text{Sb}_{72}$. The reduction in the energy of the $g_{7/2}$ single particle level has been attributed to an attractive proton-neutron monopole interaction, between the $\pi g_{9/2} - \nu h_{11/2}$ states, reducing the energy of the $g_{7/2}$ level by approximately 2 MeV across the Sb isotopes. This is an additional interaction on top of the spin-orbit interaction discussed above. While the monopole interaction is significant between the $\pi g_{9/2} - \nu h_{11/2}$ levels, as evidenced in the Sb isotopes, it is strongest when proton and neutron orbitals have similar values of orbital angular momentum, $l(\text{proton}) \sim l(\text{neutron})$ [7].

1.3   Observation of Shell Closures

In the single-particle picture shown in Figure 1.2, shell closures occur where there is a large energy difference between consecutive single-particle states. At a shell closure, a nucleus may be considered a spherical system with limited collective features at low excitation energies. The low-energy level structure of nuclei at shell closures can usually be described using single-particle excitations. However, as nuclei progress away from a shell closure, collective interactions (involving many nucleons at the same time) become more likely. Collective behavior in the proximity of shell closures, is associated with the vibration of the nuclear shape. At midshell, the highly collective system displays features that can be described as the rotation of a statically deformed nucleus. The increase in collectivity leads to the evolution of the nuclear shape from
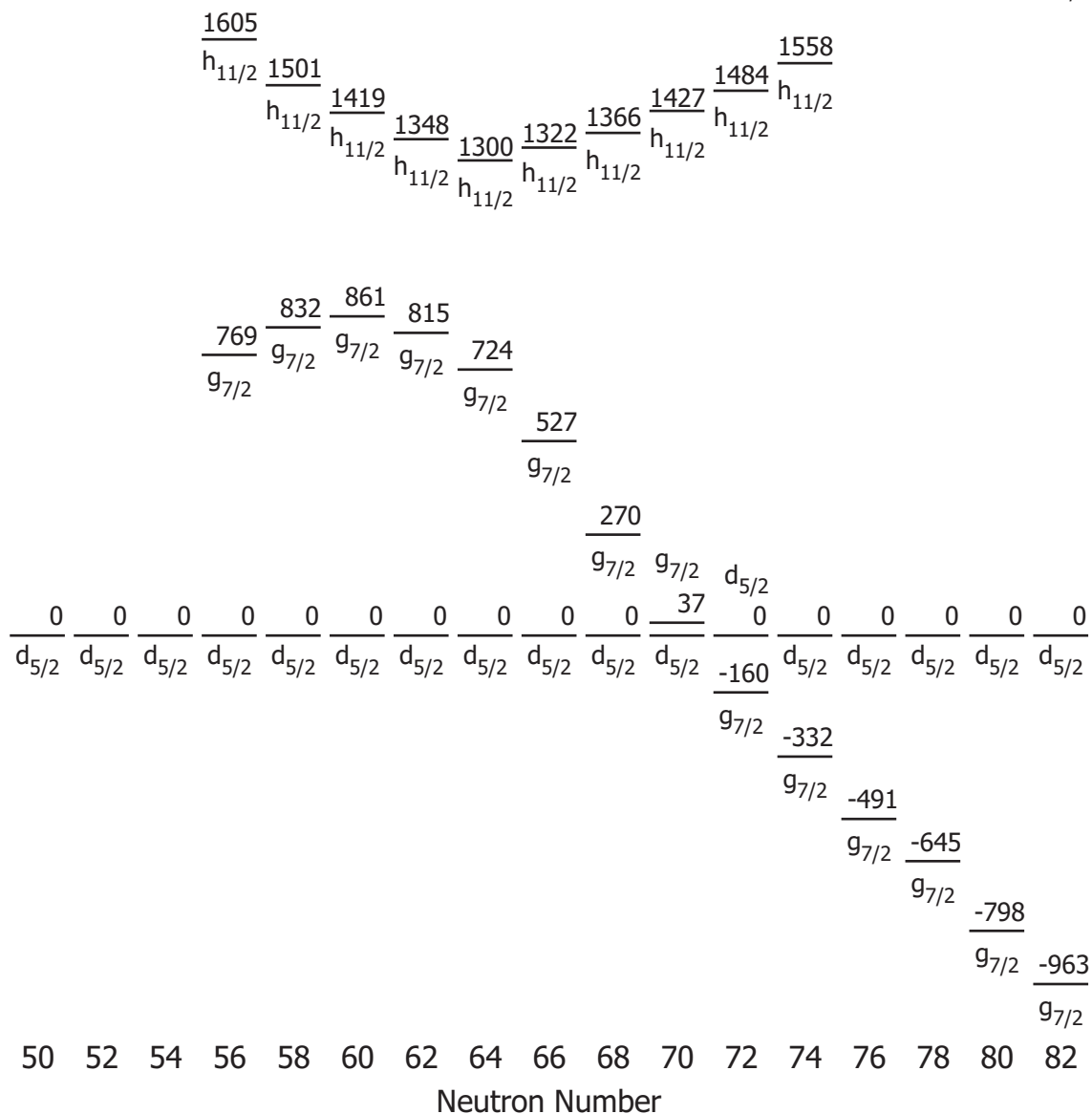
Figure 1.3: Migration of the $7/2^+$ state in Sb isotopes as a function of neutron number. Energies of the different states relative to the $d_{5/2}$ level were taken from experimental data. The migration is attributed to the proton-neutron monopole interaction between $\pi g_{7/2}$ and $\nu h_{11/2}$. As neutrons are added to the $h_{11/2}$, beginning around N = 66, there is a steady drop in the energy of the proton $g_{7/2}$ state.

spherical to a static deformation, resulting in either oblate (discus-like) or prolate (football-like) shapes. The static deformation can be characterized by the quadrupole deformation parameter, β_2. The sign of β_2 describes the shape of the nucleus with positive values associated with prolate shapes and negative values associated with oblate shapes. There exist a variety of different probes to measure the quadrupole deformation of the nucleus. For the current study the energy of the first excited 2^+ state, $E(2_1^+)$, in even-even nuclei will be used and, qualitatively, a higher $E(2_1^+)$ values for more rigid spherical nuclei is expected.

1.3.1 E(2_1^+)

The experimental signature for the possible presence of a shell closure used herein will be the energy of the first excited 2^+ state in even-even nuclei, $E(2_1^+)$. Globally, the $E(2_1^+)$ is a good indication of shell structure when compared systematically across a range of isotopes. The behavior of an $E(2_1^+)$ value can be related to the degree of collectivity in the nuclear system in a relatively simple way . At shell closures, the nucleons completely fill the single-particle levels below a large energy gap. To create a 2^+ state, a pair of nucleons must be broken and one nucleon promoted to a higher single-particle state across the energy gap due to the Pauli principle. This costs a considerable amount of energy, resulting in a high $E(2_1^+)$ value. Further from a shell closure, the configuration of the nucleons is more complicated with unfilled orbitals and the energy of the 2^+ state is lowered as a result of collective interactions among many nucleons and can be describes in terms of a vibration or, if a static deformation exists, a rotation of the nucleus.

Grodzins [8] developed the following empirical relation between the quadrupole deformation parameter, β_2, and $E(2^+)$

$$E(2^+) = \frac{1225 MeV}{\beta_2^2 A^{7/3}}$$
(1.4)
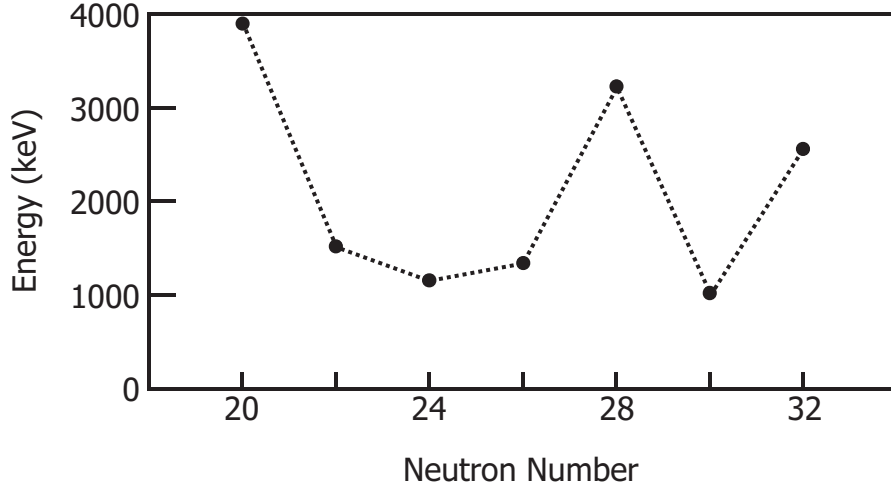
Figure 1.4: E(2^+) values in the $_{20}$Ca isotopes as a function of neutron number. The N = 28 shell closure and N = 32 subshell closure are revealed from a peak in the E(2^+) values.

where A is the mass number of the nuclide. As a shell closure is approached the nuclear shape becomes more spherical, β_2 decreases, and the E(2_1^+) increases. As a progression is made to the nuclei in the middle of a major shell collectivity increases and leads to a reduction in the E(2_1^+).

The E(2_1^+) values for even-even $_{20}$Ca isotopes are shown in Figure 1.4 as a specific example. Indications of the shell closures at N = 20,28 are observed in Figure 1.4 as peaks in the E(2_1^+) value. Also, in the neutron-rich Ca isotopes, there might be a smaller peak located at N = 32 [9]. The reduced height of the peak at N = 32 can be attributed to a subshell closure in which the energy separation between two consecutive single-particle orbits is significant but not as large as a shell closure. The existence of the N = 32 subshell closure, and the possibility of additional subshell closures in neighboring neutron-rich nuclei, is an interesting question since the development of a subshell closure would inhibit the onset of collectivity.

1.4 Proposed Measurement

The present study concentrated on the region of the chart of the nuclides shown in Figure 1.5. The region is centered above the Z = 20 proton closed shell and the N =
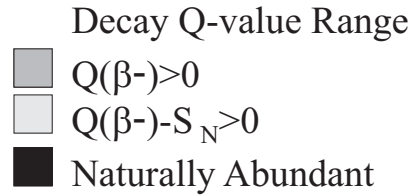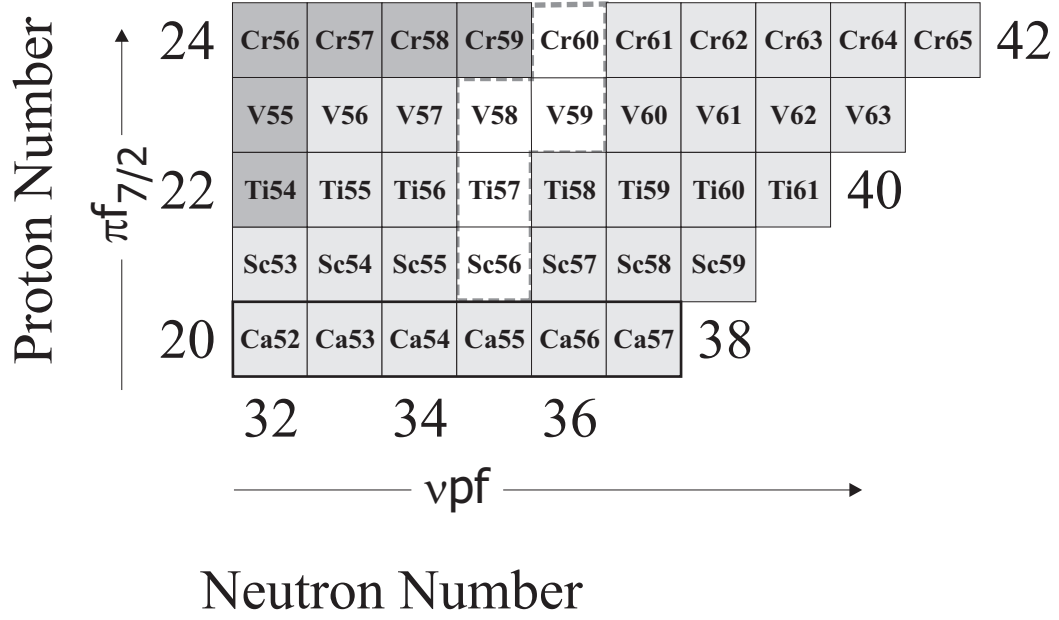
Figure 1.5: Chart of the nuclides focusing on the region around Z = 20 and N = 32. Nuclides available for study in this experiment are colored white and outlined with the dashed gray line. The five nuclides have a decay Q value that is greater than the neutron separation energy. Limited spectroscopic information was available for the nuclides in this region before the study presented here.

32 neutron closed subshell. The β decay of ^{56}Sc to levels in ^{56}Ti was investigated to determine $E(2_1^+)$ in ^{56}Ti at N = 34 and the possibility of a neutron subshell closure. In addition, new data on the β decays of ^{57}Ti, ^{58,59}V, and ^{60}Cr were obtained.

As mentioned in Section 1.2, the migration of the $\pi g_{7/2}$ state in the Sb isotopes was due to the monopole interaction between the $\pi g_{7/2}$ and $\nu h_{11/2}$ states, which have similar l values. The strongest proton-neutron monopole interaction occurs between nucleons in orbitals that are spin-orbit partners and may lead to a significant reordering of single-particle states far from stability. Due to the large spin-orbit splitting, this overlap is strongest in neutron-rich nuclei between the $\pi(l + 1/2)$ and $\nu(l - 1/2)$ single-particle states that lowers the energy of the $\nu(l - 1/2)$ level, possibly leading
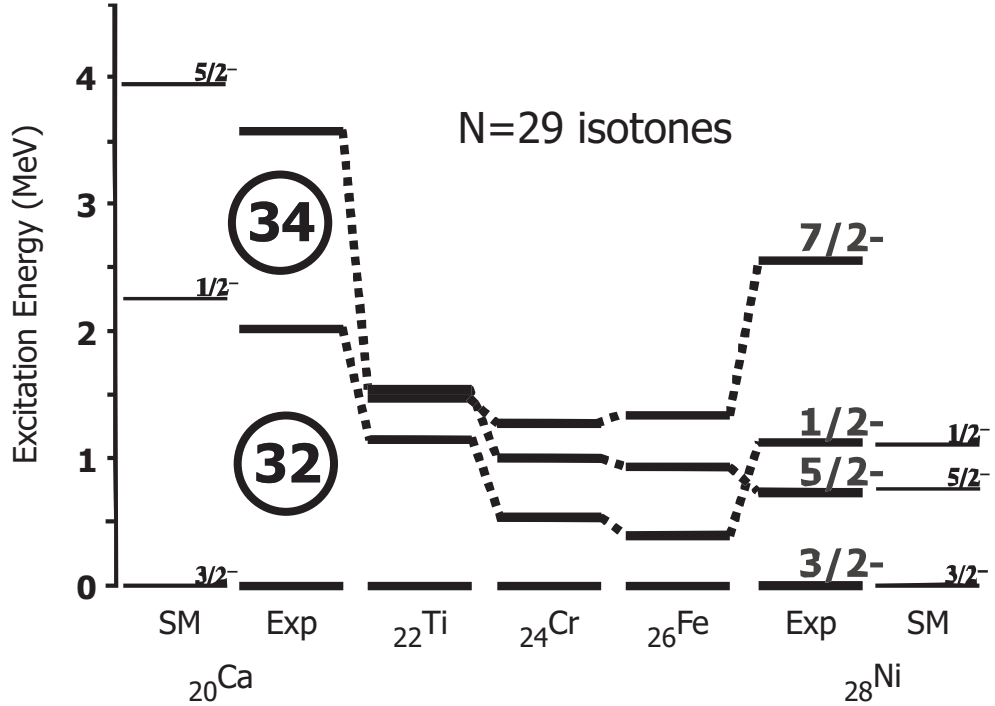
Figure 1.6: Low-energy level structure of N = 29 isotones. The energy of the $5/2^+$ state drops dramatically with the filling of the $\pi f_{7/2}$ level and is attributed to the proton-neutron monopole interaction between the $\pi f_{7/2}$ and $\nu f_{5/2}$ states.

to a dramatic reordering of single-particle states [10]. In the pf shell, the spin-orbit parnters $\pi f_{7/2} - \nu f_{5/2}$ are ideal candidates for the development of novel shell structure far from stability. The low-energy structure of neutron-rich nuclei with nucleons occupying the proton $f_{7/2}$ state and neutron $f_{7/2}$, $p_{3/2}$, $f_{5/2}$, $p_{1/2}$ orbitals, shown in Figure 1.6, is dramatically affected by the strong and attractive proton-neutron monopole interaction between the spin-orbit partners $\pi f_{7/2}$ and $\nu f_{5/2}$. As protons are added to the $\pi f_{7/2}$ orbital, going from $_{20}$Ca to $_{28}$Ni, the effective single-particle energy of the $\nu f_{5/2}$ orbital decreases significantly relative to the $\nu p_{3/2}$ state. The lowering in energy of the $\nu f_{5/2}$ orbital, in combination with the large spin-orbit splitting between the $\nu p_{3/2}$ and $\nu p_{1/2}$ levels, is suggestive of a subshell gap at $N = 32$ for nuclides in which the $\pi f_{7/2}$ orbital is occupied by four or fewer protons.

In addition to the E(2^+) value for $^{52}_{20}$Ca, discussed in the previous section, the masses [11] of the Ca isotopes suggested added stability and provided early evidence for a subshell closure at $N = 32$. However, systematic data for isotopes beyond

10

^{52}Ca are unavailable, and it was believed that the appearance of a subshell gap at $N = 32$ was reinforced by the proton shell closure at $Z = 20$. Experimental evidence for a potential subshell closure at $N = 32$ for the $_{24}$Cr isotopes was reported in Ref. [12], based on the systematic variation of $E(2_1^+)$ in the even-even Cr isotopes. The value $E(2_1^+) = 1007$ keV of ^{56}Cr$_{32}$ is more than 100 keV above that observed in the neighboring ^{54,58}Cr nuclei.

The systematic variation of $E(2_1^+)$ along the $N = 32$ isotonic chain was recently completed for the $\pi f_{7/2}$ nuclides with the determination of $E(2_1^+) = 1495$ keV for ^{54}Ti [13]. The increase in $E(2_1^+)$ from $_{24}$Cr to $_{20}$Ca with removal of protons from the $f_{7/2}$ orbital, parallels the expected growth of the single-particle energy gap at $N = 32$ due to the monopole migration of the $\nu f_{5/2}$ orbital (see Figure 1.6). The data available for the higher-spin states in even-even ^{50,52,54}Ti isotopes provide additional evidence for the $N = 32$ gap [13]. In ^{54}Ti, the significant spacing between the 6_1^+ state at 2936 keV and the cluster of levels 8_1^+, 9_1^+, and 10_1^+ at ~ 5800 keV suggests that a substantial energy gap must be overcome when promoting one of the coupled $\nu p_{3/2}$ neutrons to either the $\nu p_{1/2}$ or the $\nu f_{5/2}$ level.

It was predicted [14] that the continued monopole shift of the $\nu f_{5/2}$ orbital may also lead to the development of a shell closure at $N = 34$, and that the low-energy structure of ^{54}Ca may be similar to that of ^{48}Ca, which is doubly-magic. The shell model calculations by Honma et al. employed a new effective shell model interaction, designated GXPF1. The GXPF1 calculations have been successful in reproducing the experimental E(2_1^+) values in the neutron-rich $_{20}$Ca, $_{22}$Ti and $_{24}$Cr isotopes, as shown in Figure 1.7, including the systematic increase in E(2_1^+) at N = 32. The onset of an $N = 34$ shell closure was first expected to be evident in the Ti isotopes, where $E(2_1^+)$ for ^{56}Ti$_{34}$ was predicted to lie at approximately 1500 keV, similar in energy to its neighbor ^{54}Ti$_{32}$, see Figure 1.7.

The current experimental study focused on the measurement of E(2_1^+) in ^{56}Ti$_{34}$, populated following the β decay of ^{56}Sc to test for evidence of a new subshell at
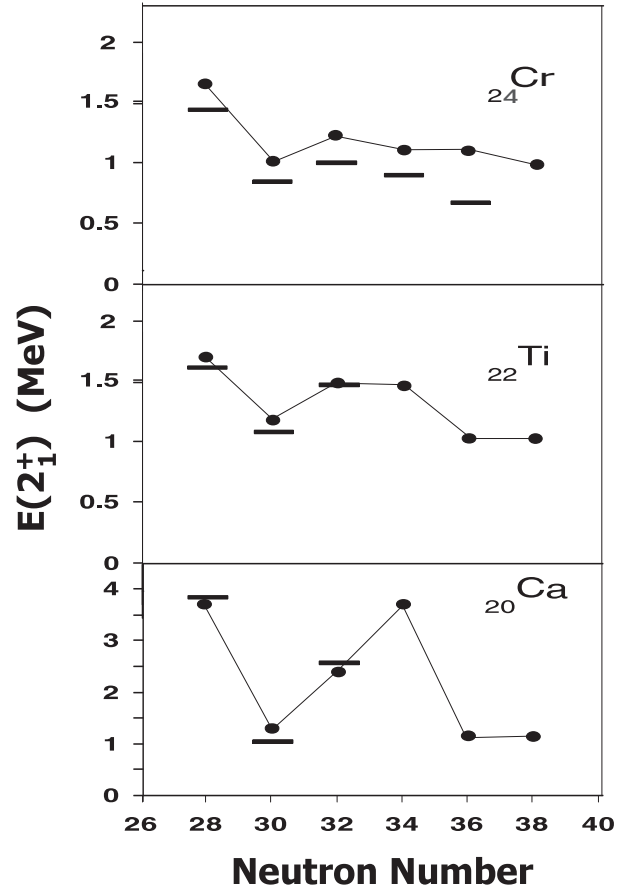
Figure 1.7: $E(2^+)$ as a function of neutron number for the $_{24}$Cr, $_{22}$Ti, and $_{20}$Ca isotopes. The circles connected by lines represent GXPF1 calculations and the black bars are experimental points. GXPF1 predicts a shell closure at N = 34 in the Ti and Ca isotopes evidenced by the systematic behavior of the calculated $E(2_1^+)$ values.

N = 34 for neutron-rich nuclides. Details regarding the study are provided in this dissertation, and are organized in the following manner. A review of the different decay paths for a neutron-rich parent nuclide are given in Chapter 2. A description of the experimental endstation for the detection of implanted ions, β and γ decays is given in Chapter 3. Also included in Chapter 3 is a description of the calibration of the both β and γ detectors, the correlation between implanted ions and decays and the electronic system used during the experiment. The results from the analysis of the β decay of ^{56}Sc, along with the β decays of ^{57}Ti, ^{58,59}V, and ^{60}Cr, are given in Chapter 4. A comparison between experimental results and calculated level structures is given for ^{56}Sc and ^{57}Ti in Chapter 5. The tentative ground state spins and parities of nuclides around the N = 32 subshell closure are analyzed in an attempt to describe the monopole migration of the $\nu f_{5/2}$ state as a function of proton number in the $f_{7/2}$ in Chapter 5. The conclusions and outlook are given in Chapter 6.

Chapter 2

Technique

The primary purpose of this study was to measure the $E(2_1^+)$ of ^{56}Ti to determine the possible presence of an N = 34 subshell closure as discussed in the previous chapter. The $E(2_1^+)$ values for even-even nuclei can be measured using a variety of different methods including Coulomb excitation [15], direct reactions [16], and deep-inelastic reactions [13]. For the present study, β decay was used to selectively populate the low-spin states in an even-even daughter nuclide. A parent nuclide was produced and its β decay was monitored. The β decay may populate excited nuclear states in the daughter and these daughter states can then decay through γ-ray emission, internal conversion, or if energetically allowed, through the emission of a neutron. The observation of the secondary radiation is used to construct a decay scheme for the parent nuclide into the different daughter states using absolute γ-ray intensities and $\gamma\gamma$ coincidence information.

2.1 β decay

β decay involves the weak-decay process of converting a neutron (proton) into a proton (neutron) keeping the mass number constant. Concomitantly, an energetic electron (β particle) and a low mass electrically neutral particle, called a neutrino, are emitted.

β decay collectively refers to three distinct decay processes listed below:

$$\beta^- \quad : \quad {}^{A}_{Z}X_N \rightarrow {}^{A}_{Z+1}Y_{N-1} + \beta^- + \overline{\nu} + Q_\beta \tag{2.1}$$

$$\beta^+ \quad : \quad {}^{A}_{Z}X_N \rightarrow {}^{A}_{Z-1}Y_{N+1} + \beta^+ + \nu + Q_\beta \tag{2.2}$$

$$\text{Electron Capture} \quad : \quad {}^{A}_{Z}X_N + e^- \rightarrow {}^{A}_{Z+1}Y_{N-1} + \nu + Q_\beta \tag{2.3}$$

where e^- is an atomic electron, $\beta^\pm$ is a beta particle, ν is a neutrino, and $\overline{\nu}$ is an anti-neutrino. Q_β is the characteristic amount of energy released in a specific β decay process and represents the difference in mass-energy between the initial and final states. If Q_β is positive the decay is energetically possible. To the neutron-deficient side of the valley of stability both β^+ and electron capture processes occur, though for a specific nucleus both may not be energetically possible because the emission of a β^+ has a threshold of 1.022 MeV.

During an electron capture process, a proton captures one of the atomic electrons converting a proton into a neutron. Along with the conversion, a mono-energetic neutrino is emitted. The capture of an atomic electron leaves a vacancy in one of the lower electronic shells, typically the K shell. The hole in the atomic shell left by the capture process is unstable and the electrons quickly reconfigure. The reconfiguration leads to detectable X-rays and Auger electrons. Though it is probable that neutrinos have some mass, it is very small [17, 18] and even so the neutrino escapes undetected from most experimental apparati due to the low weak interaction cross section; therefore, the identification of electron capture decay must be followed by tracking the secondary emission of X-rays or Auger electrons.

Whenever, the mass difference between initial and final states exceeds twice the mass of an electron (1.022 MeV) β^+ decay becomes possible. During β^+ decay, a proton is converted to a neutron, similar to the electron capture process, with the emission of a neutrino and β^+ particle. The β^+ will interact electromagnetically with the medium after emission gradually losing energy and slowing down. Once the β^+

particle has reached thermal energies it will quickly combine with an electron and annihilate, producing two 511-keV γ rays propagating in opposite directions. The β^+ decay can be followed both through detecting the energy deposited in a detector by the β^+ itself or by detecting the annihilation γ rays.

For the current work, β^- decay was the decay mode of interest. β^- decay occurs on the neutron-rich side of stability in which the weak interaction converts a neutron into a proton with the emission of a β^- particle and an anti-neutrino. The decay is observed by detecting the emission of the β^-, as it will interact electromagnetically with the electrons of the detection material. Since β emission is a three body process, the total Q_β value for the reaction is equally shared between the daughter nucleus, β^- particle, and neutrino. This results in a β particle energy spectrum that extends from zero to the Q_β value (minus a small amount of energy for the mass of the neutrino and the nuclear recoil). For the decays in the present study, the Q_β values are typically around 10 MeV. With such a large Q_β value, it is difficult to stop the electron in the detection system, and the possibility of undergoing β delayed neutron emission appears.

Important information obtained by monitoring the β activity is the rate constant, λ, of the decaying nuclides from which the half-life can be determined. An expression for the half-life as a function of λ can be derived using the first order rate law.

$$\frac{d[N]}{dt} = -N\lambda \tag{2.4}$$

$$\frac{N}{N_0} = e^{-\lambda * t} \tag{2.5}$$

where t is time, N_0 is the number of nuclei at time zero, and λ is the rate constant. At a value of $N/N_0 = 1/2$ the half-life is

$$t_{1/2} = \frac{\ln 2}{\lambda}.$$

β decay is useful as a spectroscopic tool owing to the selectivity of the decay process. Angular momentum must be conserved during the transition between the initial and final states in the β decay process leading to a restrictive set of selection rules. Note that both of the created particles have an intrinsic spin, S=1/2. If the β particle and neutrino are emitted with zero orbital angular momentum, $l = 0$ (the so-called allowed approximation), then only the intrinsic spins of the β particle and neutrino need to be considered in the transition between initial and final states. If the spins of the β particle and neutrino are anti-parallel (S=0), the total change in nuclear spin, ΔJ, between initial and final states must be 0 and the β decay is termed Fermi decay. If the electron and neutrino are emitted with their spins aligned (S=1), called Gamow-Teller decay, then $\Delta J = 0,1$. In both Fermi and Gamow-Teller decays, the condition $l = 0$ means that the parities of the initial and final states must be the same, following the condition $\Delta \pi = (-1)^l$, where π is the parity of the system. If the β particle and neutrino are emitted with $l \neq 0$, the decay is classified as "forbidden". Unlike the name suggests, "forbidden" decays can occur, just with a much smaller probability than allowed decays.. Each value of l results in a higher order of forbiddenness. The first, second, third,... forbidden decays result from the β particle and neutrino emitted with $l = 1, 2, 3, \ldots$ respectively. For each forbidden decay, both Fermi and Gamow-Teller types can occur, and the parity change between initial and final states may not be the same. For example, the first forbidden decay involves $l = 1$. If the β particle and neutrino are emitted with spins anti-aligned (Fermi type) then ΔJ=0,1. If the spins of the two emitted particles are aligned (Gamow-Teller type) then ΔJ=0,1,2. In both cases the parity must change between initial and final states because $l = 1$ in both cases. The probability of undergoing each successive level of forbidden decay decreases by a factor of about 10^4. The selection rules for β decay are summarized in Table. 2.1

If the β decay branching ratio to a particular daughter state is known then the

Table 2.1: β decay selection rules for allowed and forbidden transitions from Ref. [19]. Logft ranges taken from Ref. [5].

Type	ΔJ	$\Delta\pi$	logft
Allowed	0,1	no	3.5-7.5
First Forbidden	0,1,2	yes	5-19
Second Forbidden	1,2,3	no	10-18
Third Forbidden	2,3,4	yes	17-22
Fifth Forbidden	3,4,5	no	22-24

partial rate constant of the β decay transition to that state can be determined from

$$\lambda_i = BR_i * \lambda_t \tag{2.6}$$

where λ_i is the partial rate constant to state i, BR_i is the branching ratio to state i, and λ_t is the total decay rate. The sum over all partial rate constants, λ_i, equals the total rate constant. The partial half-life to state i can be calculated from

$$T_{1/2}^{partial} = \frac{\ln 2}{\lambda_i}. \tag{2.7}$$

From the partial half-life a comparative half-life, ft, where t is in seconds, can be calculated, where f is the "Fermi" function related to the shape of the β spectrum that arises from the differing atomic numbers of the daughter and the endpoint energy, allowing a comparison of different β decay transitions. The comparative half-life can be used to gauge the level of forbiddenness in a given β transition, but should not be considered absolute. While compilations exist for finding log$f$ values, a purely empirical equation for the calculation of log$f$ is [20]:

$$\log f_{\beta^-} = 4.0\log E_0 + 0.78 + 0.02Z - 0.005(Z-1)\log E_0 \tag{2.8}$$

where E_0 is the β-decay energy and Z is the atomic number of the daughter nuclide.

As the value of the comparative half-life can extend over many orders of magnitude, the number frequently reported is logft. The logft value associated with different

types of decays are shown in Table. 2.1.

2.1.1 β-delayed neutron decay

Neutron decay is the emission of a neutron from the nucleus under study. The equation
for such a decay is:

$$^A_Z X_N \rightarrow^{A-1}_Z X_{N-1} + \text{n} + Q_n \tag{2.9}$$
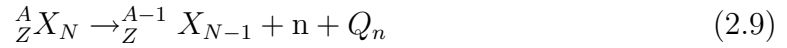
The Q_n value for the reaction is again the mass-energy difference between the initial
and final products. The neutron separation energy is defined as the negative of the
Q_n value when the product is left in its ground state. The neutron separation energy
is a positive number for all bound nuclei so that neutron decay from the ground
state is not possible. As neutrons are added to the nucleus the neutron separation
energy decreases. When the separation energy reaches zero it is not possible to bind
an additional neutron to the nucleus, and if a neutron is added, the nucleus will
undergo spontaneous neutron emission. However, in a β^- decay with a large Q_β value
it may be possible to populate excited states in the daughter nucleus that are above
the neutron separation energy. Such states could then decay by neutron emission
and this process is called β-delayed neutron emission. Neutron emission occurs via
the strong, or nuclear, interaction and competes very favorably with electromagnetic
decay. The neutron decay can populate states in the $^{A-1}$X daughter which may then
undergo electromagnetic decay typical of that nucleus.

2.2 γ decay

Following a β decay, the daughter nucleus may be left in an excited state. The excited
state will generally decay to the ground state through the emission of one or more
γ rays. The emission of γ rays results from a change in either the charge or current
distribution of the nucleus giving rise to an electric or a magnetic moment, respec-

tively. Thus, γ ray emission can be classified as electric or magnetic in character. γ rays, like β particles, carry off angular momentum from the excited nuclear state and must satisfy the relation

$$|J_i - J_f| \le \lambda \le J_i + J_f \tag{2.10}$$

where λ is the multipolarity of the transition and J_i and J_f are the spins of the initial and final states, respectively.

The change in parity, $\Delta\pi$, between initial and final states depends on the electric (E) or magnetic (M) character of the transition and the angular momentum involved as:

$$\Delta\pi(E\lambda) = (-1)^\lambda \tag{2.11}$$

$$\Delta\pi(M\lambda) = (-1)^{\lambda+1} \tag{2.12}$$

The transition rates, $\mathcal{W}$, of an electric or magnetic γ-ray transition are summarized in the following pair of equations [19]:

$$\mathcal{W}(E\lambda) = \alpha\hbar c \frac{8\pi(\lambda+1)}{\lambda[(2\lambda+1)!!]^2} \frac{1}{\hbar c} (\frac{E_\gamma}{\hbar c})^{2\lambda+1} B(E\lambda) \tag{2.13}$$

$$\mathcal{W}(M\lambda) = \alpha\hbar c (\frac{\hbar c}{2M_p c^2})^2 \frac{8\pi(\lambda+1)}{\lambda[(2\lambda+1)!!]^2} \frac{1}{\hbar c} (\frac{E_\gamma}{\hbar c})^{2\lambda+1} B(M\lambda) \tag{2.14}$$

where B(Eλ) and B(Mλ) are the reduced electric and magnetic transition probabilities that contain information on the initial and final nuclear wavefunction, c is the speed of light, α is the fine structure constant, M$_p$ is the mass of a proton, and $\hbar$ is Plank's constant divided by 2π.

It is useful to obtain some simple estimates for the values of the reduced transition probabilities, B(Eλ) and B(Mλ), but this requires a model of the nucleus. Adopting an extreme independent particle model, and assuming that the γ radiation involves the transition of one nucleon from an initial to a final single-particle state, the reduced

Table 2.2: γ transition rates and Weisskopf single particle estimates for the reduced transition probabilities from Ref. [19].

λ	$\mathcal{W}(E\lambda)$	$\mathcal{W}(M\lambda)$
1	$1.02\times10^{14}A^{2/3}E_\gamma^3$	$3.15\times10^{13}E_\gamma^3$
2	$7.28\times10^7A^{4/3}E_\gamma^5$	$2.24\times10^7A^{2/3}E_\gamma^3$
3	$1.02\times10A^2E_\gamma^7$	$1.04\times10A^{4/3}E_\gamma^3$
4	$1.02\times10^{-5}A^{8/3}E_\gamma^9$	$3.27\times10^{-6}A^2E_\gamma^3$
5	$1.02\times10^{-12}A^{10/3}E_\gamma^{11}$	$7.36\times10^{-13}A^{8/3}E_\gamma^3$

transition probabilities can be calculated as:

$$B_w(E\lambda) = \frac{1}{4\pi}(\frac{3}{\lambda+3})^2(1.2)^{2\lambda}A^{2\lambda/3}e^2 fm^{2\lambda} \tag{2.15}$$

$$B_w(M\lambda) = \frac{10}{\pi}(\frac{3}{\lambda+3})^2(1.2)^{2\lambda-2}A^{(2\lambda-2)/3}\mu_N^2 fm^{2\lambda-2} \tag{2.16}$$

where μ_N is the nuclear magneton, λ is the multipolarity, and A is the mass number. Equations 2.15 and 2.16 are called the Weisskopf single-particle estimates for the reduced transition probabilities. Table. 2.2 lists the transition rates for different electric and magnetic multipoles using the Weisskopf single-particle estimate for the reduced transition probability.

For a given γ transition, it is possible that several multipole radiations may be emitted. From the estimated transition rates shown in Table 2.2 it can be seen that the lowest multipole γ transition will dominate the decay. Secondly, it is possible for transitions to be of mixed type with magnetic and electric transitions, but the only prominent case is when a mixed M1/E2 transition is possible.

2.2.1   Internal Conversion

A competing process to γ-ray emission that may be significant for low energy transitions or transitions involving a high value of λ is internal conversion. Internal conversion occurs when the electromagnetic fields responsible for the emission of a photon interact with one of the atomic electrons resulting in its emission from the atom with-

out creation of a photon. In contrast to β decay, the electron is not created during the decay process, but is a preexisting atomic electron. The energy of the emitted electron will equal the decay energy minus the binding energy of the electron. It is possible to emit electrons from different atomic shells, and a measurement of the relative probabilities of emitting conversion electrons from different atomic shells is one way to determine the multipolarity of the transition involved. The probability of internal conversion will increase if: Z is increased, the energy of the decay is decreased, or the multipolarity of the transition is increased. The probability of internal conversion for a particular decay is defined by the internal conversion coefficient, α.

$$\alpha = \frac{\lambda_e}{\lambda_\gamma} \tag{2.17}$$

where λ is the rate of decay of each radiation type, defined as $0.693/t_{1/2}^{partial}$. The internal conversion coefficient can vary between 0 and ∞. An important case of internal conversion occurs in transitions between 0^+ states. Since $\lambda = 0$ and $\Delta\pi = (-1)^0 = +1$, these are E0 transitions. In such transitions, γ emission can not occur and the decay must proceed through internal conversion or pair production.

2.3 Application

β-delayed γ-ray spectroscopy was utilized to investigate evolution of shell structure around the $N = 32$ and the suspected $N = 34$ subshell closure. Parent nuclides were produced and the β decay into daughter states was observed. From the selectivity of the β transition, daughter states were populated if they satisfy the relation $\Delta J = 0, 1$ with the same parity. Detection of the delayed γ rays enabled the determination of the excited nuclear states in the daughter, in particular, the energy of the first excited 2_1^+ state was determined giving an indication on the possible existence of shell closures in the region of study. β-delayed neutron emission was detected through the observation

of γ rays in the A-1 mass chain with respect to the nuclide being examined. Internal conversion was not directly observable but needed to be considered, especially for low-energy transitions as the process will reduce the observed γ-ray intensity. The β decay to, and the energies of, excited nuclear states in the daughter provided information on the underlying nuclear shell structure in this region of exotic nuclei. The next chapter will focus on the method of production for the parent nuclides and the instrumentation used for the $\beta\gamma$ measurements.

Chapter 3

Experimental Setup

3.1 Isotope Production and Delivery for Experiment NSCL-02004

Except for the few long-lived natural radioactive elements, such as U and its radioactive daughters, radioactive isotopes must be artificially produced on earth. At the National Superconducting Cyclotron Laboratory (NSCL), radioactive isotopes are produced using the projectile fragmentation method. In this method, a very fast projectile is impinged onto a target and a fraction is converted into one of a myriad of reaction products. The reaction products, both stable and radioactive, emerge from the target with large forward momenta and are analyzed to select only the nuclides of interest.

The primary purpose of the current experiment was to study the β decay of ^{56}Sc. ^{56}Sc was produced using the projectile fragmentation of a primary ^{86}Kr beam. The ^{86}Kr beam was extracted from the K1200 at an energy of 140 MeV/nucleon and was impinged on a 376 mg/cm^2 ^{9}Be fragmentation target. The A1900 fragment separator [21] was used to isolate the interesting reaction products from the resulting assortment of nuclei produced in the ^{86}Kr on ^{9}Be fragmentation reaction. A schematic layout of the K500 and K1200 superconducting cyclotrons and the A1900 fragment
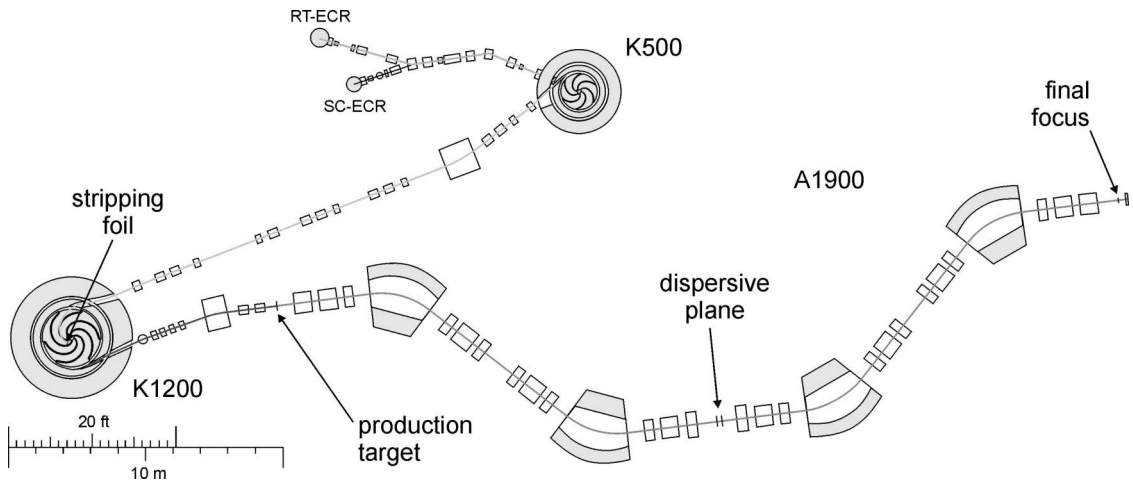
Figure 3.1: Layout of the K500, K1200 and A1900 components of the NSCL.

separator is shown in Figure 3.1.

A key feature of the present study was the production, separation, and identification of each isotope prior to its decay. For this study, the A1900 had to be tuned to optimize the production of ^{56}Sc. The magnetic rigidity of the first half of the A1900 was set to $B\rho_1 = 4.239$ Tm. At the second intermediate image the beam achieved its maximum dispersion in the horizontal direction and was passed through a 330 mg/cm^2 Al energy-loss wedge and 1% momentum slits allowing for a physical separation of the transmitted beam at the focal plane (labeled "dispersive plane" in Figure 3.1). A small momentum slit was chosen due to the unavailability of the scintillator at the dispersive plane, which is necessary for time of flight correction to the particle identification when a larger momentum acceptance is used. The magnetic rigidity of the second half of the A1900 was set to $B\rho_2 = 3.944$ Tm. The transmitted particles were brought back into focus at the final image and then delivered to the experimental endstation in the N3 vault. The rate of ^{56}Sc at the endstation was measured to be 0.0045 particles/s pnA. With an average primary beam current between 10 and 15 pnA the rate of ^{56}Sc was ~3/min. Along with ^{56}Sc, ^{57}Ti, ^{58,59}V, and ^{60}Cr fragments were also transmitted to the experimental endstation.

The fragments were implanted directly into a Double-Sided Silicon Strip Detector (DSSD) to be described later in this chapter. Particle identification was achieved

through a combination of energy loss signals in silicon detectors at the endstation and a measurement of fragment time of flight (TOF). The cyclotron rf signal was used as the TOF stop throughout the experiment. Two different timing arrangements served to create the start signal for the TOF measurement. The first start signal came from a thin scintillator in the experimental vault approximately 2 meters upstream from the DSSD. One third of the way through the experiment a beamline vacuum pump failed, resulting in the loss of the scintillator and necessitating its removal from the beam line. A replacement signal, used for the remainder of the experiment, was created from a silicon PIN detector (PIN1) located only 1m upstream of the DSSD. While using the timing signal from the PIN detector resulted in a poorer TOF resolution, due to poorer intrinsic resolution, the particle identification plot was still clean enough to clearly identify all transmitted products and ^{56}Sc was well separated from other implanted isotopes. The energy-loss signal used in particle identification was derived from the same silicon PIN detector. Plotting the energy loss as a function of TOF results in the particle identification plot shown in Figure 3.2 (using the first timing arrangement). The five different isotopes implanted at the experimental endstation again were: ^{56}Sc (12300), ^{57}Ti (192100), ^{58}V (153400), ^{59}V (539800) and ^{60}Cr (275100), where the number in parentheses was the total number of implanted ions for that nuclide used in the analysis presented in the next section. Notice that ^{56}Sc was <1% of the secondary beam delivered to the experimental endstation.

3.2   Detector Setup for Experiment NSCL-02004

During experiment number NSCL-02004 two different detector systems were used in coincidence to monitor implanted ions, β decays and γ-ray transitions. The radioactive beam was implanted into the DSSD of the β calorimeter setup to be discussed below. The β calorimeter was also used for β decay detection. The correlation of implanted nuclei with their subsequent decays was performed in software. β-delayed γ rays were
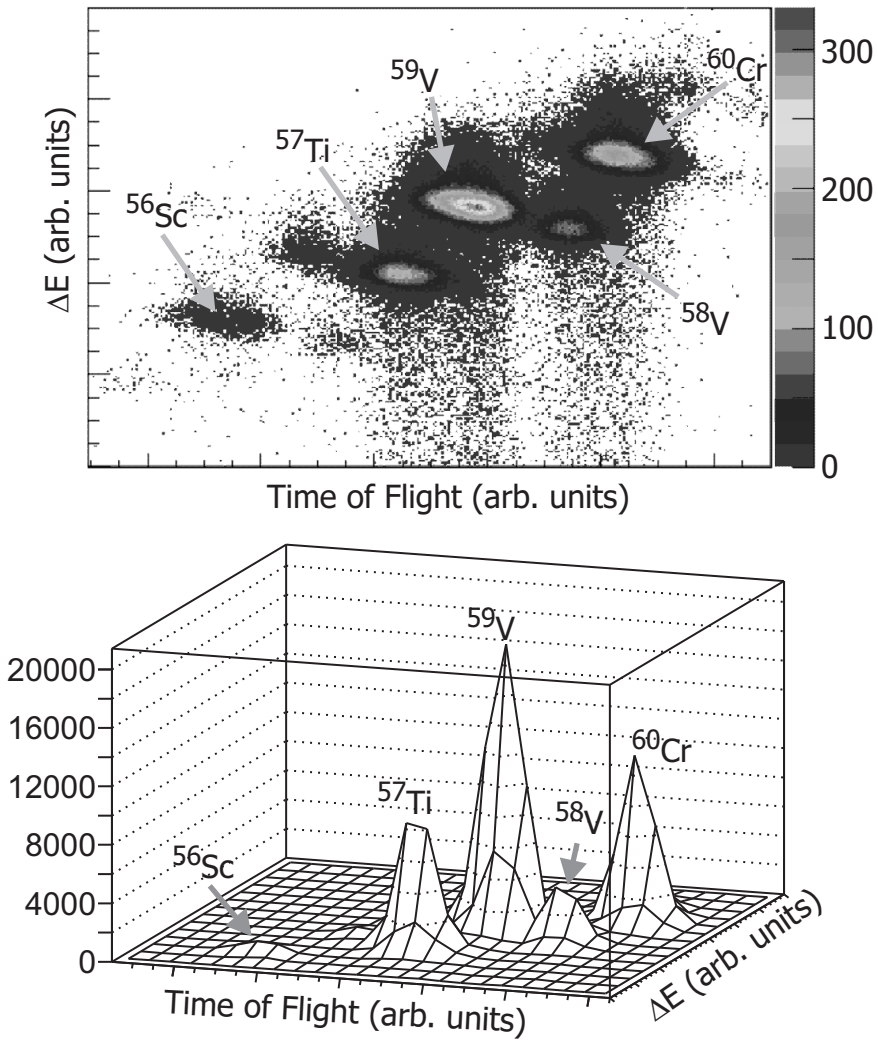
Figure 3.2: Particle identification using Time of Flight (start from scintillator 2 m upstream of the DSSD and stop from the cyclotron rf signal) and energy loss in the first PIN detector. ^{56}Sc is well separated from the other implanted isotopes even though it constitutes $<1\%$ of the total beam.

monitored with 12 HPGe detectors from the Segmented Germanium Array (SeGA) [22].

3.3   Beta Calorimeter

The low rates for the production of very neutron-rich radioactive beams makes bulk activity measurements in which the beam is cycled on and off to study β decay properties intractable [23]. A device for β decay studies using a continuously implanted beam into an active detector is preferable, eliminating the need for cycling the beam on and off. Implanting ions into an active detector would also enable the identification of implanted ions and subsequent decays on an event-by-event basis allowing for the study of species which constitute a small percentage of the total number of implanted nuclei. To this end, the NSCL Beta Counting System [24] was developed. A schematic diagram of the β counting system is shown in Figure 3.3 The center piece of the β counting system is a 4cm $\times$ 4cm $\times$ 1482μm Micron Semiconductor Double-Sided Silicon Strip Detector (DSSD) segmented into 40 1-mm strips on both the front and back faces that results in a total of 1600 pixels, each of which is an individual detector! The detector was oriented so that the p-type Si was the front and the n-type Si was the back of the detector. The DSSD was biased with +215 V on the back of the detector.

Following downstream from the DSSD were six 5cm $\times$ 5cm Single-sided Silicon Strip Detectors (SSSD) which constitute the β calorimeter. The thicknesses of SSSD1 through SSSD6 were; 990μm, 977μm, 981μm, 975μm, 989μm, and 988μm thick, respectively. Each of the six SSSDs are segmented into sixteen strips on one face and were mounted behind the DSSD so that the strip orientation alternated between the x and y directions, see Figure 3.3. The SSSDs were placed with $\sim$2 mm between the center of each detector ($\sim$1mm between faces). The DSSD and the first SSSD were separated by 7mm. Following the six SSSD detectors are two 5cm $\times$ 5cm PIN de-

28

Drawing not to scale

Beta Calorimeter

PIN1a
1061-16

PIN2a
2007-8

PIN2
2095-23

DSSD
2035-3

SSSD1
2194-1

SSSD3
2186-5

SSSD5
2194-14

PIN3
2103-14

SSSD2
2194-12

SSSD4
2186-10

SSSD6
2194-4

PIN4
2103-12

21 mm — 7 mm

9 mm 9 mm

1 mm

13 mm

1 mm

PIN1
1404-3

Al degrader

435
mg/cm^2

Beta Counting System
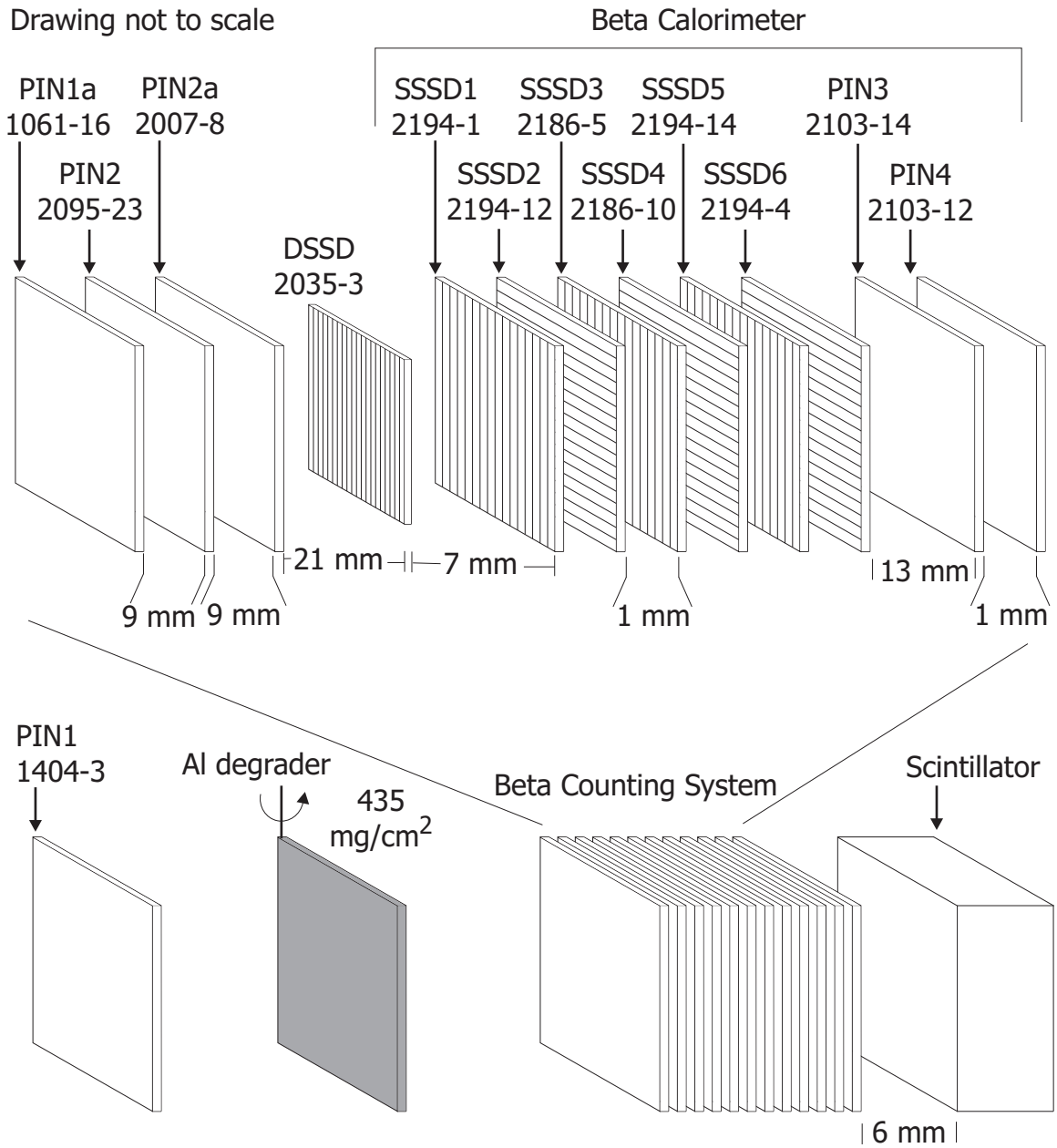
Scintillator

6 mm

Figure 3.3: Schematic of the β counting system and its position relative to other detectors used during the experiment. Drawing is not to scale and inter-detector distances are given. Silicon detector serial numbers are given below the name of the detector that will be used throughout this document.

tectors that are 993μm and 998μm thick, respectively, for a total of approximately 8 mm of silicon behind the DSSD, sufficient to stop β particles up to about 4 MeV [25]. The decays in the present experiment have β-decay Q values in the range of 10 MeV. To stop the high-energy β particles that escape the Si stack an additional 2 inches of plastic scintillator were placed after PIN4.

Upstream of the DSSD were four PIN detectors designated PIN1, PIN1a, PIN2, and PIN2a which were 474μm, 488μm, 992μm, and 966μm thick respectively. PIN1 provided both energy loss and TOF signals used in the particle identification discussed above. The signal from PIN2a was split and input into high- and low-gain amplifiers to observe β decays and implanted ions, respectively.

The thickness of the upstream Al degrader (435 mg/cm^2) located between PIN1 and PIN1a was optimized to allow for the implantation of ^{56}Sc at a depth of $\sim 600\mu$m in the DSSD in the direction parallel to the beam axis. With ^{56}Sc implanted at $\sim 600\mu$m in the DSSD there was an increased probability of recording a β particle ΔE signal above noise when the β particle was emitted in the direction of the SSSDs.

3.3.1 Electronics

A schematic diagram of the signal processing system is shown in Figure 3.4. The signals generated in each strip of the DSSD were first sent to a grounding board. The grounding board paired each signal with a ground line and grouped the signals into blocks for further processing in commercial 16-channel electronic modules. The "segmentation" process grouped the channels 1-16, 17-32, and 33-40 together for both the front or back of the detector. These blocks of channels for the front or back were then sent into preamplifiers. The challenge of detecting β decays and implantation events in the DSSD is the large difference in the total energy deposited for the two events; high energy implantation events deposit $\approx$ 1's GeV while low energy decay events deposit $\approx$ 100's keV. To overcome the disparate energy scales, Multi Channel System (MCS) preamplifiers with both low- and high-gain outputs were used with
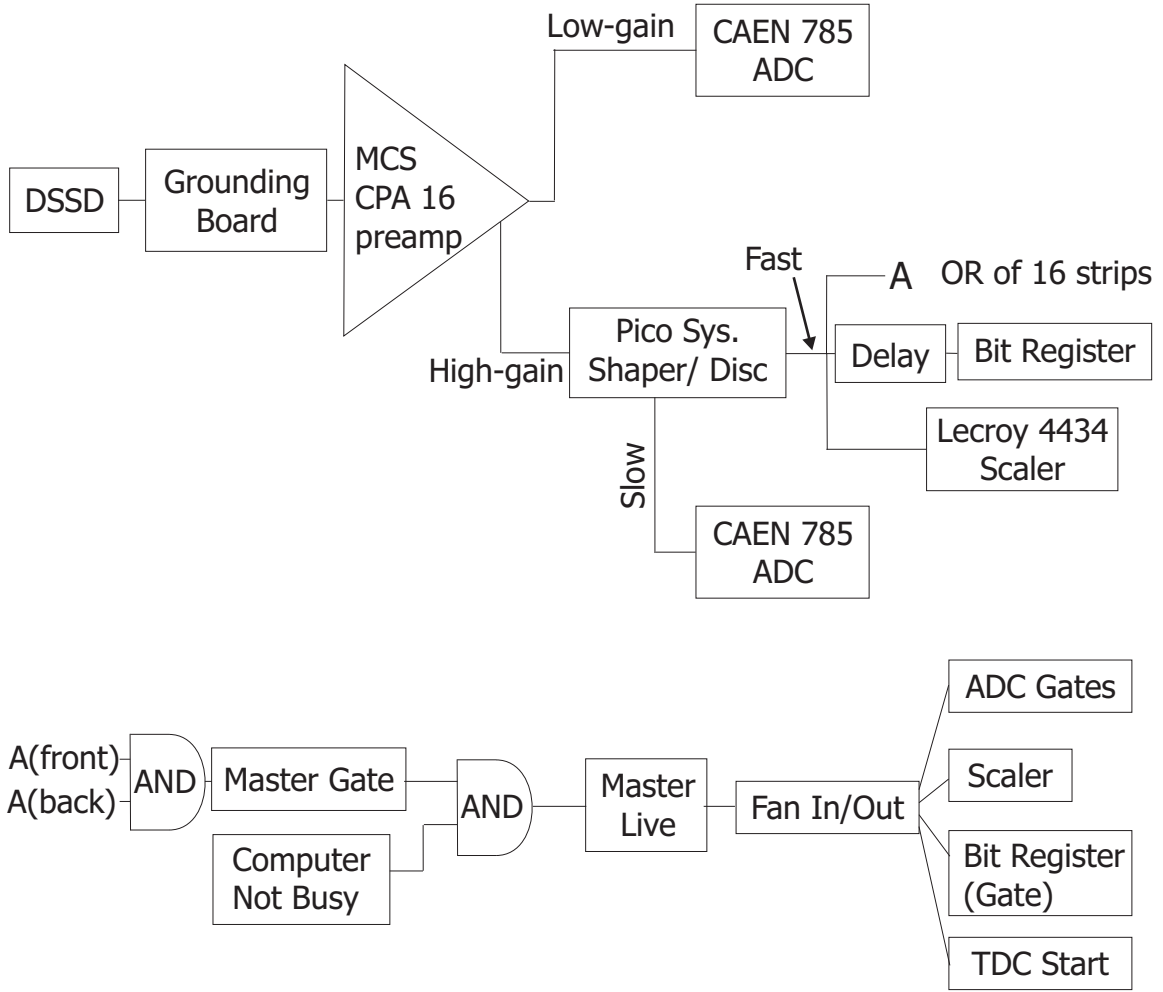
Figure 3.4: Electronics setup for the DSSD during experiment 02004 along with trigger conditions. The diagram shown on top represents one block of channels for the DSSD readout.

the DSSD. The MCS preamplifiers were also used with the SSSDs, where only the high-gain side of the preamplifier was used. High-energy implantation and low-energy decay signals were obtained from the low-gain (0.03 V/pC) and high-gain (2 V/pC) outputs of the preamplifier, respectively. The low-gain signals were then sent directly to a VME ADC. The high-gain signals were further processed through Pico Systems shaper/discriminators. Following shaping, the energy signals (high-gain) were sent to VME ADCs. The complete diagram of the electronics setup for the DSSD, including the trigger logic, is shown in Figure 3.4. The timing signals of the 40 front channels, from the Pico Systems module, are OR'ed together, as are the 40 back channels. The

OR'ed front and back signals are AND'ed to provide the master gate signal in the experiment. The master gate signal AND'ed with a computer not-busy signal define the master live signal. The master live signal triggered computer acquisition to read the detectors. The 12 Ge detectors were read on every event but could not trigger the acquisition independent of the DSSD. The DSSD was read in blocks of 16 low- and high- energy channels. For example, if front strip 10 registered a decay event, front strips 1 through 16 were read into the analysis from both the high and low gain signals. The SSSDs were read out two detectors at a time. For example, if strip 1 in SSSD1 registered an event then strips 1 through 16 were read into the analysis for both SSSD1 and SSSD2.

A schematic diagram of the PIN electronics are shown in Figure 3.5. A mentioned before, PIN1 was used as the TOF start signal and the cyclotron rf signal was used as the TOF stop for particle identification. PIN2a was used as both a fragment and a β detector.

Implanted ions and decays were "time stamped" on an event-by-event basis for use in the software correlation. The time signal was derived from two 16-bit EG&G RC014 Real Time Clock (8^6Hz) modules operated in parallel. The 8^6Hz internal pulser from Clock1 was downscaled by a factor of eight and counted by Clock1. At the reduced frequency, Clock1 filled its 16 bit field in 2 s, a resolution of 30.5 μs. When Clock1 reached the end of its range an overflow signal was sent to Clock2, which counted the number of resets. The two clocks were read out on every event (both implanted ions and decays) to determine the time stamp. The time stamp was derived from the equation:

$$timestamp = clock1 + 65536 * clock2$$

3.3.2   Calibration

Each Si detector was calibrated with both a ^{90}Sr β and ^{228}Th alpha source. A ^{228}Th alpha spectrum was accumulated for each strip for gain-matching purposes. The strips
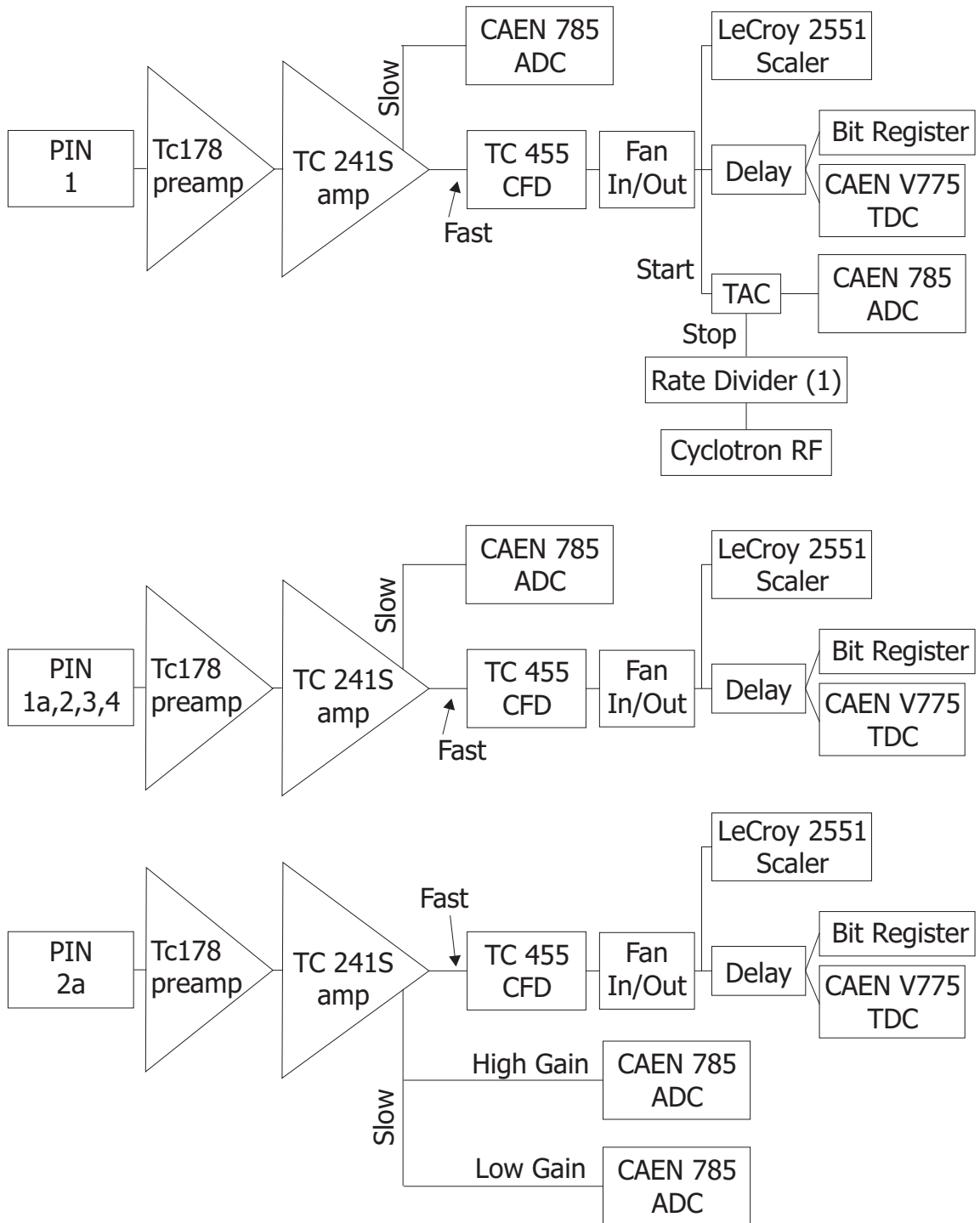
Figure 3.5: Electronics setup for PIN detectors during experiment 02004.

were gain-matched in software based on the centroid of the lowest energy alpha peak at 5.4 MeV. The total ^{228}Th spectra created by summing all 40 strips on front and back of the DSSD are shown in Figure 3.6(a-d). Two different methods were used to determine the energy of the alpha particle for the spectra, shown in Figure 3.6, and are labeled as either E_{sum} or E_{max}. E_{sum} was determined by summing the energy collected in the DSSD (above threshold) for all 40 strips, shown in Figure 3.6(a,c) for either the front or back of the DSSD, respectively. E_{max} was determined by comparing the energies deposited in the individual 40 strips of the DSSD (above threshold), for either the front or back of the detector, and only reporting the maximum energy, shown in Figure 3.6(b,d). Two important observations were made concerning the alpha spectra. First, the resolution of the front is much better than the back of the DSSD. As a result, the energy signals from the front of the DSSD were used whenever a DSSD energy signal was needed. Secondly, in calibration spectra reporting the maximum energy deposited into one channel, Figure 3.6(b,d), there is significant low-energy tailing on the individual alpha peaks, especially for the back of the detector. Low energy tailing in the maximum-energy spectra can result from either the incomplete collection of charge in the DSSD, or the division of charge between two adjacent strips. Comparing the two spectra from the back of the DSSD (sum versus maximum energy) it is seen that most of the low-energy tailing is removed when the energy sum is used, suggesting charge division between adjacent strips on the back of the detector is important. The small low-energy tailing is not improved significantly between the sum and maximum-energy spectra for the front of the DSSD suggesting that its origin might be incomplete charge collection.

Threshold calibrations using a ^{90}Sr source were also performed. First, hardware thresholds were set for each strip individually by observing the shaped output of the DSSD on an oscilloscope triggered with a CFD signal. A ^{90}Sr spectrum was then collected for each strip and used to determine the software threshold. Representative ^{90}Sr spectra for the front and back of the DSSD are shown in Figure 3.7. Strips near

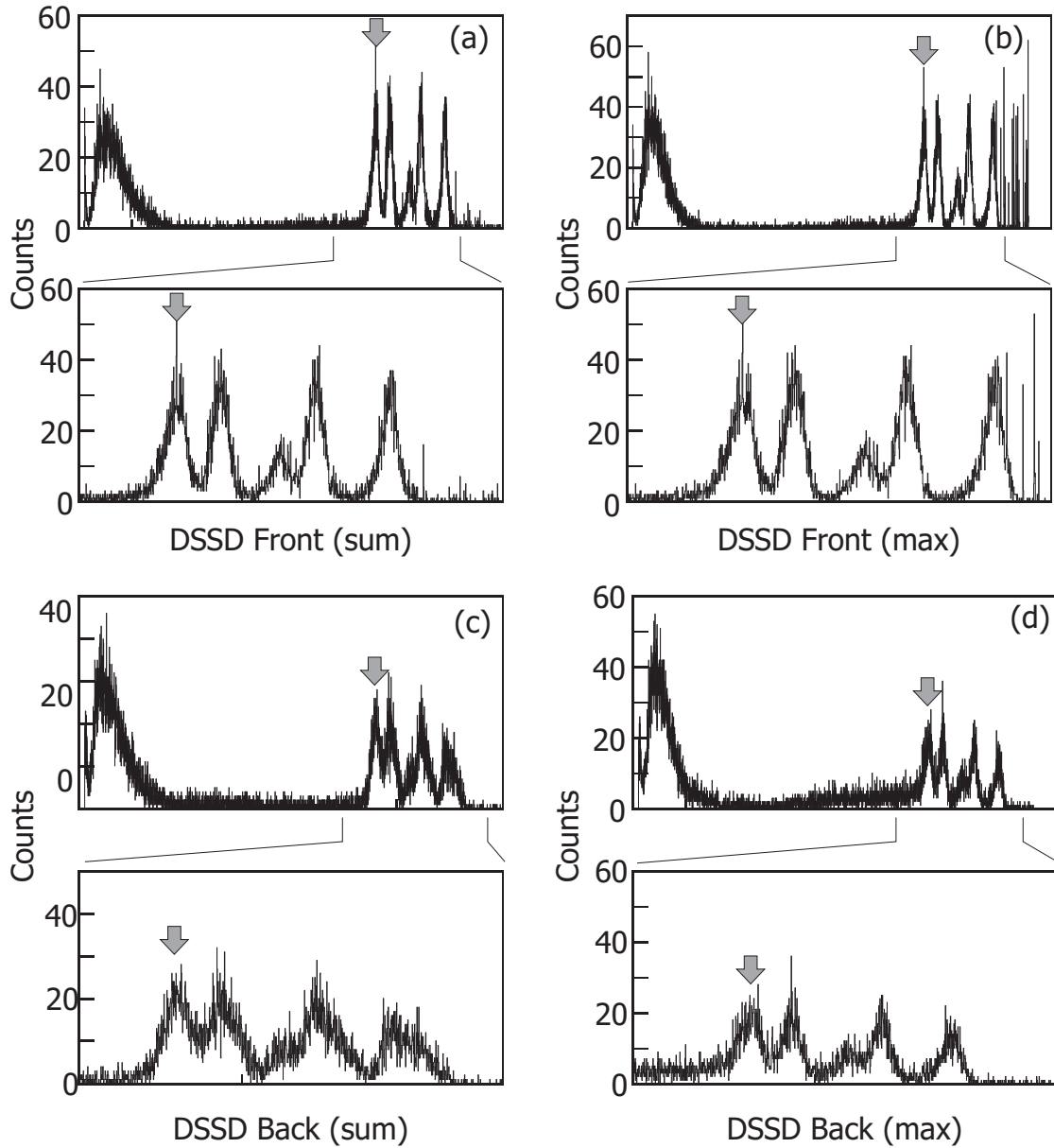Figure 3.6: DSSD ^{228}Th calibration for the front and back of the DSSD. Arrows mark the 5.4 MeV ^{228}Th alpha peak that was used for gain-matching. Panels a,c report the total energy collected in the DSSD determined from the sum of the energy deposited in each strip. Panels b,d report the maximum energy collected in one channel.
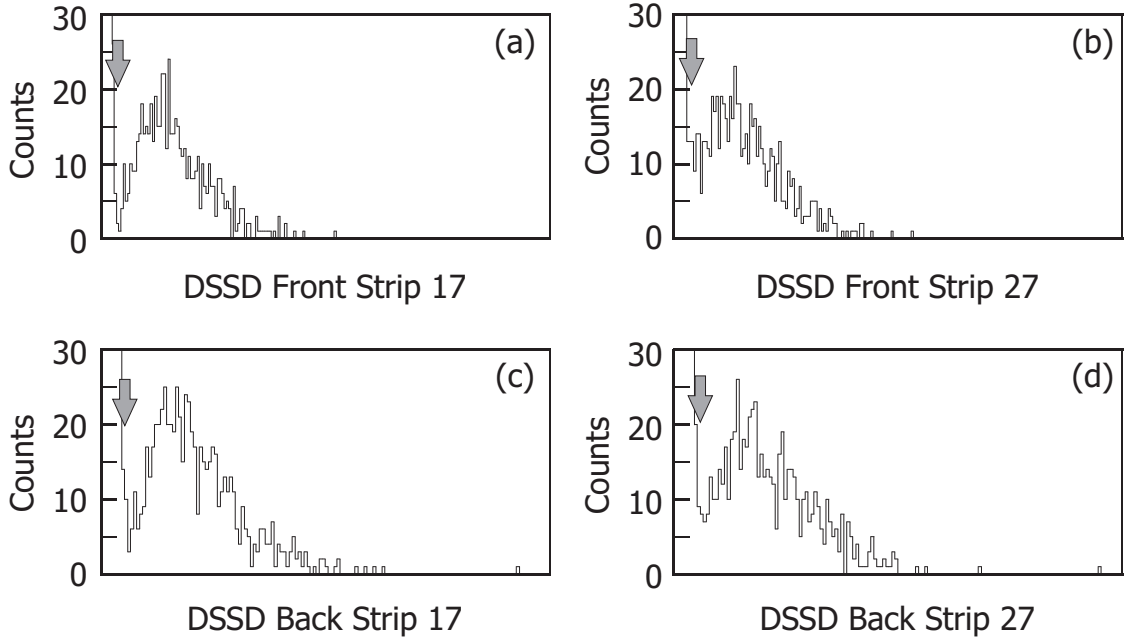
Figure 3.7: Representative DSSD ^{90}Sr calibration for the front and back of the DSSD. Arrows mark the location of representative software thresholds.

the edge of a readout cable, such as strip 17, were inherently noisier and required an increased hardware threshold. Additionally, the back of the DSSD was noisier than the front, supporting the choice of the front strips for DSSD energy information. The average threshold for the DSSD strips was ~120 keV.

To take advantage of the high number of pixels in the DSSD, the secondary fragment beam was defocused to illuminate as much of the detector as possible. The defocusing resulted in the illumination of approximately 2/3 of the DSSD. The implantation distribution in the x and y dimensions of the DSSD for all implantation events is displayed in Figure 3.8(a). The distribution for ^{56}Sc events is shown in Figure 3.8(b). The problem encountered early by Prisciandaro [23] using single output preamplifiers, where the average implantation multiplicity was six, making the localization of an implant event difficult, was remedied by using the dual-output preamplifiers discussed in Section 3.3.1. Using the dual-output preamplifiers the location of an implantation event could be well defined, for example Figure 3.9 shows the implantation multiplicity for the front and back of the DSSD.
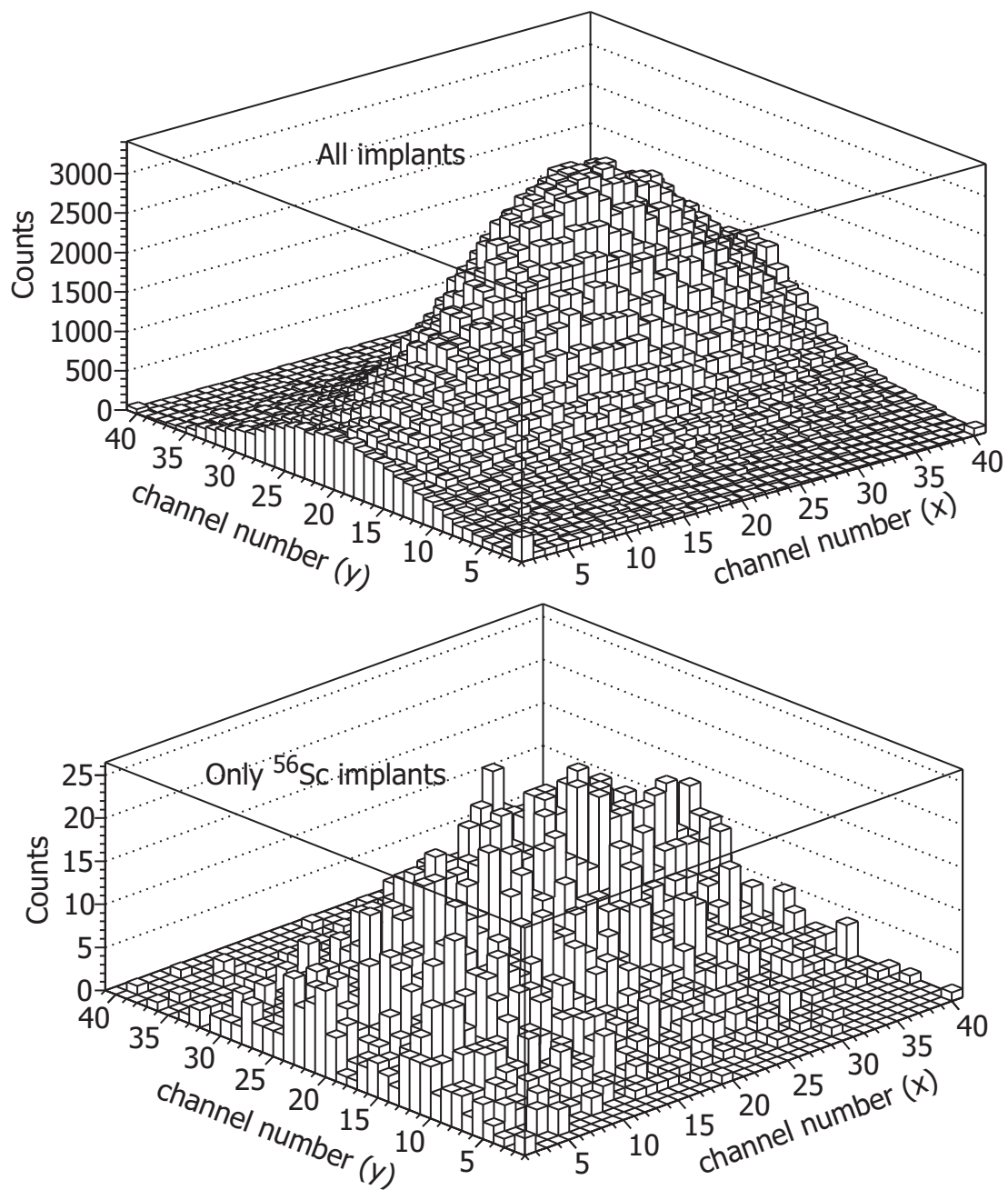
Figure 3.8: The radioactive beam is defocused to illuminate approximately 2/3 of the DSSD and the distribution of implanted ions in the x and y dimension across the face of the DSSD is shown in (a). The implantation profile is still distributed across the face of the DSSD when (b) only ^{56}Sc events are displayed.
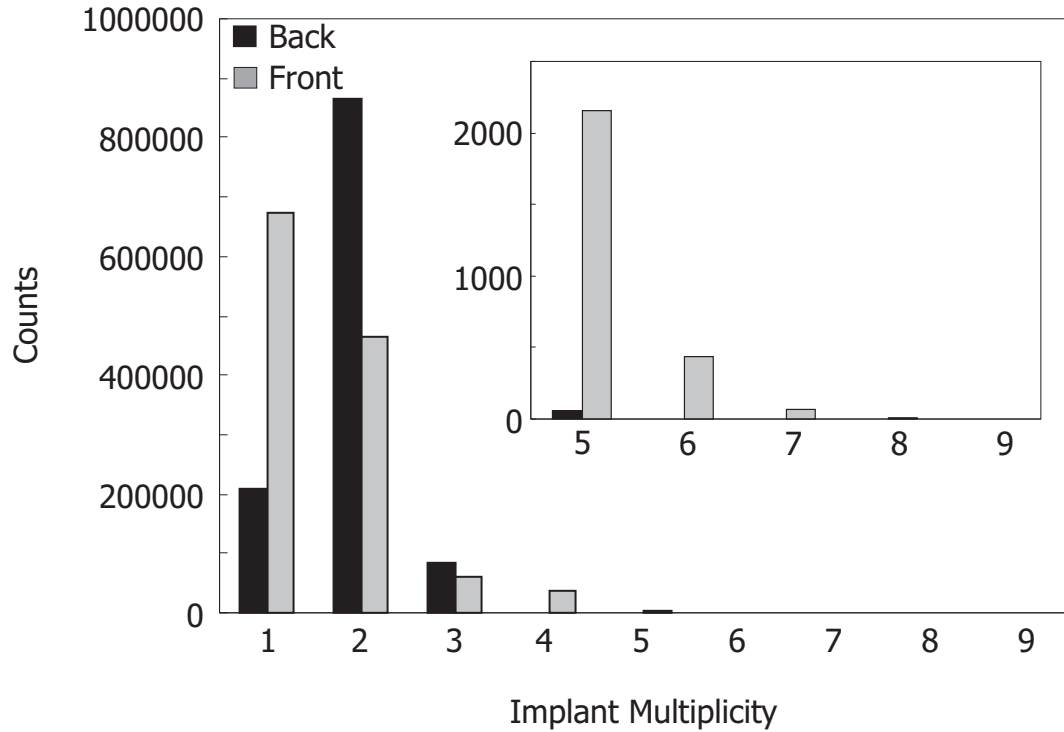
Figure 3.9: Implantation multiplicity of the DSSD. The inset shows implantation multiplicities, five through nine, with a higher resolution on the y axis.
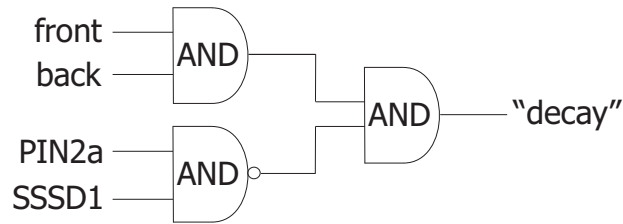
Figure 3.10: Software condition between the front and back of the DSSD, PIN2a, SSSD1 which was defined as a decay.

3.3.3 Correlation

Correlations between implanted ions and decays were performed in software on an event-by-event basis. An implanted ion was defined as a signal above threshold in PIN1 and a front and back (low-gain) strip of the DSSD, combined with no signal in the first SSSD. A decay was defined as a signal above threshold in a front and back strip (high-gain) of the DSSD, combined with either a signal in PIN2a or SSSD1 or, alternatively, a signal in neither PIN2a nor SSSD1, see Figure 3.10. An event which fired both PIN2a and SSSD1 was identified as a penetrating light particle which leaves

an energy signal in every detector of the β counting system. After defining the conditions necessary for identification of implanted ions and decays the two distinct events must be correlated. Correlations between implanted ions and decays were performed in software on an even-by-event basis based on pixel location and timing information. Previous analyses of data from the beta counting system had restricted the decay-implant correlation to events that occur within the same pixel (see for example Ref. [26]). The average implantation rate in the current experiment over the entire detector was lower than 10Hz. The low implantation rate allowed for the expansion of the fragment-β correlation field to the surrounding 8 pixels.

The two parameters defining the decay-implant correlation function are the maximum correlation time and the minimum time between implanted ions. The maximum correlation time is defined as the longest time window in which a β decay can be correlated with an implanted ion. The longer the maximum correlation time, the greater the chance of correlating the implanted ion of interest with a background event. In addition, the maximum correlation time needs to be long enough to encompass a few half-lives of the nuclide under study in order to extract a reasonable decay curve. The minimum implantation time is defined as the minimum amount of time between two successive implantation events before the second implanted ion will be considered in the correlation. The shorter the minimum implantation time, the greater is the chance of incorrectly correlating a decay with an implantation.

In the present analysis the maximum correlation time and the minimum time between implanted ions were both set to one second for the analysis of ^{56}Sc, ^{57}Ti, ^{58}V, and ^{59}V. Due to the longer half-life of ^{60}Cr, its analysis was conducted with the maximum correlation time and minimum time between implanted ions set to five seconds. A decay curve for each isotope was constructed by histogramming the time difference between the implanted ion of interest and the correlated β decay. An example is shown in Figure 3.11(a) for the decay of ^{58}V. By integrating the decay curve for the parent isotope the total number of detected β decays from ^{58}V can be
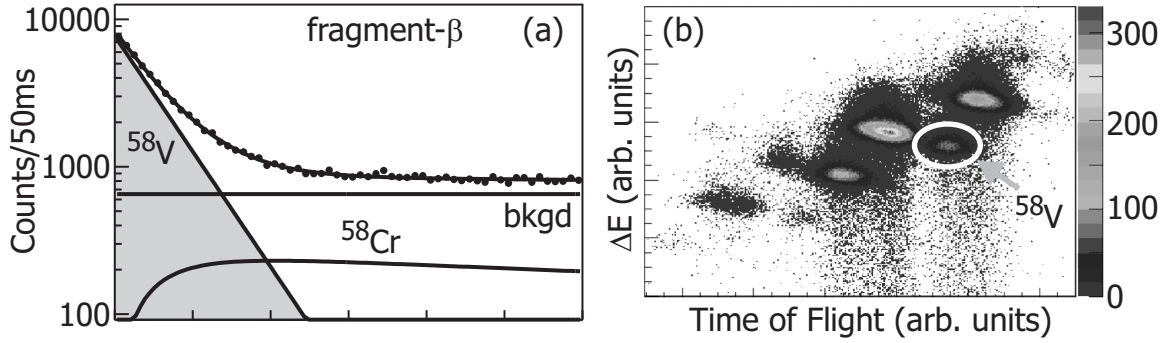
Figure 3.11: The decay curve in (a) is produced by histogramming the time difference between ^{58}V implanted ions and the correlated β decays. By fitting the decay curve, the contribution due to ^{58}V β decays (shaded region) can be determined. Using the total number of ^{58}V decays and the total number of implanted ions, from the particle ID spectrum shown in (b), the β detection efficiency for the calorimeter can be determined. The β detection efficiency for all isotopes was $\sim$30%.

determined. Combined with the total number of implanted ions, from the particle ID shown in Figure 3.11(b), the β-detection efficiency of the DSSD was calculated. For all the isotopes studied the β-detection efficiency was $\sim$30%.

During the course of the present analysis, two methods were used for handling the correlation of multiple decays within the maximum correlation time, following a specific implantation event. In the first method, once a decay was correlated with an implanted ion, the implantation information was deleted (back-to-back decay rejection). If another decay is detected that would have been within the correlation time of the deleted implanted ion the decay is ignored. Back-to-back decay rejection led to the suppression of correlations at longer times in the decay curve that were associated with daughter and grand-daughter activities. The effect is not very significant for those decay chains with daughter half-lives in the second range (such as the decay chain associated with ^{58}V). However, the reduction at longer correlation times significantly affected the decay curve of ^{56}Sc, where the half-lives of all three generations are fairly short (40 ms, 200 ms, and 216 ms for ^{56}Sc, ^{56}Ti, and ^{56}V, respectively) and should reasonably be expected to occur within the one second correlation time. Using back-to-back decay rejection resulted in an inability to fit the ^{56}Sc decay curve with multiple generations over the one second correlation window, making it difficult to

extract the ^{56}Sc half-life. The second method of correlating multiple decays within a given correlation time ensured that all decays that occurred after an implanted ion, up to the maximum correlation time are correlated. Since the implanted ion information was never erased, multiple decays can be correlated with the same implanted ion. The removal of back-to-back decay rejection increased the events at longer correlation times, associated with daughter and grand-daughter decays, and enabled the fitting of the ^{56}Sc decay curve through all three generations. The back-to-back decay rejection condition was removed for all analyses presented here.

Using the high segmentation of the DSSD combined with the segmentation of the SSSDs, particles can be tracked through the β calorimeter by making multiple measurements of their x and y positions as energy is deposited in the different Si detectors. With this capability, different events in the SSSDs can be identified. Light particles transmitted to the endstation along with the primary beam follow straight line paths through the stack. Since there is little deviation in their path as they traverse the stack, such events will show a high correlation between y positions (or x positions) measured with different detectors. For example, the strips on the front of the DSSD were oriented in the y direction as were the strips of SSSD1. A plot of the measured y position from the DSSD versus the measured y position from SSSD1 is shown in Figure 3.12(a). Two distinct distributions can be seen. The first distribution is a highly correlated pattern running across the diagonal which can be associated with light particles following straight-line trajectories. The second distribution observed in Figure 3.12(a) originates from β particles. This distribution can be isolated by applying the aforementioned software condition for identifying β decays, PIN2a, DSSD, and SSSD1 can not all fire in coincidence, and results in Figure 3.12(b), which is free from light particles. There is a small correlation between the two different y-position measurements but due to the isotropic emission of β particles, it is much weaker than the correlation observed with light particles. Lastly, when the y dimension, from the front of the DSSD, is plotted against a measurement of the x position, a plot similar
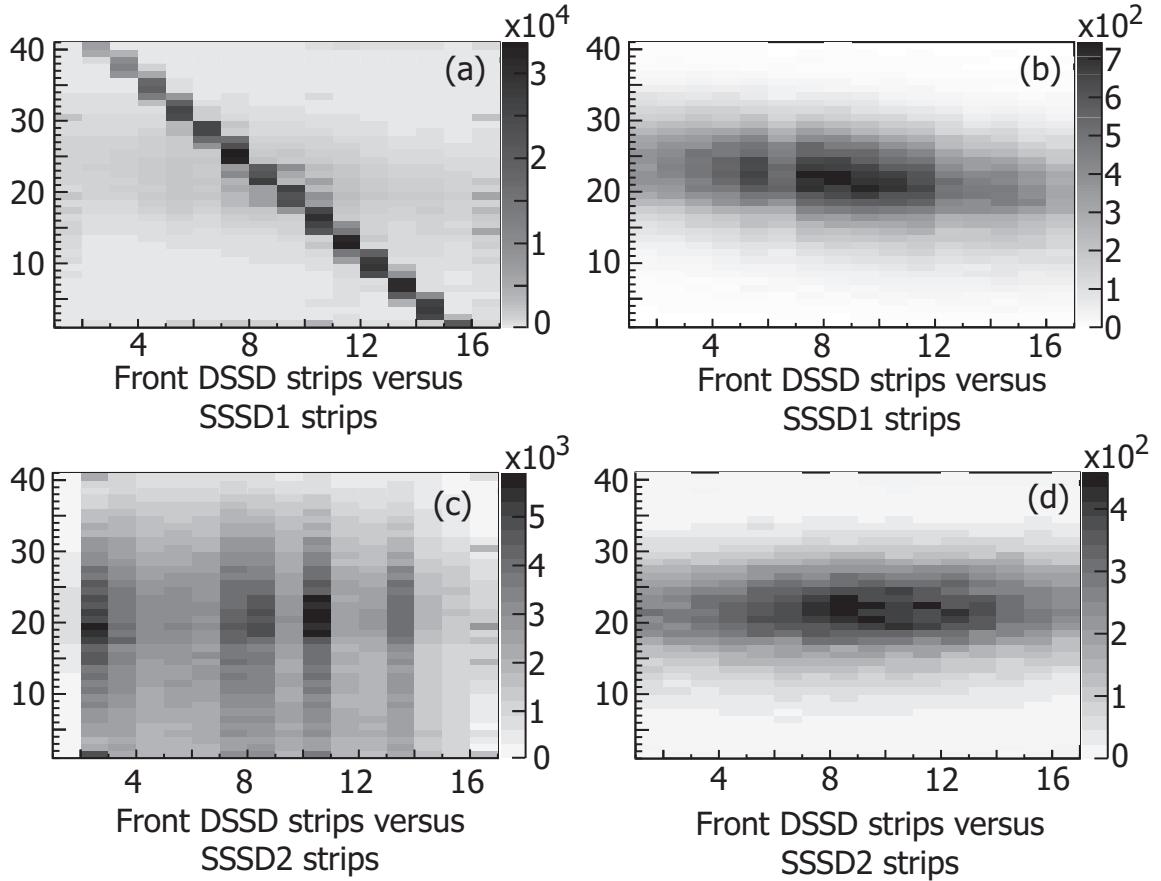
Figure 3.12: Correlation, in strip number, between the front of the DSSD (y direction) and (a) SSSD1 (y direction) (b) SSSD1 (y direction) with a restriction to only decay events, (c) SSSD2 (x direction), and (d) SSSD2 (x direction) with a restriction to only decay events. In (a) the two distinct distributions arise from light particles and decay events which can be isolated, and are shown in (b). Plotting the x versus y coordinate in (c,d) recovers a plot similar to the implantation profile.

to the implantation profile should result. Shown in Figure 3.12(c,d) are the plots of the DSSD front (y position) versus SSSD2 (x position) for all nuclides, and gated on decays, respectively. As can be seen, there is no correlation observable in the xy plot.

3.4 γ-ray Detection

γ rays were monitored using twelve HPGe detectors from the MSU Segmented Germanium Array (SeGA) [22]. Each Ge crystal has a diameter of 70 mm, a length of

Figure 3.13: Electronics setup for SeGA during experiment NSCL-02004.

80 mm and is divided into eight segments along its length and four segments along the cylindrical axis for a total of 32 segments. As the β-decay studies are conducted with a stopped beam, the high segmentation typically used for the Doppler correction of γ-ray energies is not needed and only the central contact which provides 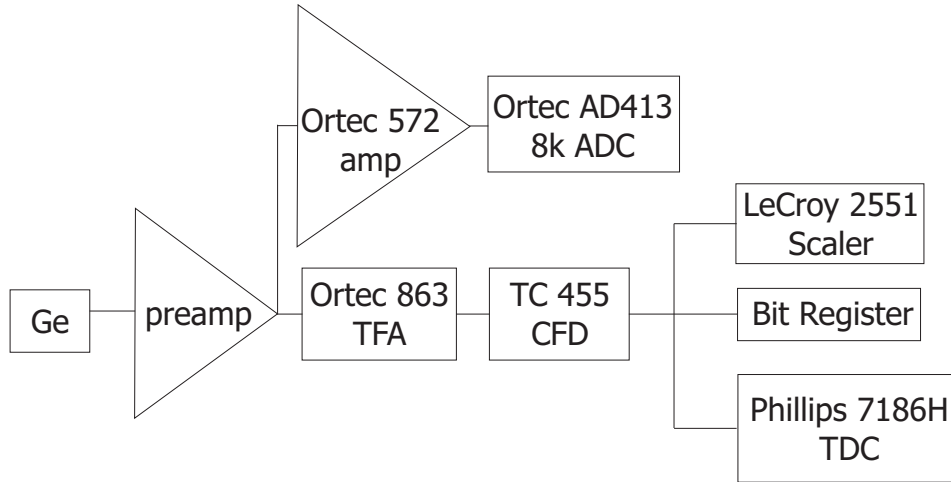a total energy signal of each detector was used in the present study. A schematic diagram of the Ge electronics are shown in Figure 3.13.

3.4.1 Calibration

The twelve γ-ray detectors were arranged in two separate rings of six detectors each, with each cylindrical axis parallel to the beam axis, as shown in Figure 3.14. In this relatively close-packed configuration the energy and efficiency calibration data were measured with a Standard Reference Material (SRM) source, containing ^{125}Sb, ^{154}Eu, and ^{155}Eu, along with a separate ^{56}Co source.

The SRM and ^{56}Co sources were placed at the DSSD location and the raw Ge energy spectra were accumulated for all 12 Ge detectors simultaneously. The peak locations were fitted using the Oak Ridge Display, Analysis and Manipulation Module (DAMM) [27]. Energy calibrations were obtained from a second order polynomial fit to the true peak energy versus the channel position in each of the twelve detectors.
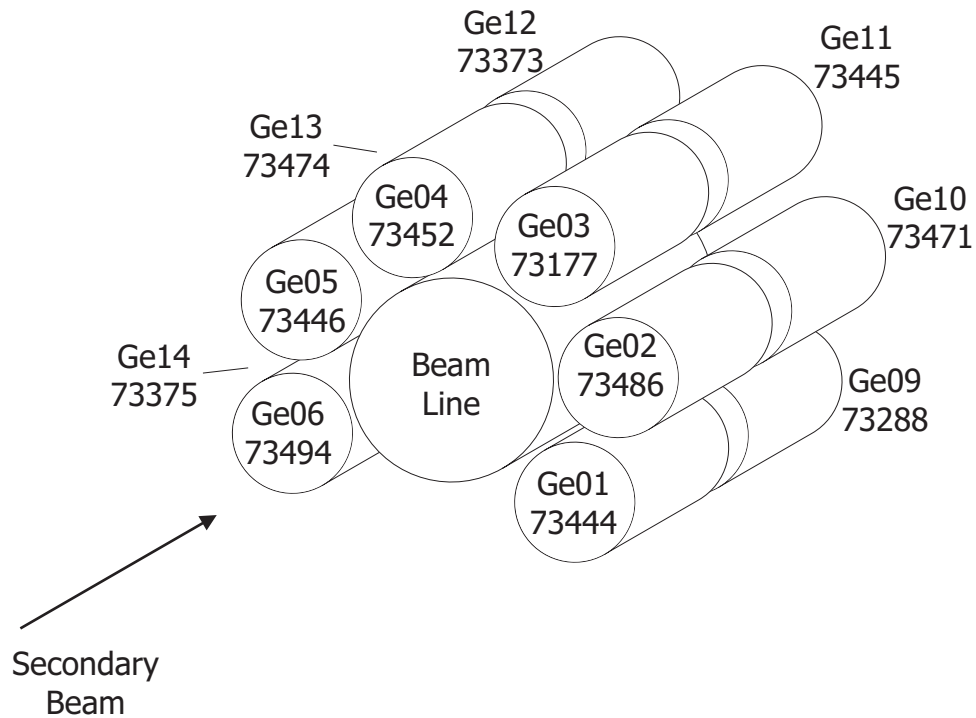
Figure 3.14: Schematic arrangement of the twelve HPGe detectors from SeGA around the beam line containing the β calorimeter. Serial numbers for individual Ge detectors are given as well.

Two different Ge energy calibrations have been used to analyze the data.

In the first analysis a number of different energies from the standard sources were used to calibrate the array from 123.1 to 2598.4 keV, shown in Table 3.1. The residuals of the first calibration, defined as the difference between the true energy and the calibrated energy and shown in Figure 3.15, displayed a pronounced curvature and deviated from actual values by more than 0.5 keV at an energy of 1 MeV. This calibration was used in Ref. [28] and resulted in a small mismatch between the fitted energy of two ^{56}V γ-ray transitions and the results of previous measurements. The energies for ^{56}Sc γ-ray transitions were also consistently low compared to a complementary Gammasphere experiment performed on ^{56}Ti [29]. As a result, a new energy calibration was constructed.

The second Ge energy calibration used two energy ranges. The first energy range (low) extended from 123.1 keV through 1596.5 keV and the second energy range (high) started at an energy of 1274.4 and extended through 3253.4 keV. The γ ray

Table 3.1: List of γ-ray energies in keV for the two Ge energy calibrations.

| Source	First Calibration	Second Calibration	
SRM	123.071	123.071	low
SRM	247.93	247.93	low
SRM	591.763	591.763	low
SRM	723.305	723.305	low
^{56}Co	846.771	−	
SRM	873.19	873.19	low
^{56}Co	1037.84	−	
^{56}Co	1238.282	−	
SRM	1274.436	1274.436	low and high
SRM	1596.495	1596.495	low and high
^{56}Co	1771.351	1771.351	high
^{56}Co	2015.181	−	
^{56}Co	2034.755	2034.755	high
^{56}Co	2598.459	2598.459	high
SRM	2614.533	−	
^{56}Co	3201.962	−	
^{56}Co	3253.416	3253.416	high
^{56}Co	3272.99	−	
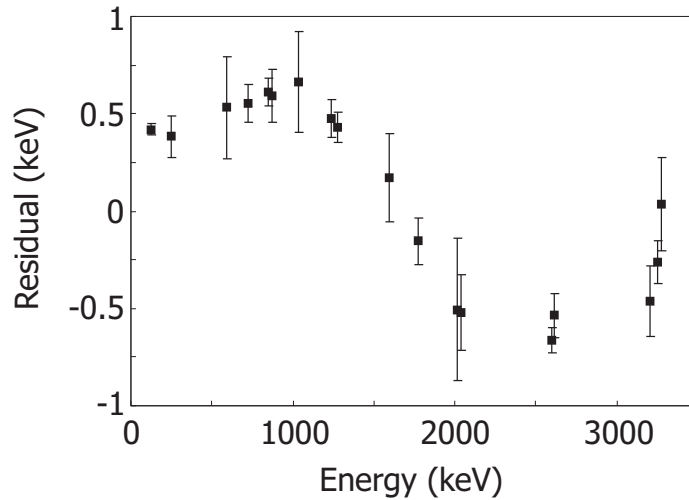
Figure 3.15: Residual plot for the 12 detector Ge array using the first energy calibration. Similar curvature is also observed in each of the twelve individual detector residual plots. There is significant deviation from true values, especially at 1 and 2.5 MeV.

transitions used in the low and high energy calibrations are listed in Table 3.1. To evenly weight the fit over the entire energy range considered, an attempt was made to use evenly distributed energy values, and in the case of a cluster of energies, at 3200 keV for example, only one of the energies was used. The transition between the low- and high-energy calibrations was arbitrarily chosen to occur at an energy of 1460 keV and it was checked that the position of the transition did not affect the calibrated energies. The low- and high-energy calibrations greatly reduced the magnitude of the residuals. The individual residuals for all 12 detectors are shown in Figure 3.16. The residuals of the Ge array, composed of all twelve individual detectors, is shown in Figure 3.17. Using the low- and high-energy calibrations, the residuals have been reduced dramatically to ± 0.15 keV, and the curvature has been minimized. The error on reported γ ray energies provided in the results section were obtained by adding in quadrature the error from the fit (0.15 keV), the error from the peak position given by DAMM, and the error from the random number generator (0.3 keV). The random number generator was used to correct for the ADC real-to-integer number conversion. The error from the random number generator was estimated by observing the shift in peak energy with a different value used as the start seed. An enlarged region of the calibration spectrum for all twelve detectors is shown in Figure 3.18 from 900-1100 keV. The two peaks located at 996.3 and 1004.7 are separated almost to the baseline and the full width at half maximum is 3.6 keV. Both peaks in Figure 3.18, not included in the energy calibration, are symmetric suggesting that the detectors are gain-matched correctly.

γ-ray peak efficiency measurements were completed with the SRM source using γ-ray transitions with known emission rates extending from an energy of 27.4 keV to 1596.4 keV. The absolute emission rates of transitions in ^{56}Co source used for efficiency calibration were not known, but by matching the efficiency between the 846.8 keV ^{56}Co transition and the 873.2 keV SRM γ ray, the ^{56}Co source was used to provide relative efficiencies up to 3273 keV. The logarithm of the efficiencies as a
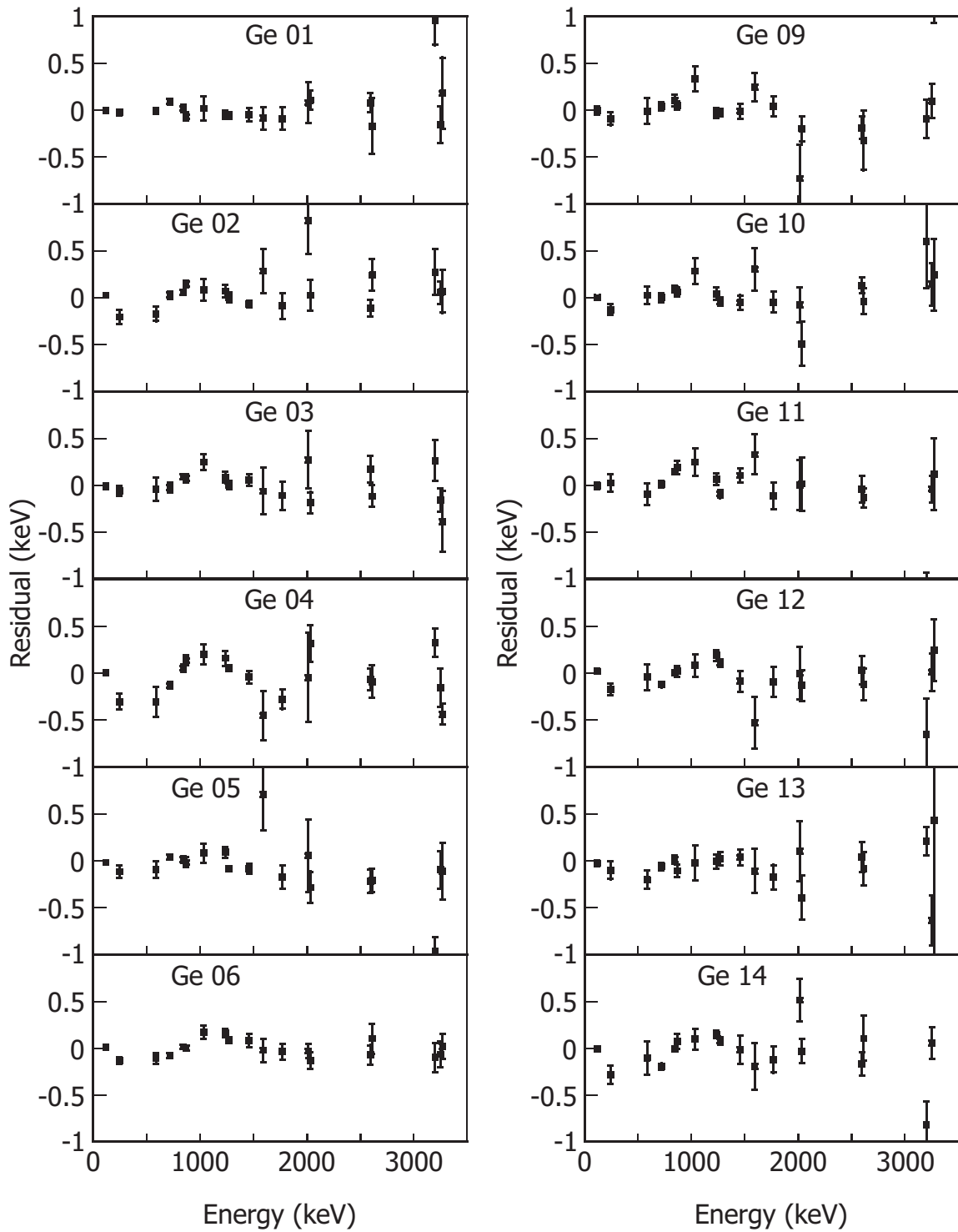
Figure 3.16: Residual plots for the individual SeGA detectors. The switch between low- and high-energy calibrations occurred at 1460 keV.
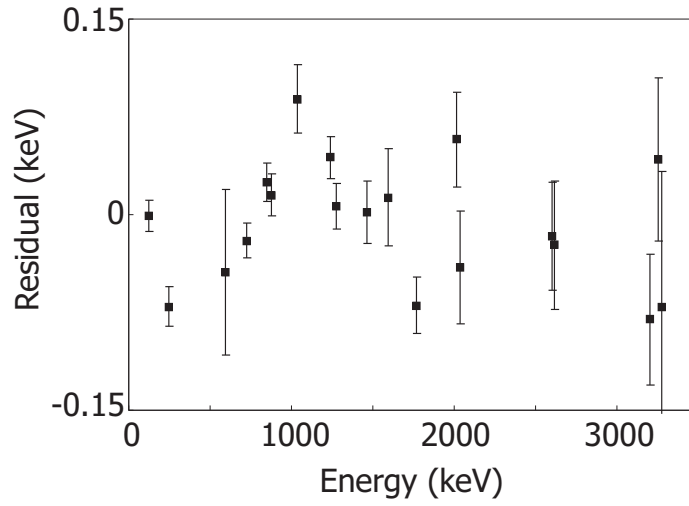
Figure 3.17: Residual plot for the sum of all twelve detectors in the second Ge calibration. See text for details.
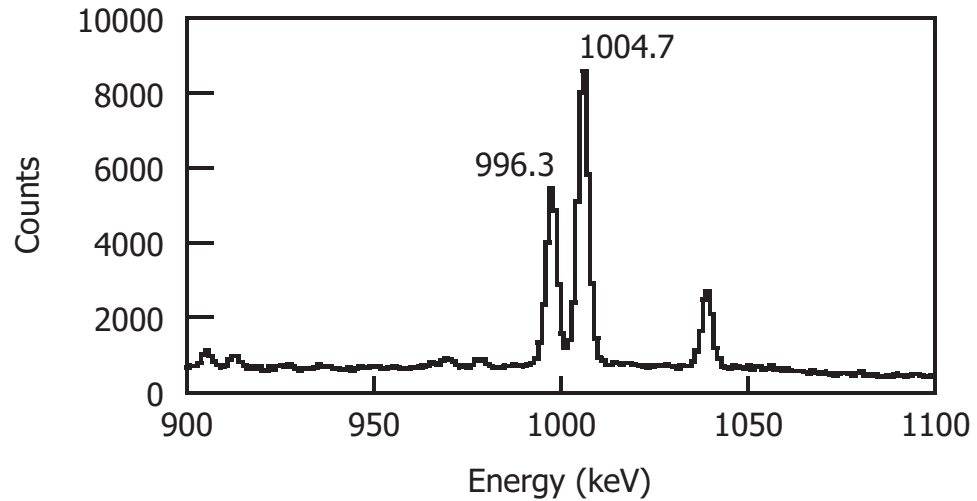
Figure 3.18: Sum Ge spectrum for all twelve individual Ge detectors between 900-1100 keV. The two peaks around 1 MeV are cleanly separated and the full width at half maximum is 3.6 keV.
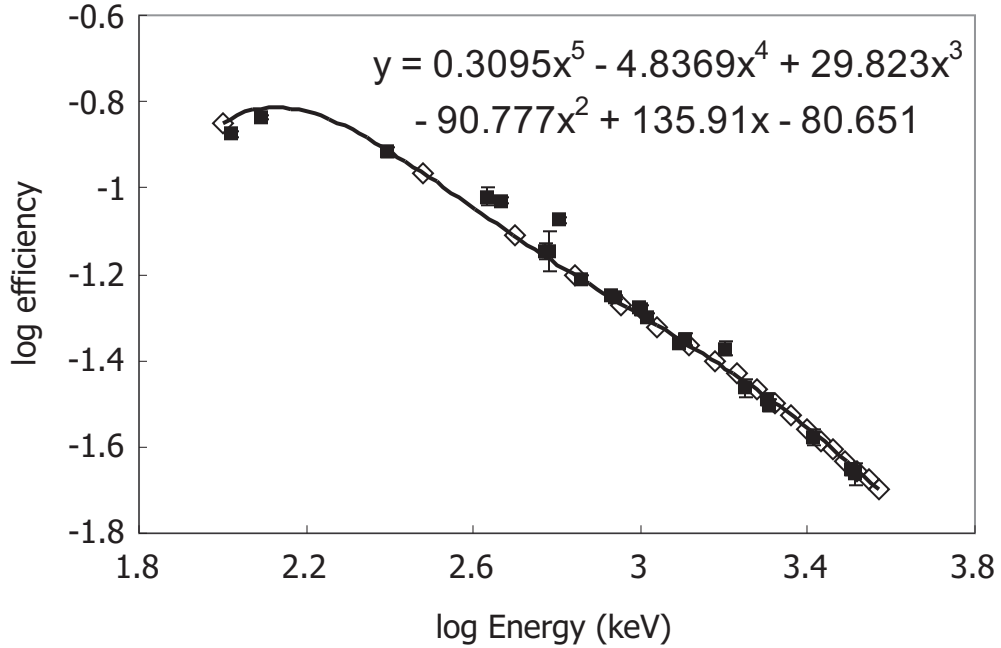
Figure 3.19: Efficiency of the array of 12 HPGe detectors as a function of energy. The diamonds represent calculations with the MCNP code using a point source geometry at the DSSD location. The squares represent experimentally determined efficiencies. A fifth order polynomial relating the energy with efficiency is shown by the solid line.

function of the logarithm of the energy were then fitted with a fifth order polynomial. The results are shown in Figure 3.19. The array efficiency was also simulated using the MCNP code and accurately reproduced the experimental data down to 105 keV, sufficient for the γ rays observed in the present study. The efficiency of the array at 1 MeV was determined to be 5.3% .

Chapter 4

Experimental Results

The nuclides implanted into the DSSD during experiment NSCL-02004 included: $^{56}_{21}$Sc, $^{57}_{22}$Ti, $^{58,59}_{23}$V, and $^{60}_{24}$Cr. Of these nuclides, ^{56}Sc has not previously been studied, and the other nuclides have been isolated only in small quantities. Thus, the present results represent huge improvements in basic knowledge of the β-decay properties of these nuclides. Additionally, the experiment was configured to detect isomeric γ rays emitted from the implanted nuclides if present. Altogether, a wealth of information was obtained for each nuclide. For all implanted nuclides a decay curve and β-delayed γ-ray spectrum were obtained by making a cut on implantation-correlated β decays. For multiplicity-two γ-ray events ($m_\gamma = 2$), a $\gamma\gamma$ matrix was constructed by plotting the energy of the second detected γ ray against the energy of the first γ ray. An example of the $\gamma\gamma$ matrix for ^{58}V is shown in Figure 4.1(a). Gated slices of the $\gamma\gamma$ matrix provided a coincidence spectrum for each γ-ray transition. For multiplicity-one γ rays ($m_\gamma = 1$), a plot of the the decay curve versus the γ spectrum was created, from which a γ-gated decay curve for each γ-ray transition was extracted through a slice perpendicular to the time axis. An example of such a plot is shown in Figure 4.1(b). The only exception to the γ gated decay curve procedure described above was in the analysis of ^{56}Sc. To avoid the loss of statistics associated with the restriction of the γ-ray multiplicity to a value of one, each individual Ge spectrum ($m_\gamma \geq 1$) was
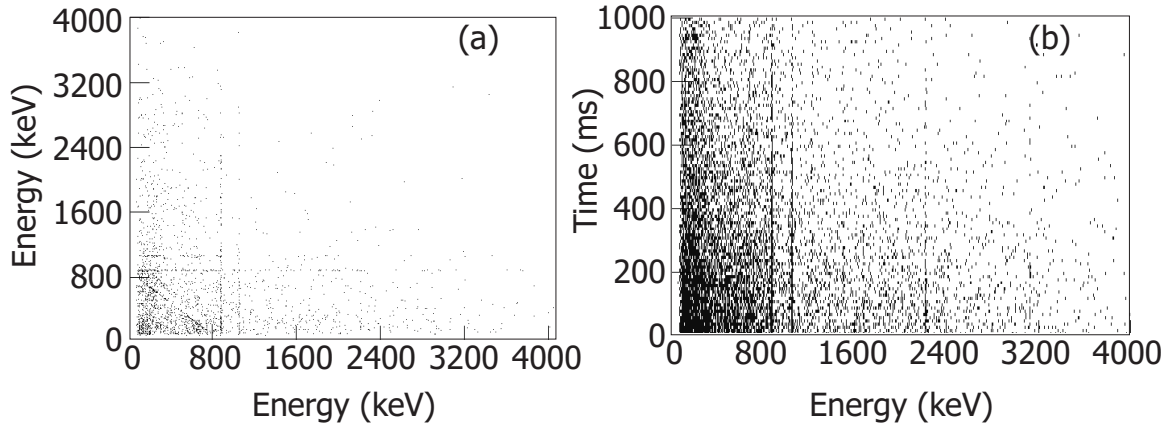
Figure 4.1: For ^{58}V, two dimensional plots of (a) the energy of the the second detected γ ray versus the energy of the first detected γ ray in a multiplicity-two γ-ray event and (b) the time versus the γ-ray energy for γ multiplicity-one events. Projections of (a) produced γγ coincidence spectra while projections of (b) onto the y axis produced γ-gated decay curves.
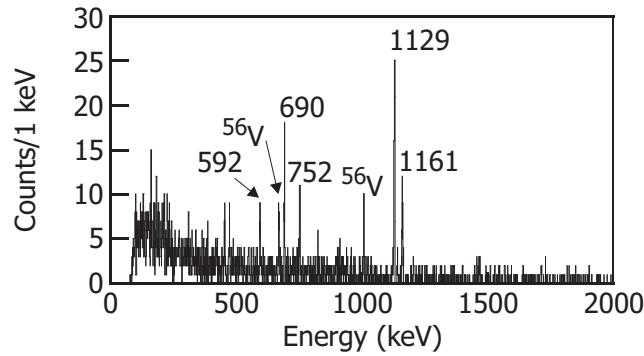
Figure 4.2: ^{56}Sc β-delayed γ-ray spectrum from 0-2 MeV for events occurring within one second after a ^{56}Sc implanted ion.

gated on the ^{56}Sc transition of interest. The twelve individual gates were summed together to extract the ^{56}Sc decay curve.

4.1 ^{56}Sc

The β-delayed γ-ray spectrum obtained for ^{56}Sc from 0-2 MeV, shown in Figure 4.2, contains βγ events that occurred within the first second following a ^{56}Sc implanted ion. A total of seven new transitions have been identified in this spectrum. As the ^{56}Ti daughter has no known γ-ray transitions [30] the five remaining transitions have

Table 4.1: ^{56}Sc β-delayed γ rays along with adopted values, absolute intensities and the initial and final states for those transitions placed in the ^{56}Ti level scheme.

E_γ,β-decay (keV)	E_γ,Adopted (keV)	I_γ^{abs} (%)	Initial State (keV)	Final State (keV)
592.3 ± 0.5	592.3 ± 0.5	7 ± 2		
690.2 ± 0.4	690.1 ± 0.4	19 ± 4	2980	2290
751.5 ± 0.5	751.5 ± 0.5	9 ± 3		
1128.2 ± 0.4	1128.5 ± 0.4	48 ± 11	1129	0
1160.0 ± 0.5	1160.5 ± 0.5	21 ± 5	2290	1129

been assigned to the β decay of ^{56}Sc, and are listed in Table 4.1.

The transitions located at 690.2±0.4, 1128.2±0.4, and 1160.0±0.5 keV compared favorably with the energies of 690.0 ± 0.5, 1128.8 ± 0.5, and 1161.0 ± 0.5 keV found in deep inelastic work reported in Ref. [29]. The weighted averages of the β-decay and in-beam results, 690.1 ± 0.4, 1128.5 ± 0.4, and 1160.5 ± 0.5 keV, were adopted as the energies for these three γ-ray transitions in ^{56}Ti. The most intense transition in the $\beta\gamma$ spectrum is located at 1129 keV and has been tentatively identified as the $2_1^+ \rightarrow 0_1^+$ transition [28]. The γ-ray transition with energy 592.3±0.5 keV falls within the error of the single γ-ray transition previously observed in ^{55}Ti [31] and could be due to a β-delayed neutron branch from ^{56}Sc to levels in ^{55}Ti. Such a branch is feasible considering that the 13.7±0.8 MeV Q-value for the ^{56}Sc β decay is considerably larger than the 5.3 ± 0.3 MeV neutron separation energy in ^{56}Ti.

The decay curve derived from ^{56}Sc-correlated β decays is shown in Figure 4.3(a). The decay curves obtained by requiring an additional coincidence with the 1129-, 690-, or 1161-keV β-delayed γ rays are shown in Figures 4.3(b-d). The half-life deduced from the 1129-keV γ-gated decay curve is statistically different from those deduced from the 690- and 1161-keV γ-gated decay curves, suggesting that two β-decaying parent states were populated in the production of ^{56}Sc. A weighted average of the half-lives extracted from the 690- and 1161-keV γ-gated decay curves results in a value of 60 ± 7 ms, which was postulated as the half-life of a high-spin β-decaying state in the ^{56}Sc parent. Since the 1129-keV γ ray has been tentatively assigned to the
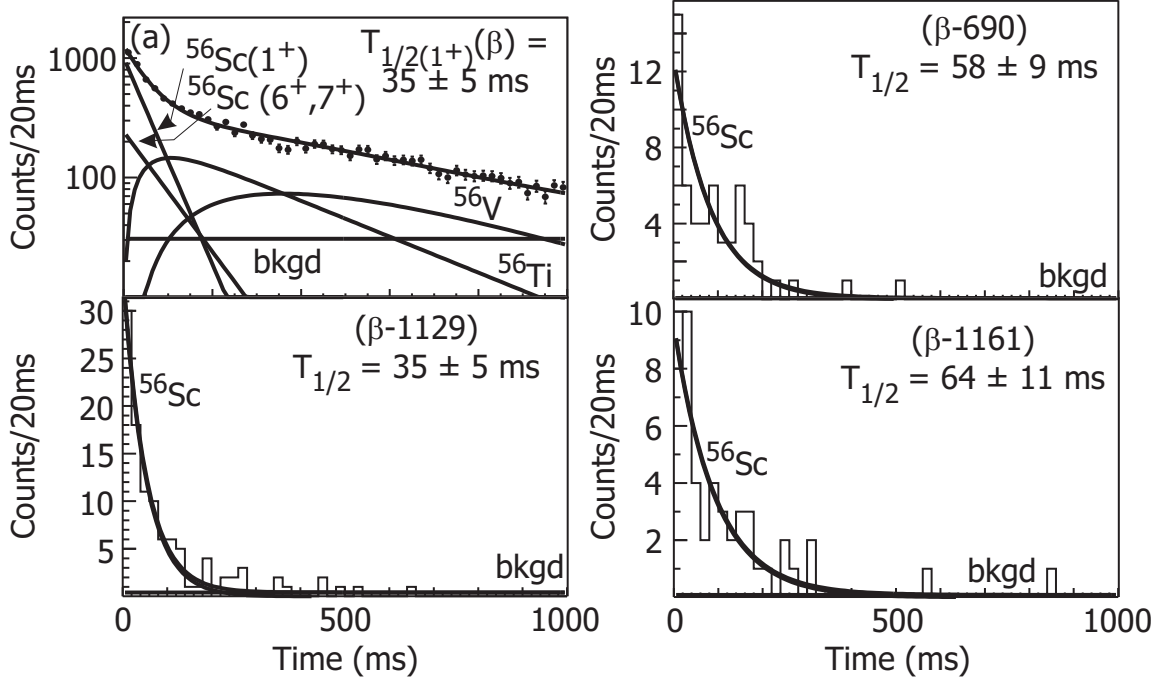
Figure 4.3: Decay curves for ^{56}Sc showing (a) fragment-β correlations where the data were fit with an exponential parent decay, an exponential growth and decay for both daughter and grand-daughter and a linear background, (b) fragment-β correlation with an additional requirement of a coincident 1129-keV γ ray, (c) fragment-β correlation with an additional requirement of a coincident 690-keV γ ray, (c) fragment-β correlation with an additional requirement of a coincident 1161-keV γ ray. Decay curves shown in (b-c) were fitted with an exponential decay and linear background.

$2_1^+ \rightarrow 0_1^+$ transition, it appears that a lower-spin ^{56}Sc state has a shorter half-life, and that the 1129-keV γ-gated decay curve is then a mixture reflecting both the low- and high-spin state half-lives. The percentages of β decays due to the low- and high-spin state are $(83 \pm 11)\%$ and $(20 \pm 4)\%$, respectively, based on absolute γ-ray intensities and the deduced β-feeding to the ^{56}Ti ground state.

The ^{56}Sc-correlated β-decay curve, Figure 4.3(a), was first fitted using a single exponential decay component for ^{56}Sc with daughter and grand-daughter generations. The resulting half-life is consistent with the previous determination [28]. However, evidence for two β-decaying states in ^{56}Sc resulted in a re-examination of the overall fragment-β decay curve. Since the half-life of the high-spin β-decaying state was extracted from the decay curves gated on the 690- and 1161-keV γ-ray transitions, the value for the low-spin half-life can be deduced from the total β-decay half-life
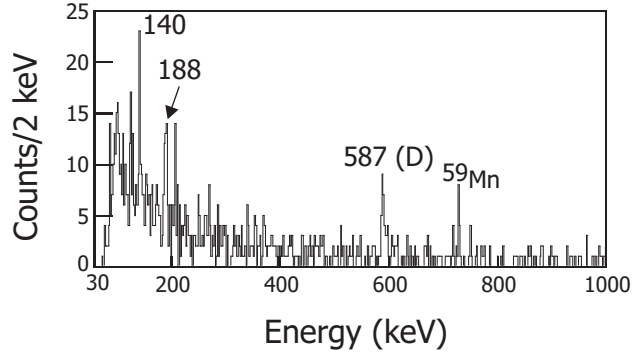
Figure 4.4: Isomeric γ-ray spectrum collected within a $20\mu s$ time window following a ^{56}Sc implanted ion.

curve. The decay curve in Figure 4.3(a) was fitted to a function that included the high-spin state half-life, along with the percentage of β decays attributed to the high- and low-spin states, the exponential growth and decay of the daughter and grand-daughter isotopes, ^{56}Ti [30] and ^{56}V [26], and a linear background component. In this way, a half-life of 35 ± 5 ms was deduced for the lower-spin state in ^{56}Sc. The isotopes ^{58,59}V, ^{57}Ti, and ^{60}Cr, which have previously measured half-lives, were implanted along with ^{56}Sc. The decay curves for these four isotopes were also fitted and used to verify the linear background.

The experiment as configured also permitted the detection of isomeric γ rays that decay following the implantation of a nucleus into the DSSD. The isomeric γ-ray spectrum collected within a 20-μs time window following a ^{56}Sc implanted ion is shown in Figure 4.4. Three transitions were observed at 140 ± 2, 188 ± 2, and 587 ± 2 keV with absolute γ-ray intensities of $(1.4 \pm 0.1)\%$, $(1.8 \pm 0.3)\%$, and $(2.2 \pm 0.6)\%$, respectively. It is possible that the 587-keV transition is a doublet. Unfortunately, the errors on the absolute intensities and the lack of coincidence data do not permit placement of any of the three isomeric transitions in the low-energy structure of ^{56}Sc at the present time.

The proposed decay scheme for levels in ^{56}Ti populated following the β decay of ^{56}Sc is shown in Figure 4.5. The β-decay Q value was derived from the mass excess

^{56}Sc

$T_{1/2} = 35 \pm 5$ ms $T_{1/2} = 60 \pm 7$ ms

(1^+) 0+x $(6^+,7^+)$ 0+y

$Q_\beta = 13.7 \pm 0.8$ MeV

n

592.3 [7]

592

S_n

0

^{55}Ti

(1^+) $(6^+,7^+)$

I_β(%) I_β(%)

-        100 (6^+) 690.1 [19]   2980

-        0 (4^+) 1160.5 [21]   2290

35±11   - (2^+) 1128.5 [48]   1129

65±13   - 0^+ 0

^{56}Ti
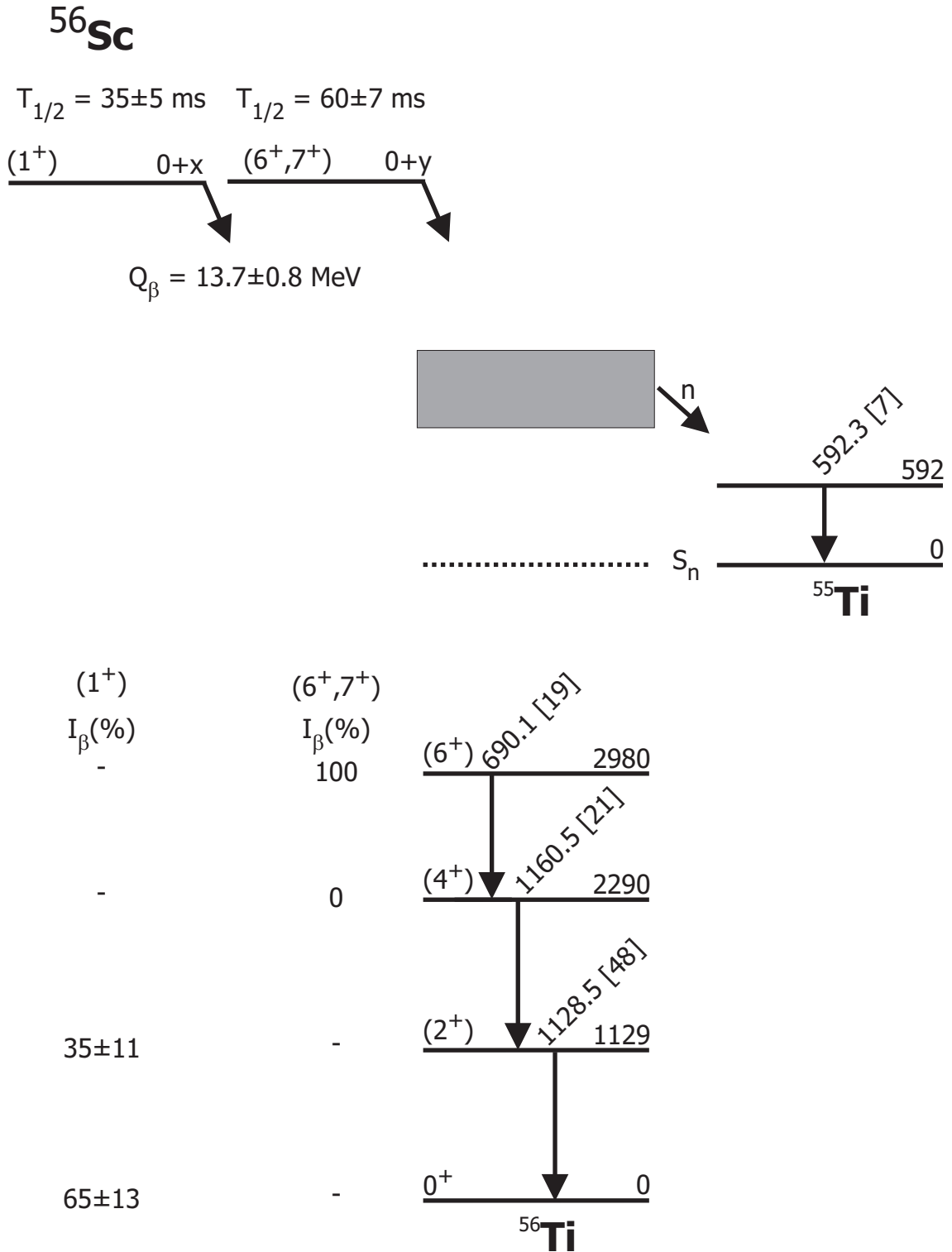
Figure 4.5: Proposed ^{56}Ti level scheme populated following the decay of ^{56}Sc. The number in brackets following the γ-ray decay energy is the absolute γ-ray intensity. The Q value was deduced from data in Ref. [32]. Absolute β-decay intensities are not shown due to the presence of a possible β-delayed neutron branch to states in ^{55}Ti (see text).
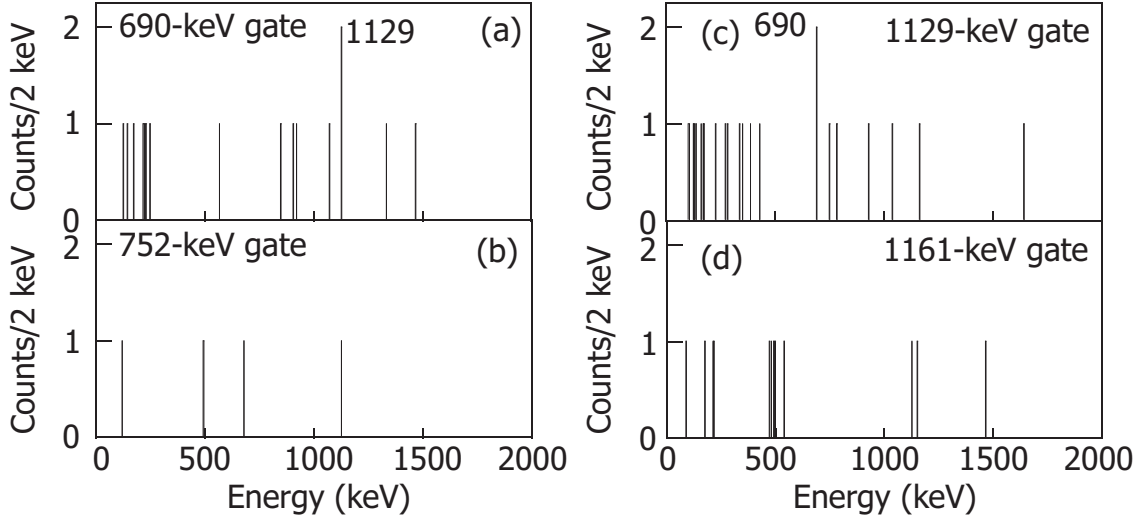
Figure 4.6: γ-γ coincidence data for the 690-, 752-, 1129-, and 1161-keV transitions following a ^{56}Sc β decay.

of both parent and daughter as compiled in Ref. [33]. Absolute γ-ray intensities were deduced from the number of observed ^{56}Ti γ rays, the simulated γ-ray efficiency curve, and the number of ^{56}Sc implanted ions correlated with β decays. The last term was derived from a fit of the decay curve in Figure 4.3(a) as described in section 3.3. Details of the γ ray placements and spin and parity assignments were aided by a complementary experiment carried out at the ATLAS accelerator at Argonne National Laboratory with the Gammasphere multi-detector array to study the yrast structure of neutron-rich Ti isotopes as described in Ref. [29]. Note that the placement of the 690-keV γ ray feeding the 1129-keV state in ^{56}Sc was also confirmed by fragment-$\beta\gamma\gamma$ coincidences (see Figure 4.6).

β feedings to levels in ^{56}Ti from both β -decaying states were deduced from the absolute γ-ray intensities, and are summarized in Figure 4.5. The apparent β feedings should be considered upper limits, based on the sizeable β-decay Q-value and the possible existence of unobserved γ decays below our detection limit of $\approx 6\%$ absolute intensity and the possibility of a β-delayed neutron branch to ^{55}Ti. From the intensity of the γ ray at 592 keV, a lower limit for the β-delayed neutron branch is 7%. This

56

Table 4.2: ^{58}V β delayed γ rays with absolute γ-ray intensities, initial and final states.

E_γ (keV)	I_γ^{abs} (%)	Initial State (keV)	Final State (keV)
879.8 ± 0.4	56 ± 3	880	0
1042.4 ± 0.7	2.2 ± 0.9		
1056.4 ± 0.4	23 ± 2	1936	880
1381.4 ± 0.4	2.3 ± 0.4		
1500.0 ± 0.5	2.1 ± 0.5		
1678.7 ± 0.6	1.7 ± 0.7		
2217.5 ± 0.4	8.2 ± 0.6	3097	1936
3123.4 ± 0.6	3.1 ± 0.8		

value compares reasonably well with the predicted P_n value of 12% from Ref. [34]. Apparent logft values for the observed β-decay branches are not quoted due to the uncertainties in the ordering of and energy differences between the low- and high-spin β-decaying states in ^{56}Sc. β-decay branching to the ^{56}Ti ground and first excited 2^+ state of ^{56}Ti led to the tentative assignment of 1^+ to the spin and parity of the parent ^{56}Sc low-spin β-decaying state. Apparent direct feeding to the 6^+, 2980-keV level in ^{56}Ti from the high-spin ^{56}Sc β-decaying state limits the spin of the high-spin isomeric state to values of 5, 6, or 7. Absence of direct β feeding to the 4_1^+ state (the absolute intensities of the 690- and 1161-keV transitions are equivalent within experimental errors) further restricts the spin of the ^{56}Sc high-spin β-decaying state to $J = (6, 7)$.

4.2 ^{58}V

The β-delayed γ-ray spectrum for ^{58}V in the range 0-3.6 MeV is shown in Figure 4.7(a,b). There are a total of eight γ rays observed in the spectrum, and they are listed along with their absolute γ-ray intensities in Table 4.2. Of these eight γ rays, those with energies of 880, 1042, 1056, 1500, and 2218 kev have been previously observed [26]. The γ ray reported at 1571 keV in Ref. [26] was unobserved in the current experiment and a revised energy of 1500 keV is assigned to the 1501 keV γ ray from Ref. [26]. Three new γ rays at 1381, 1679, and 3123 keV all have absolute
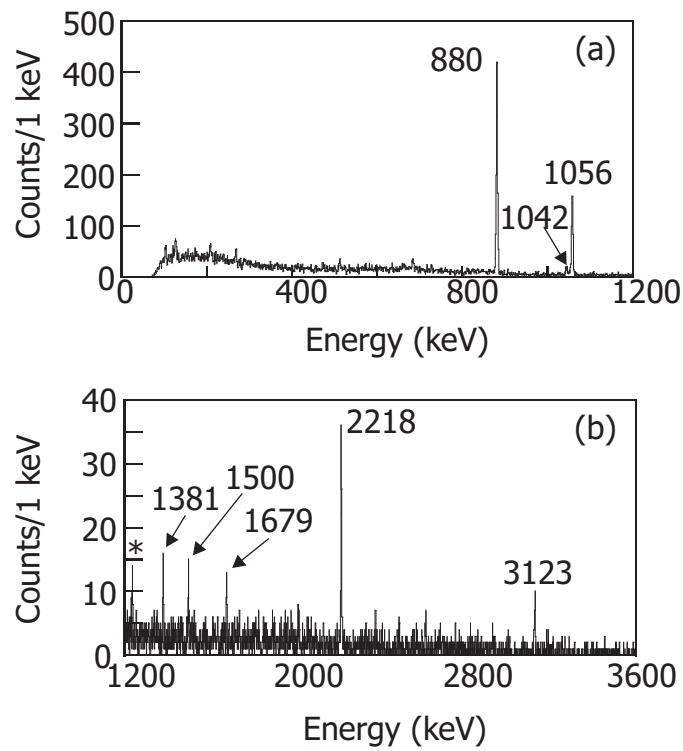
Figure 4.7: ^{58}V β-delayed γ-ray spectrum from (a) 0-1.2 and (b) 1.2-3.6 MeV for events occurring within one second after a ^{58}V implanted ion. The γ ray marked with an asterisk is from the decay of ^{59}Cr.
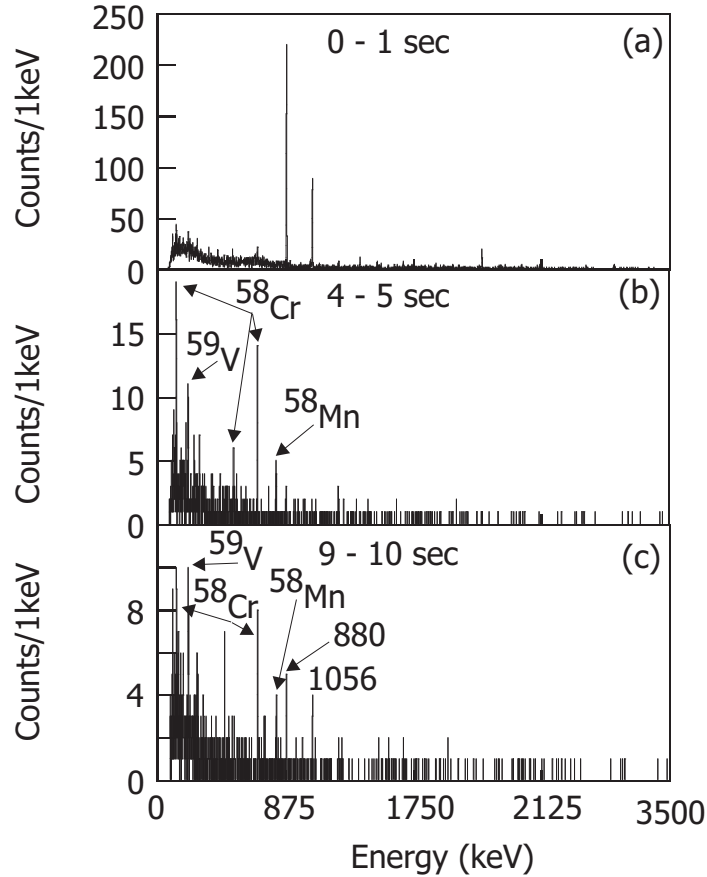
Figure 4.8: ^{58}V β-delayed γ spectra. The maximum correlation time and minimum time between implantation were both set to 10 s. Gates on subsets of the correlation time were created and applied to the $\beta\gamma$ spectrum. β-delayed γ-ray spectra are shown with an additional cut on the correlation time extending between (a) 0-1 s, (b) 4-5 s, and (c) 9-10 s.

intensities at or below 3%, which is lower than the detection limit in Ref. [26]. To determine whether any of these γ-ray transitions can be attributed to longer lived species, the correlation time and maximum time between implantation were both changed to ten seconds, and three different cuts on correlation time were applied to the $\beta\gamma$ spectrum. Time cuts between 0-1 s, 4-5 s, and 9-10 s resulted in the spectra shown in Figures 4.8(a,b,c). Prominent peaks located in Figures 4.8(b,c) can be identified with daughter and grand-daughter decays in the A=58 decay chain or with contamination from ^{59}V, due to an overlap in the particle ID gates.

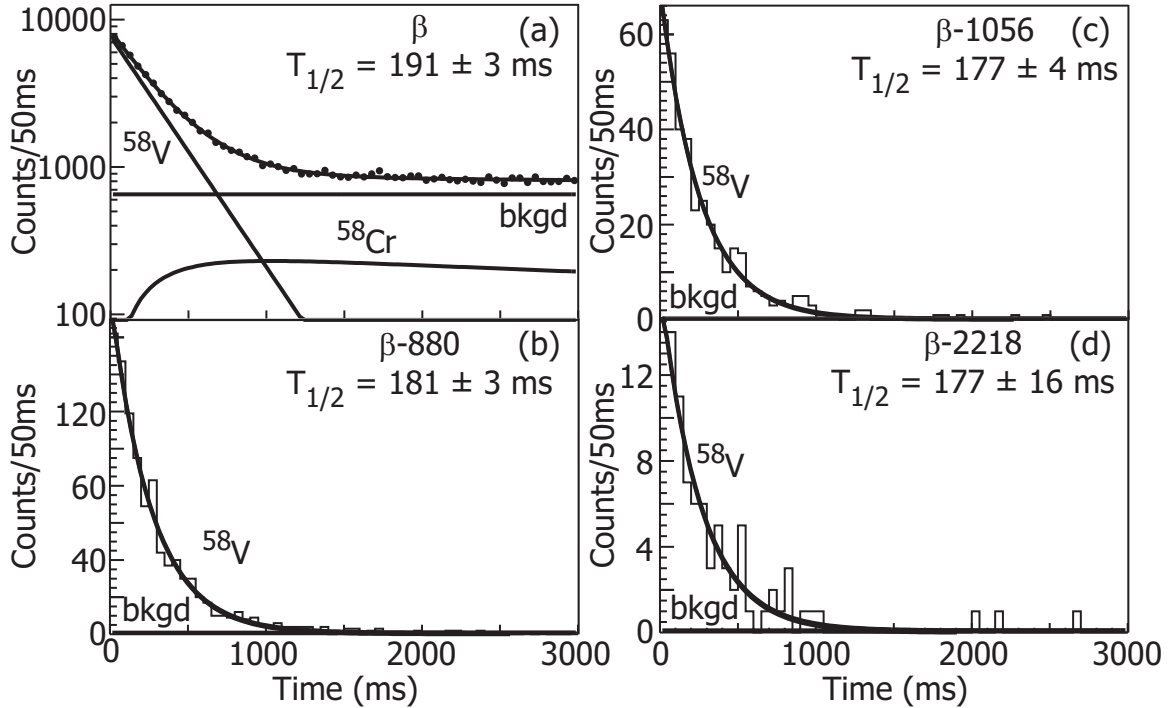The measured decay curves for ^{58}V β decays, along with γ-gated decay curves over

Figure 4.9: Decay curves for ^{58}V showing (a) fragment-β correlations where the data were fit with an exponential parent decay, an exponential growth and decay for the daughter ^{58}Cr and a linear background, (b) fragment-β correlation with an additional requirement of a coincident 880-keV γ ray, (c) fragment-β correlation with an additional requirement of a coincident 1056-keV γ ray, (c) fragment-β correlation with an additional requirement of a coincident 2218-keV γ ray. Decay curves shown in (b-c) were fitted with an exponential decay and linear background.

a three second correlation time were extracted, fit, and are shown in Figures 4.9(a-d). The ^{58}V decay curve shown in Figure 4.9(a) was fit with an exponential decay along with the exponential growth and decay of the daughter nuclide ^{58}Cr ($t_{1/2}$= 7s). The grand-daughter, ^{58}Mn ($t_{1/2}$= 3s), decay was found not to contribute to the half-life fit. A linear background was also included in the fit. A value of 191 ± 3 ms was extracted for the half-life of ^{58}V in agreement with previous values of 185 ± 10 ms [26], 205 ± 20 ms [35], and 200 ± 20 ms [36]. γ-gated decay curves for the 880-, 1056-, and 2218-keV γ-ray transitions are shown in Figure 4.9(b-d) and are all in agreement with each other, suggesting the absence of multiple isomeric β-decaying states in the ^{58}V parent.

The 880-keV transition has previously been assigned as the $2^+ \rightarrow 0^+$ transition in ^{58}Cr [26]. γ-γ coincidences were determined for the 880-, 1056-, and 2218-keV
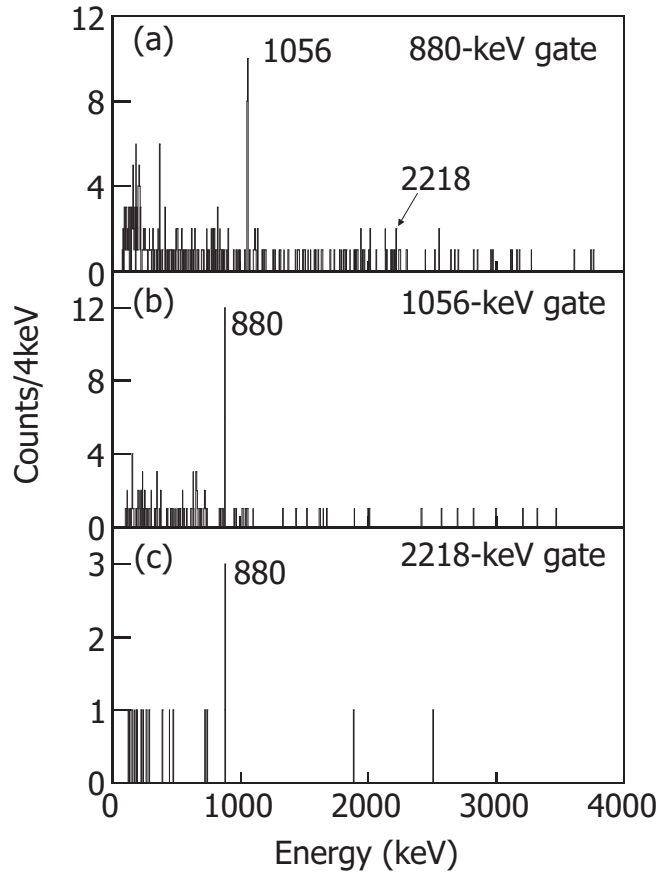
Figure 4.10: γ-γ coincidence data for the (a)880-, (b)1056-, and (c)2218-keV transitions following a ^{58}V β decay.

transitions and are shown in Figure 4.10. From the coincidence data it can be seen that both the 1056- and 2218-keV transitions feed the 880-keV 2^+ state. The ratio of intensities between the 1056- and 2218-keV transitions observed in the 880-keV coincidence spectrum agrees with the ratio between the 1056- and 2218-keV intensities observed in the $\beta\gamma$ spectrum suggesting the transitions are in parallel. Furthermore, based on the intensity of the 880-keV transition observed in the 1056-keV γ-gated coincidence spectrum (see Figure 4.10(b)), if the 2218-keV γ ray were in coincidence with the 1056-keV transition, a peak with an area of approximately seven counts would be present and is clearly absent in Figure 4.10(b). The coincidence spectra lead to the level scheme shown in Figure 4.11. From the number of ^{58}V β decays detected, the γ-ray intensity and the SeGA efficiency curve, the absolute intensity
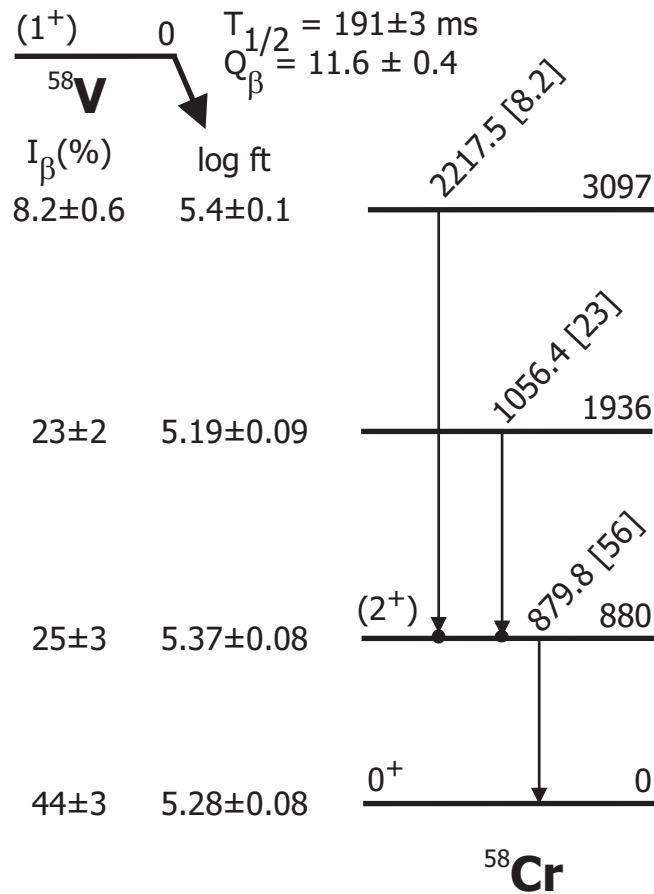
Figure 4.11: Proposed ^{58}Cr level scheme populated following the decay of ^{58}V. The number in brackets following the γ-ray decay energy is the absolute γ ray intensity. The Q value was deduced from data in Ref. [32]. Observed coincidences are represented as filled circles. Absolute β-decay intensity and logft values for the β decay to each state in ^{58}Cr is shown on the left of the figure.
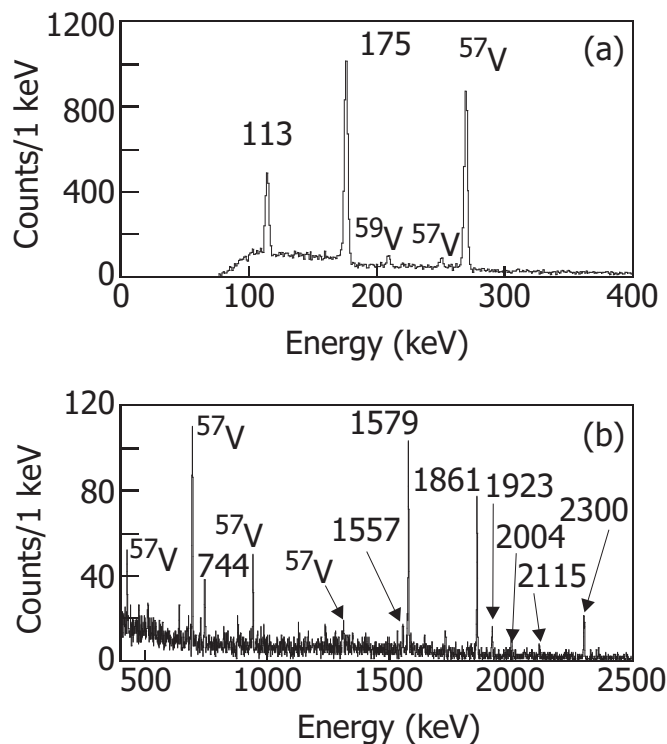
Figure 4.12: ^{57}Ti β-delayed γ-ray spectrum for events occurring within one second after a ^{57}Ti implanted ion from (a) 0-0.4 and (b) 0.4-2.5 MeV.

of a γ-ray transition can be determined. From the absolute intensity and the level scheme the apparent β-decay intensity to each state can be calculated along with an apparent logft value, using a β-decay Q value of 11.6 ± 0.4 MeV [32]. Supposing that the ^{58}V β decay proceeds through an allowed transition to both the 2^+ and 0^+ states of ^{58}Cr as indicated by the logft values, the parent ^{58}V ground state is most likely a 1^+ state.

4.3 ^{57}Ti

The β-delayed γ-ray spectrum for ^{57}Ti in the region of 0-2.5 MeV is shown in Figures 4.12(a,b). The spectrum includes all γ rays detected within one second after the implantation of a ^{57}Ti ion. Six γ rays, including two prominent ones located at 268 and 692 keV, have been assigned to the daughter decay of ^{57}V in a previous work [26].
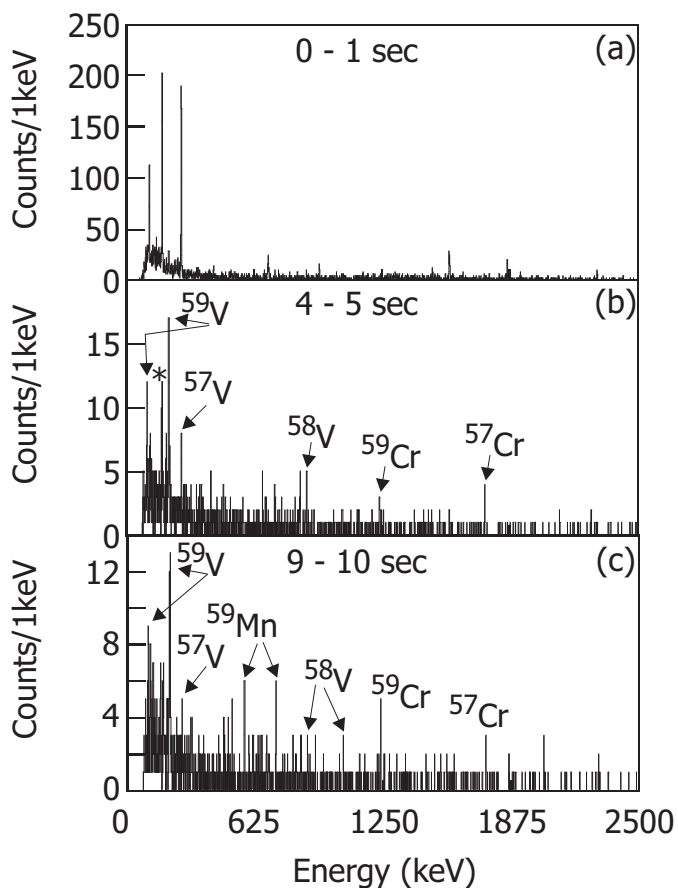
63

Figure 4.13: ^{57}Ti β-delayed γ spectra. The maximum correlation time and minimum time between implantation were set to 10 s. Gates were created on subsets of the maximum time and applied to the $\beta\gamma$ spectrum. β-delayed γ-ray spectra are shown with a cut on the correlation time extending between (a) 0-1 s, (b) 4-5 s, and (c) 9-10 s.

To observe decays with longer half-lives, cuts on the correlation time between 0-1 s, 4-5 s, and 9-10 s were again applied to the $\beta\gamma$ spectrum and the results are shown in Figure 4.13. The presence of γ rays belonging to the decay of ^{58,59}V can be explained by an overlap in the particle ID gates with ^{57}Ti. As there are no γ rays present in the 4-5 s and 9-10 s cuts that cannot be assigned to known transitions, the remaining γ rays in the $\beta\gamma$ spectrum were attributed to the decay of ^{57}Ti and are listed along with absolute intensities in Table 4.3. It should be noted that there are no γ rays in Table 4.3 that can be associated with ^{56}V. Therefore, it does not appear that there exists a delayed neutron branch which passes through the 2^+ state in ^{56}V.

Table 4.3: ^{57}Ti β-delayed γ-rays with absolute γ-ray intensities, along with initial and final states for those transitions placed in the level scheme.

E_γ (keV)	I_γ^{abs} (%)	Initial State (keV)	Final State (keV)
113.1 ± 0.4	14 ± 1	113	0
174.8 ± 0.4	31 ± 2	175	0
744.0 ± 0.4	2.3 ± 0.4	2475	1732
1557.3 ± 0.5	2.2 ± 0.5	1732	175
1579.4 ± 0.4	16 ± 2	1754	175
1861.5 ± 0.4	14 ± 2	2036	175
1922.9 ± 0.5	2.6 ± 0.5	2036	113
2003.7 ± 0.6	1.8 ± 0.5		
2114.6 ± 0.5	0.7 ± 0.3		
2300.4 ± 0.4	5.0 ± 0.5	2475	113

The half-life of ^{57}Ti deduced from a fit of the decay curve shown in Figure 4.14(a) is 98 ± 5 ms. Previous measurements of the ^{57}Ti half-life include 67 ± 25 ms [37], 180 ± 30 ms [36], and 56 ± 20 ms [38]. However all three of these measurements isolated ^{57}Ti in only very small quantities. The half-life fit includes the exponential decay of the parent, exponential growth and decay of the daughter, ^{57}V, and a linear background term. The half-life of the daughter, ^{57}V, was taken to be 350 ms as reported in Ref. [26]. The γ-gated half-lives from the decay of ^{57}Ti are shown in Figures 4.14(b-h) and Figures 4.15(a-b). All γ-gated half-lives were fit with an exponential decay and linear background component and are consistent, within errors, with the half-life determined without any γ-ray coincidence, further aiding their assignment to the decay of ^{57}Ti. Furthermore, based on the consistency of γ-gated half-lives there is no reason to suspect multiple β-decaying states.

A $\gamma\gamma$ matrix was created to identify coincidences between the observed γ rays. Coincidence spectra for various ^{57}Ti γ rays were extracted and are shown in Figure 4.16. Based on the efficiency-corrected intensity ratios between the 113- and 175-keV peaks in 1579- and 1861-keV γ-gated coincidence spectra, approximately 50% in both cases, the 113- and 175-keV transitions were placed in parallel. From an inspection of the 1923-keV coincidence spectrum, the 1923-keV transition has been placed directly
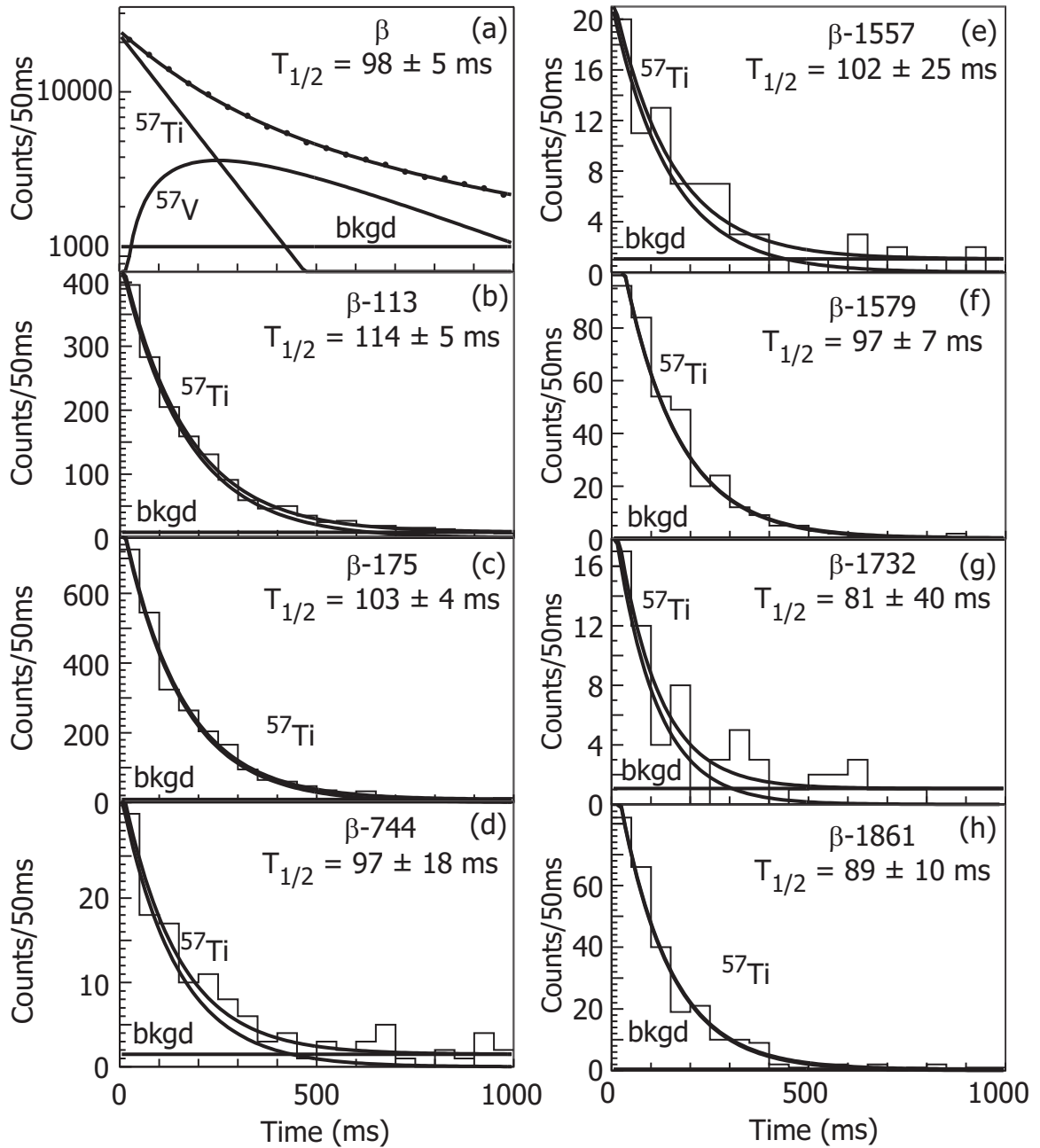
Figure 4.14: Decay curves for ^{57}Ti showing (a) fragment-β correlations where the data were fit with an exponential parent decay, an exponential growth and decay for the daughter ^{57}V and a linear background and (b-j) fragment-β correlations with an additional requirement of a coincident gamma ray with an energy of (b) 113 keV, (c)175 keV, (d) 744 keV, (e) 1557 keV, (f) 1579 keV, (g) 1732 keV, (h) 1861 keV. Decay curves shown in (b-h) were fitted with an exponential decay and linear background.
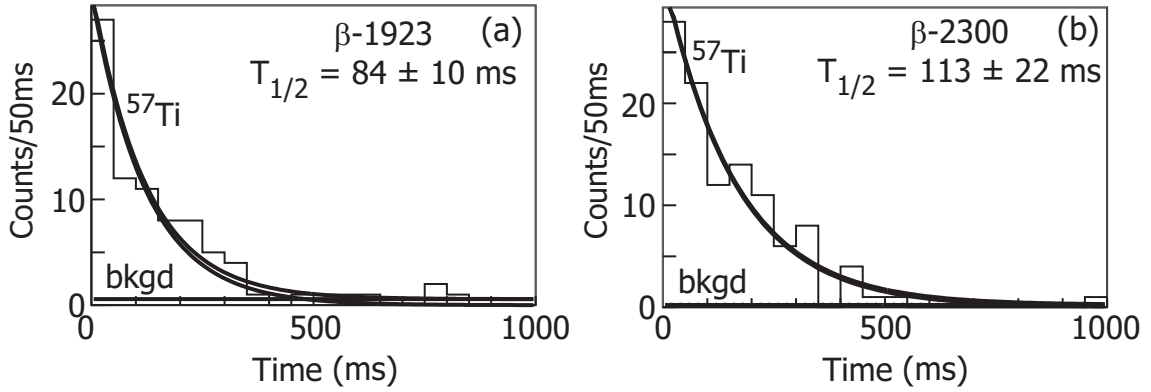
Figure 4.15: Decay curves for ^{57}Ti showing fragment-β correlations with an additional requirement of a coincident gamma ray with an energy of (a) 1923 keV and (b) 2300 keV. Decay curves shown in (a) and (b) were fitted with an exponential decay and linear background.

feeding the 113-keV state due to the absence of a 175-keV coincidence peak, which would be expected to be twice as strong as the 113-keV transition, based on intensity ratios observed in the 1579- and 1861-keV coincidence spectra. The absence of either the 113- or 175-keV transition in the 1732-keV gated coincidence spectrum, which does display a coincidence with 744, establishes the 1732-keV level. The level scheme constructed from the coincidence data is shown in Figure 4.17. Since the 113- and 175-keV transitions are in parallel there should be a transition of 62 keV between the 175- and 113-keV states in order for both energies to appear in the 1579 and 1861 coincidence spectra. Such a transition would have been below the hardware thresholds of the SeGA array and, therefore, not observed. Additionally, such a low energy γ ray would probably be highly converted. The spin and parity assignments of ^{57}Ti and ^{57}V will be discussed in the next chapter in after comparison to theoretical calculations.

The only concern is with the 113- and 175-keV coincidence spectra. The coincidence spectrum for the 175-keV transition displays a peak located at 113 keV and vice versa. A determination of whether these two γ rays are truly in coincidence was made by inspecting intensity ratios between different transitions in the two separate spectra . Supposing the 113- and 175-keV transitions are in series, a gate placed on 175 keV should reveal a one-to-one ratio between the efficiency corrected areas of the
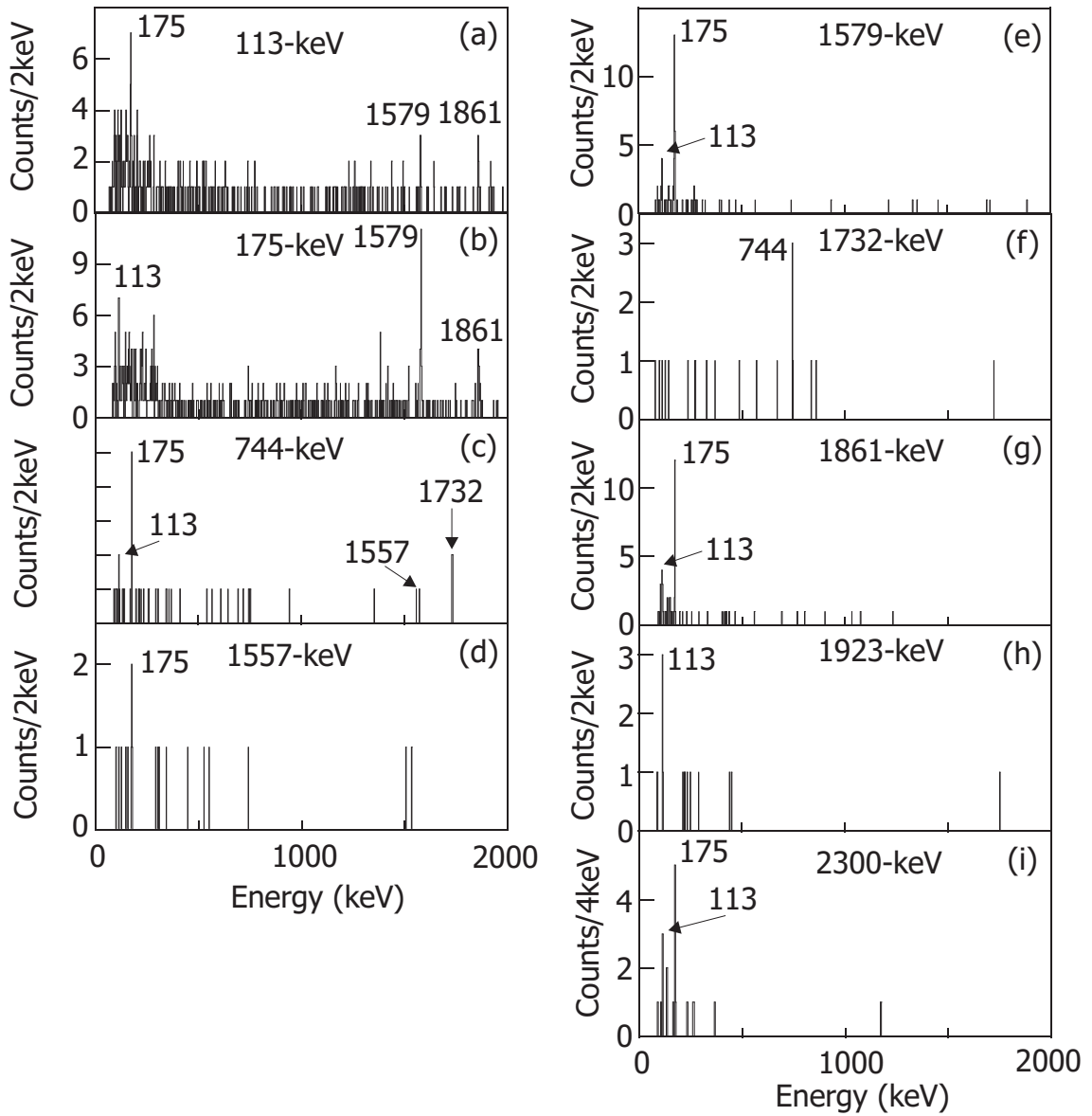
Figure 4.16: γ-γ coincidence data for the (a)113-, (b)175-, (c)744-, (d)1557-, (e)1579-, (f)1732-, (g)1861-, (h)1923-, and (f)2300-keV transitions following a ^{57}Ti β decay.
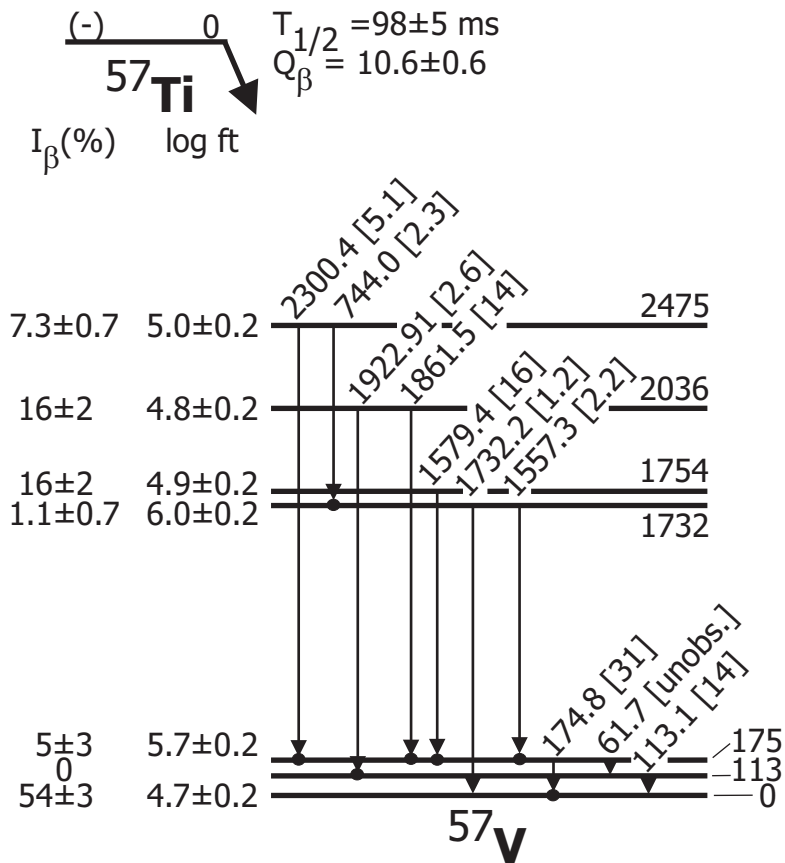
Figure 4.17: Proposed ^{57}V level scheme populated following the decay of ^{57}Ti. The number in brackets following the γ-ray decay energy is the absolute γ-ray intensity. The Q value was deduced from data in Ref. [32]. Observed coincidences are represented as filled circles. Absolute β decay intensity and apparent logft values for the β decay to each state in ^{57}V is shown on the left of the figure.

Table 4.4: Ratio between the efficiency corrected areas of the 113- and 175-keV transitions to the 1579-keV transition. If 113- and 175-keV transitions are in series the ratio should be 1. Areas are efficiency corrected.

175-keV spectrum		113-keV spectrum	
E_γ (keV)	Area	E_γ	Area
113	104 ± 59	175	87 ± 20
1579	490 ± 74	1579	172 ± 25
Ratio $= 0.21 \pm 0.12$		Ratio $= 0.5 \pm 0.2$	

Table 4.5: Calculated ^{57}Ti internal conversion coefficients from Ref. [2].

Energy (keV)	E1	E2	E3	E4	M1	M2	M3	M4
113	0.022	0.24	2.2	19	0.016	0.16	1.4	13
175	0.0058	0.044	0.28	1.8	0.0054	0.036	0.22	1.5

1579- and 113-keV peaks. What is found is that the 113 keV area is approximately 20% of the expected 1:1 ratio, see Table 4.4. It is unlikely that internal conversion could make up for the difference in intensities (see Table 4.5). Similarly, if a gate is placed on the 113 keV transition the 175-keV peak is not in a 1:1 intensity ratio with the 1579 keV peak. Therefore, the 113 and 175 keV transitions are most likely in parallel and they appear in coincidence only due to random coincidence.

4.3.1 ^{57}V

Through the decay of ^{57}Ti it was also possible to study the decay of the daughter nuclide ^{57}V. The delayed γ rays of ^{57}V appear in Figure 4.12 as a daughter activity. This nuclide has been previously studied [26], and a level scheme was constructed based on sum energy relationships and the fact that none of the three most intense transitions were in coincidence. With the greater statistics in the present experiment, a coincidence spectrum was extracted by gating on the 268-keV transition and is presented in Figure 4.18. The coincidences between the 268-keV transition and the 424- and 1314-keV transitions can be seen, confirming the placement of these γ transitions in the level scheme reported in [26].
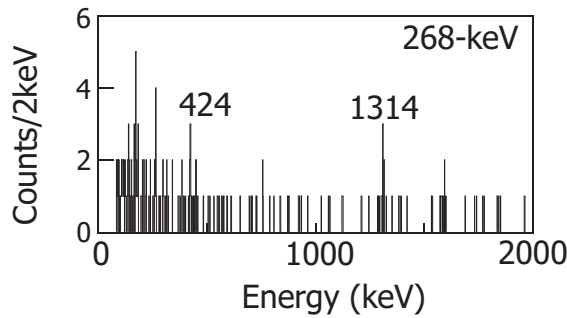
70

Figure 4.18: γ-γ coincidence data for the 268-keV transition following a ^{57}V β decay.

4.4 ^{59}V

The β-delayed γ-ray spectrum for those events observed within one second after a ^{59}V implanted ion is shown, in the energy range of 0-3 MeV, in Figures 4.19(a,b,c). Numerous γ-ray transitions are observed in this spectrum and are listed in Table 4.6. Of the γ rays listed in Table 4.6, the ones at 102 and 208 keV have been observed in previous studies of the β and isomeric decay of ^{59}V and ^{59m}Cr, respectively [37,39].

To determine if any of the transitions originate from longer lived species three different gates on the correlation time were applied to the $\beta\gamma$ spectrum between 0-1 s, 4-5 s and 9-10 s, and are shown in Figure 4.20. From the time-gated $\beta\gamma$ spectrum there are multiple γ-ray transitions that can be assigned to daughter activities. The 112-, 662-, 1126-, 1238- and 1899-keV transitions were assigned to the decay of ^{59}Cr. The γ rays at 112- and 1238-keV have been previously observed [40, 41]. The transitions located at 472, 570, 590, and 726 keV can be assigned to the decay of ^{59}Mn. Further confirmation of the assignments to daughter and grand-daughter decays were obtained from a comparison between the Ge spectrum taken with, and without, back-to-back decay rejection. In such a comparison, γ-ray transitions belonging to the daughter and grand-daughter nuclei in the A = 59 decay chain were identified by changes in intensity. The changes in intensity with, and without, back-to-back decays as compared to the 606-keV transition are shown in Table 4.7 for the 472, 662, 1126,
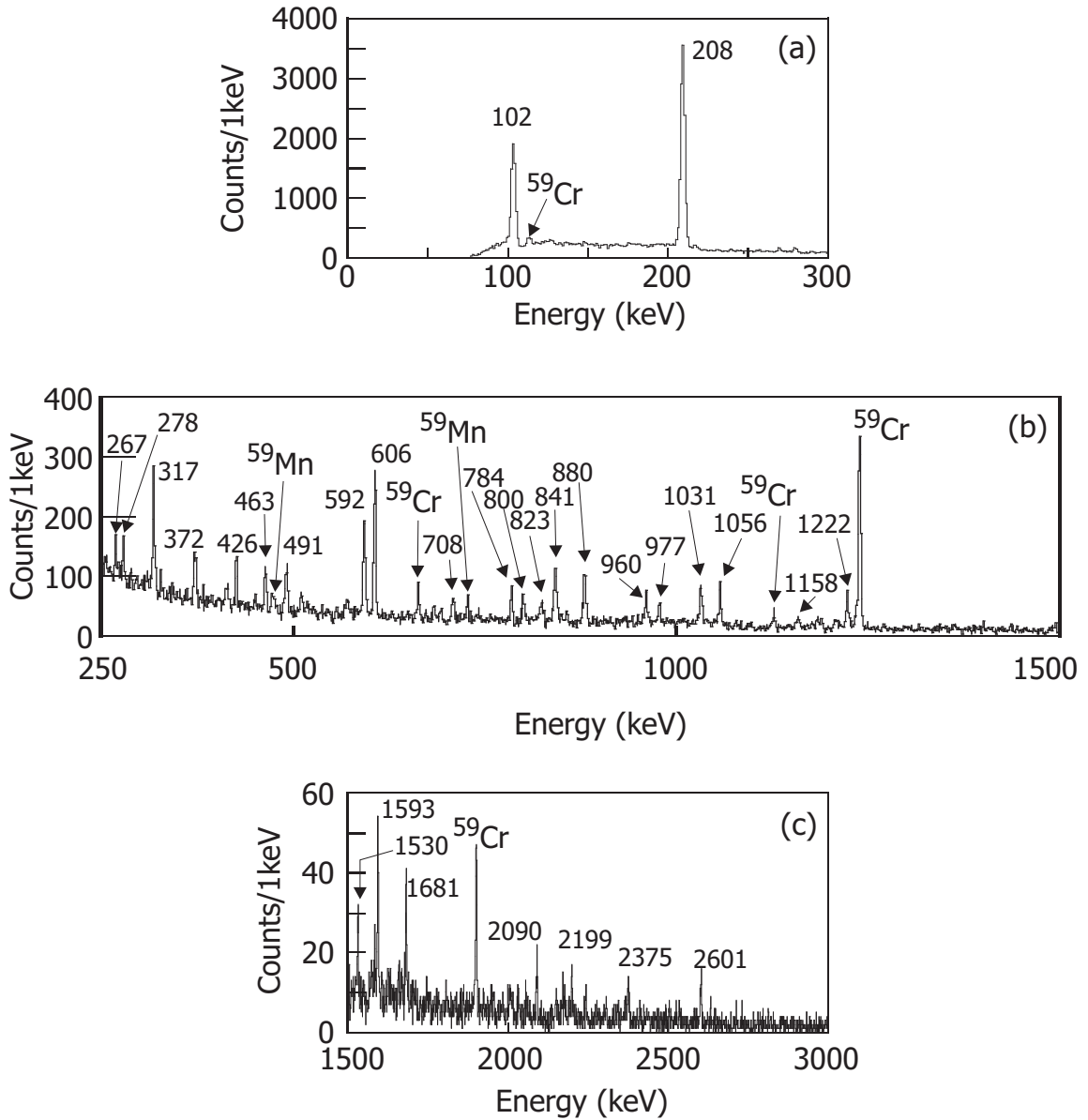
Figure 4.19: ^{59}V β-delayed γ rays in the range (a) 0-0.3, (b) 0.25-1.5, and (c) 1.5-3.0 MeV for events occurring within one second after a ^{59}V implanted ion. Numerous transitions from daughter and grand-daughter generations can be observed.

Table 4.6: ^{59}V β-delayed γ-rays with absolute γ ray intensities, and initial and final states for those transitions that were placed into the ^{59}Cr level scheme.

Energy (keV)	I_γ^{abs} (%)	Initial State (keV)	Final State (keV)
102.0 ± 0.4	21 ± 2	310	208
207.8 ± 0.4	41 ± 3	208	0
317.3 ± 0.4	3.0 ± 0.4	525	208
371.7 ± 0.5	1.6 ± 0.3		
425.5 ± 0.4	1.7 ± 0.3	1341	915
490.8 ± 0.5	2.3 ± 0.4	800	310
592.4 ± 0.4	4.2 ± 0.3	800	208
606.0 ± 0.4	6.4 ± 0.4	915	310
707.6 ± 0.5	1.1 ± 0.3	915	208
784.1 ± 0.4	1.8 ± 0.3		
799.9 ± 0.5	1.1 ± 0.3	800	0
823.2 ± 0.6	1.1 ± 0.3		
841.4 ± 0.4	2.7 ± 0.3	1366	525
879.9 ± 0.5	3.0 ± 0.4		
959.9 ± 0.4	2.2 ± 0.3		
977.2 ± 0.5	1.4 ± 0.2	2509	1532
1030.8 ± 0.4	2.4 ± 0.3	1341	310
1056.0 ± 0.4	2.5 ± 0.3	1366	310
1157.8 ± 0.5	0.8 ± 0.2	1366	208
1206.5 ± 0.6	0.6 ± 0.2		
1222.1 ± 0.4	2.5 ± 0.3	1532	310
1529.6 ± 0.5	1.0 ± 0.3		
1593.4 ± 0.5	2.2 ± 0.4	2509	915
1680.9 ± 0.5	1.9 ± 0.3		
2089.6 ± 0.5	0.9 ± 0.2		
2198.7 ± 0.5	0.5 ± 0.2	2509	310
2375.0 ± 0.6	0.8 ± 0.2		
2601.3 ± 0.6	1.2 ± 0.2		
2812.5 ± 0.5	0.2 ± 0.1		

1238,and 1899-keV transitions. The statistics in the Ge spectrum using back-to-back decay rejection were too low to identify the peaks at 570, 590, 726 and 112 keV.

Since ^{59}V was produced in copious amounts, it was possible to deduce γ-gated half-lives for most of the observed γ-ray transitions. These γ-gated half-lives are shown in Figures 4.21,4.22, and 4.23. The ^{59}V half-life deduced from the γ-gated decay curves is 97 ± 2 ms.

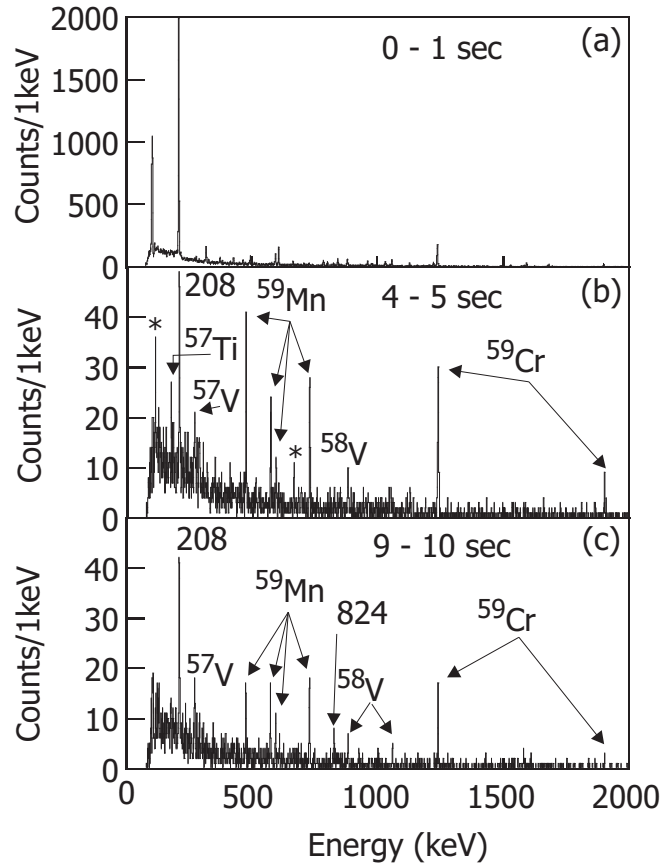The γ-gated decay curves shown in Figure 4.24 are those associated with ^{59}Cr and

Figure 4.20: ^{59}V β-delayed γ spectra The maximum correlation time and minimum time between implantation were set to 10 s. Gates were created on subsets of the maximum time and applied to the $\beta\gamma$ spectrum. β-delayed γ-ray spectra are shown with a cut on the correlation time extending between (a) 0-1 s, (b) 4-5 s, and (c) 9-10 s. The asterisks in (b) are due to ^{59}Cr decay.

^{59}Mn decays. With the exception of the 1238-keV transition, all of the γ rays were fairly weak and it is unknown why the decay curves in Figure 4.24(a-e,g) do not show the expected growth of a daughter or grand-daughter at small correlation times.

The γ-gated half-life spectra for the 880- and 1056-keV lines are both slightly longer than the other γ-gated half-lives. Transitions at 800- and 1056-keV are also observed following the β decay of ^{58}V. The difference in the half-lives of the 880- and 1056-keV transitions, compared to the other γ gated half-lives, may be due to ^{58}V contamination in the particle ID. In an attempt to eliminate possible contamination from ^{58}V, a restricted particle ID was placed on the central portion of the ^{59}V particle

Figure 4.21: Decay curves for ^{59}V showing (a-h) fragment-β correlations with an additional requirement of a coincident gamma ray with an energy of (a) 102 keV, (b) 208 keV, (c) 317 keV, (d) 372 keV, (e) 426 keV, (f) 463 keV, (g) 491 keV, and (h) 592 keV. Decay curves shown in (a-h) were fitted with an exponential decay and linear background.

Figure 4.22: Decay curves for ^{59}V showing (a-h) fragment-β correlations with an additional requirement of a coincident gamma ray with an energy of (a) 606 keV, (b) 708 keV, (c) 784 keV, (d) 800 keV, (e) 823 keV, (f) 841 keV, (g) 880 keV, and (h) 960 keV. Decay curves shown in (a-h) were fitted with an exponential decay and linear background.
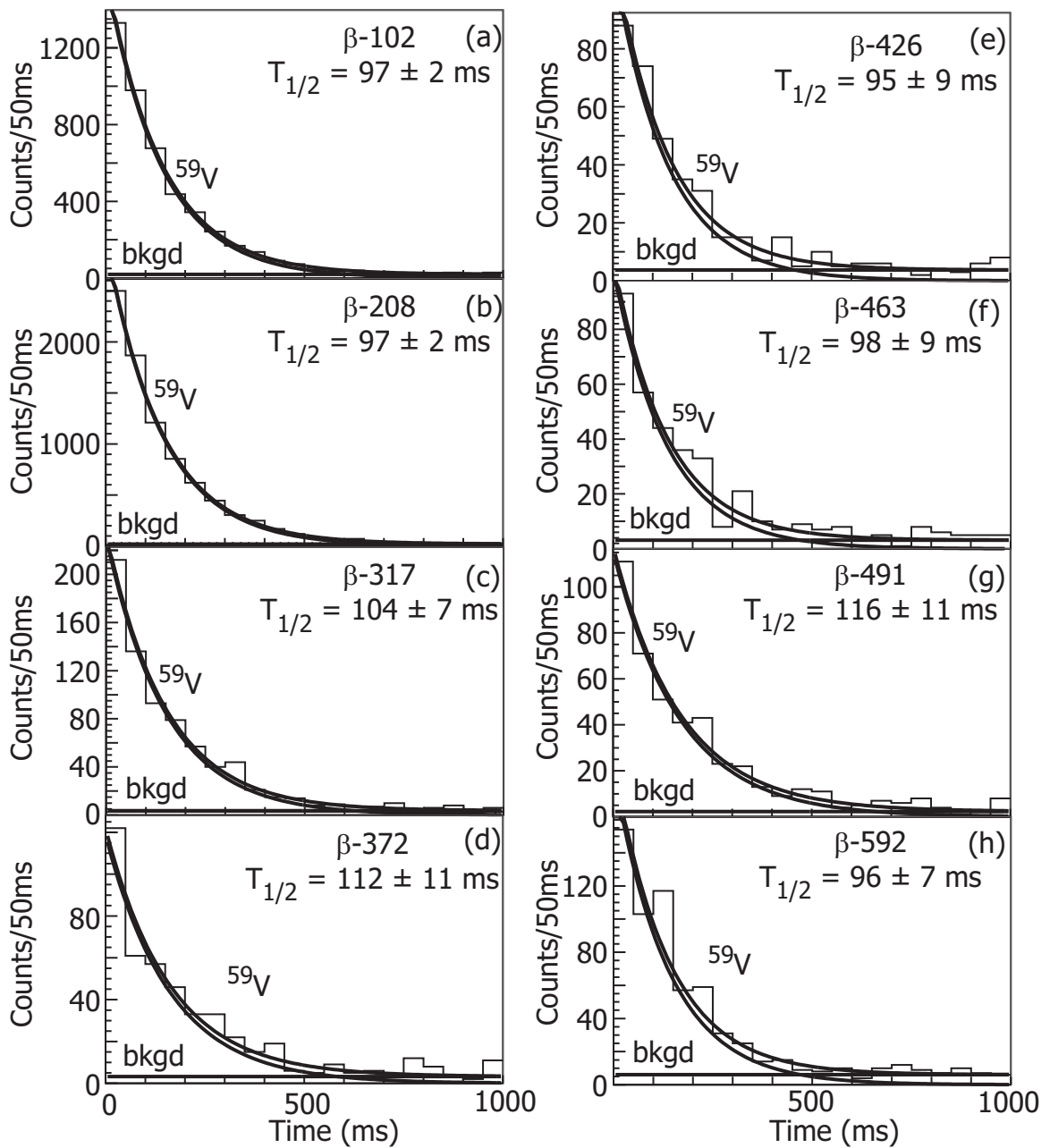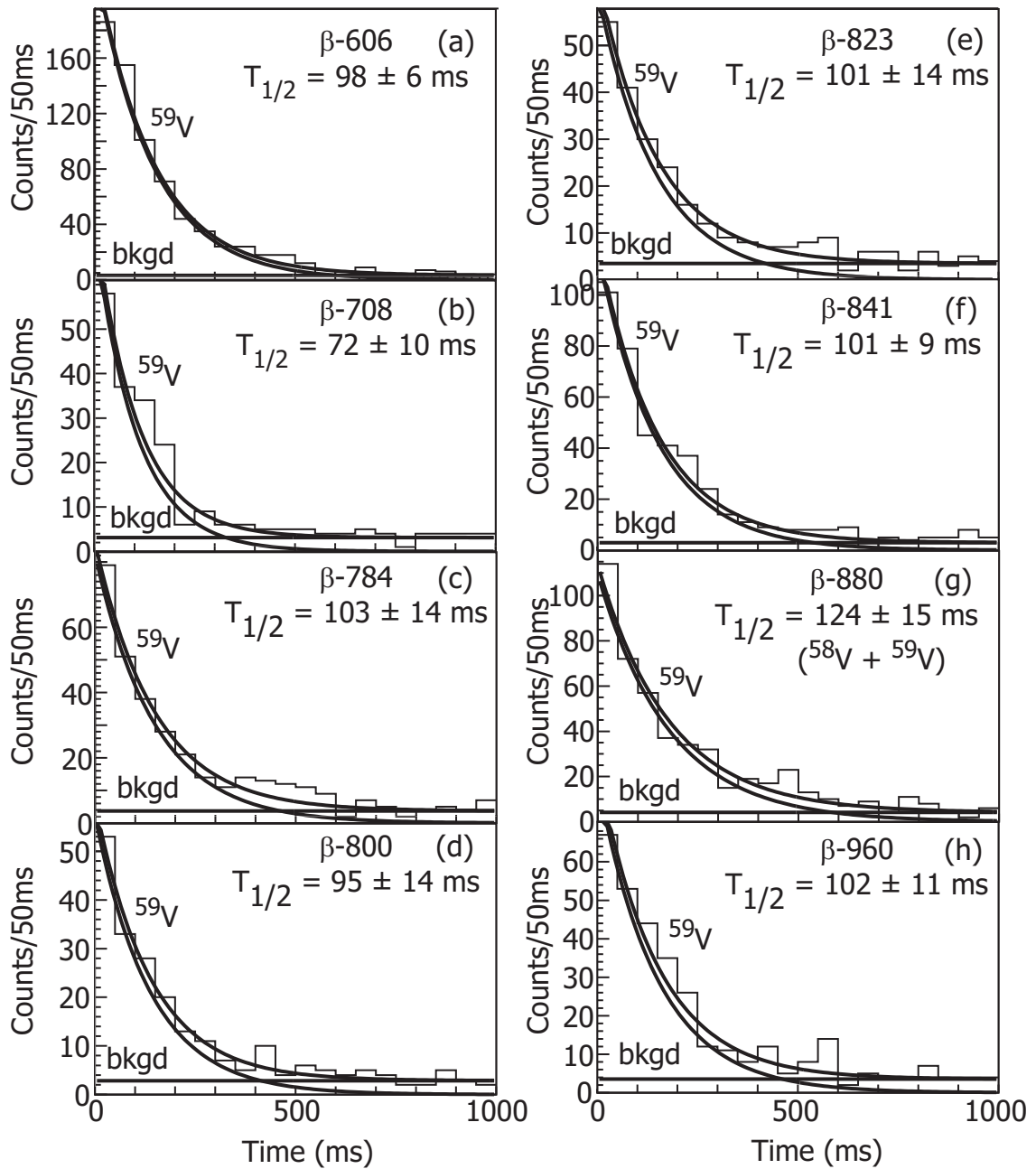
Figure 4.23: Decay curves for ^{59}V showing (a-f) fragment-β correlations with an additional requirement of a coincident gamma ray with an energy of (a)977, (b) 1031 keV, (c) 1056 keV, (d) 1222 keV, (e) 1530 keV, (f) 1593 keV, and (g) 1681 keV. Decay curves shown in (a-g) were fitted with an exponential decay and linear background.
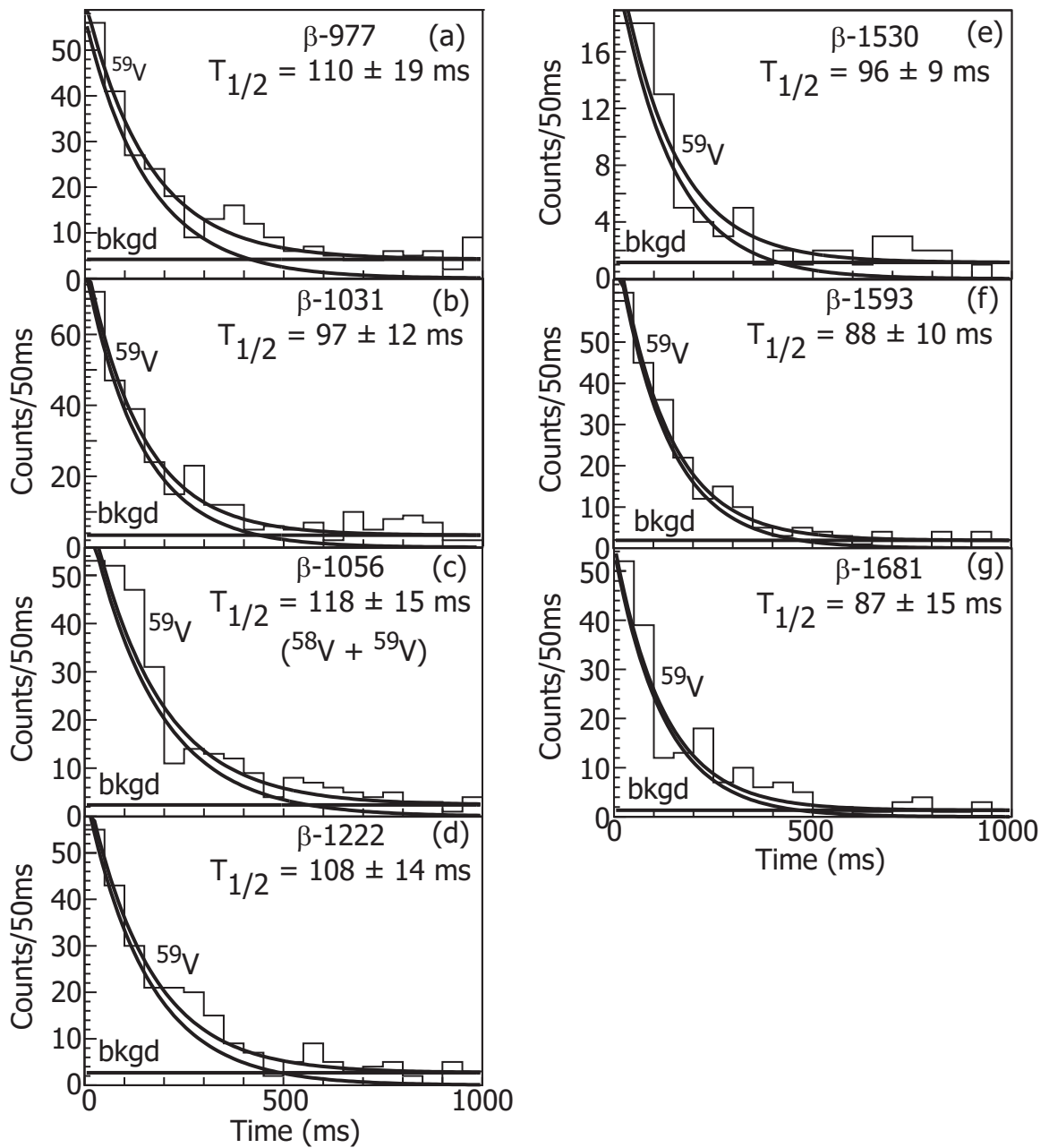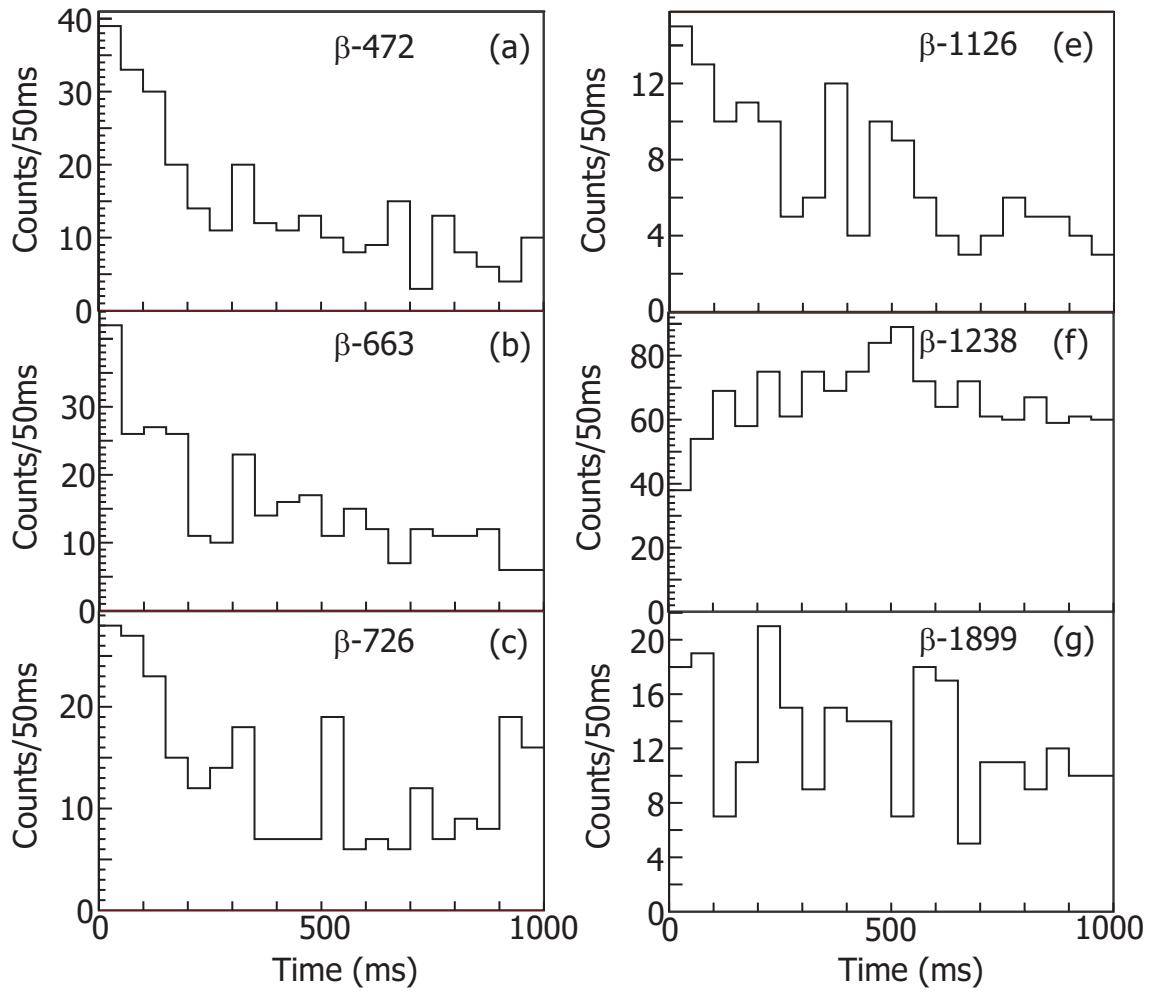
Figure 4.24: Decay curves showing (a-g) fragment-β correlations with an additional requirement of a coincident gamma ray with an energy of (a) 472 keV, (b) 663 keV, (c) 726 keV, (d) 1126 keV, (e) 1238 keV, and (f) 1899 keV.

Table 4.7: Ratio of peak intensities between Ge spectra without and with back-to-back decay rejection relative to the increase observed for the 606-keV transition. γ rays that can be assigned to daughter or grand-daughter transitions show a dramatic increase in peak intensity.

Energy (keV)	Ratio	Source
102.0 ± 0.4	1.01 ± 0.08	^{59}V
207.8 ± 0.4	1.00 ± 0.06	^{59}V
592.4 ± 0.4	0.99 ± 0.09	^{59}V
472.9 ± 0.5	1.6 ± 0.6	^{59}Mn
662.6 ± 0.4	1.4 ± 0.4	^{59}Cr
1126.5 ± 0.5	1.6 ± 1.8	^{59}Cr
1238.0 ± 0.4	1.6 ± 0.2	^{59}Cr
1899.5 ± 0.5	1.5 ± 0.3	^{59}Cr

ID gate. The 880- and 1056-keV transitions are still observed following the decay of ^{59}V. Additionally, the intensity of the 1056-keV transition is higher than that of the 880-keV transition. The 1056-keV transition was also observed in coincidence with ^{59}V γ rays and thus can conclusively be placed as following the decay of ^{59}V. The 880-keV transition, not in coincidence with any ^{59}V γ ray, may result from a possible β-delayed neutron branch into the 2_1^+ state of ^{58}V. If such a branch exists, the P_n value for ^{59}V would be $\sim$3%. This value is a lower limit as it is determined based on the observed γ-ray intensity of the $2^+ \rightarrow 0^+$ transition in ^{58}V.

A fit of the fragment-β decay curve was complicated by the relatively poor knowledge of the daughter, ^{59}Cr, half-life. The first measurement of the ^{59}Cr half-life, 740 ± 240 [40, 41], was obtained from an average of the γ-gated half-lives of 1.0 ± 0.4 s and 0.6 ± 0.3 s, for the 1238- and 112-keV γ-rays, respectively, weighted by relative intensities. The second measurement conducted on ^{59}Cr resulted in a half-life of 460 ± 46 ms [42]. The inconsistency of these two results made it difficult to fit the half-life of the ^{59}V parent. In an attempt to determined the half-life of ^{59}Cr the 1238-keV γ-gated decay curve from 0-5 s was fit and the results are shown in Figures 4.25(a-b). When the decay curve in 4.25(a) was fit with no restriction on the half-life of the ^{59}V parent, the deduced half-life for ^{59}Cr is 1100 ± 200 ms and the fitted half-
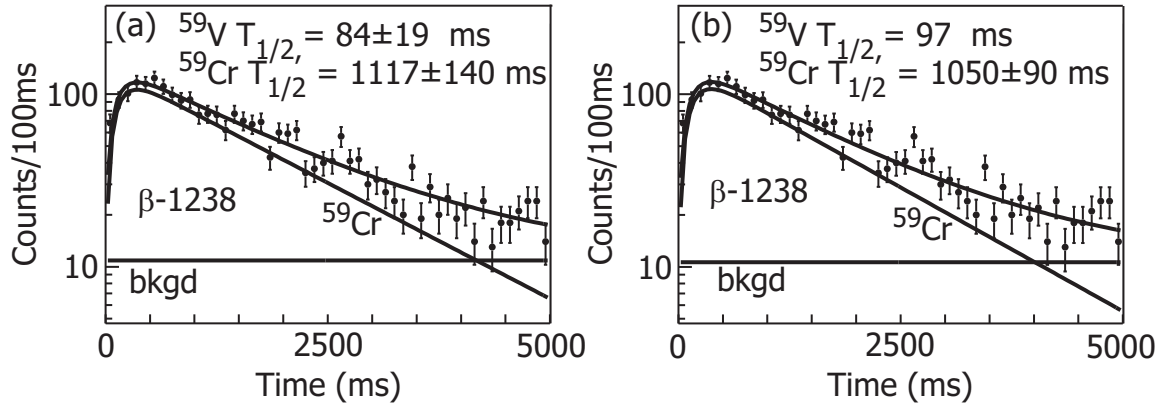
Figure 4.25: Decay curve showing fragment-β correlations with an additional requirement of a coincident gamma ray with an energy of 1238 keV. Fit includes the exponential growth and decay of the daughter ^{59}Cr with a linear background. In (a) the ^{59}V half-life was a variable in the fit, in (b) it was constrained to 97 ms.
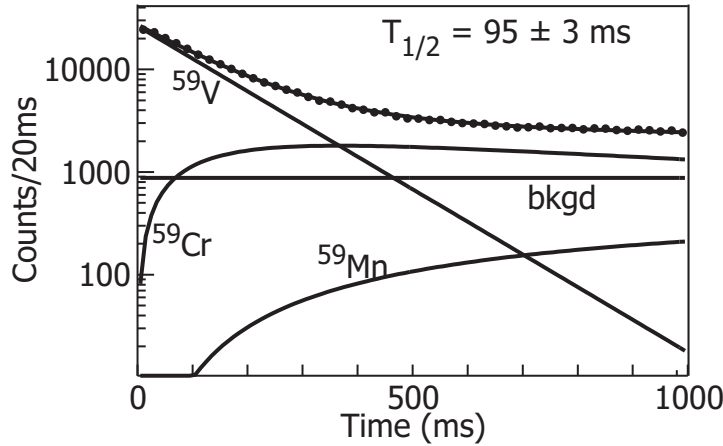
Figure 4.26: Decay curve showing fragment-β correlations for events occurring within one second after a ^{59}V implanted ion. The decay curve is fit with an exponential decay of the parent, growth and decay of the daughter and grand-daughter and a linear background term. The half-life of the daughter was set to 1100 ms deduced from the γ gated decay curve fit of the 1238-keV transition.

life for ^{59}V (84 ± 19 ms) agrees, within error, with most of the ^{59}V γ-gated half-lives. The decay curve in 4.25(b) was fit, restricting the parent half-life to 97 ms, taken from a weighted average of all γ gated half-lives; a ^{59}Cr half-life of 1050 ± 90 ms was deduced. From a weighted average of the two 1238-keV γ ray fits, the half-life of ^{59}Cr was adopted to be 1100 ± 100 ms. The adopted ^{59}Cr half-life was then used to fit the ^{59}V fragment-β decay curve, shown in Figure 4.26, leading to a half-life of 95 ± 3 ms for ^{59}V. Taking a weighted average of the 95 ± 3 half-life with the γ-gated half-lives

resulted in a value of 97 ± 2 ms, adopted for the the ^{59}V half-life. Previous values of the half-life include 130 ± 20 ms [36] and 75 ± 7 ms [37] but both studies suffered from a lack of statistics and used an imprecise value for the ^{59}Cr half-life.

$\gamma\gamma$ coincidence spectra for transitions in ^{59}V are shown in Figures 4.27, 4.28, and 4.29. The γ rays with energies of 102 and 208 keV had been identified and placed into a level scheme previously [37] with the 102- and 208-keV transitions in series. The series placement of these two γ rays, with the lowest excited state at an energy of 208 keV, was confirmed using the $\gamma\gamma$ coincidence spectra for ^{59}V. In particular, the γ rays at 317, 592, and 707 are present only in the 208-keV γ-gated spectrum, and the coincidence spectra gated on the 317-, 592-, and 707-keV transitions only show a coincidence with the 208-keV transition not with the 102-keV transition, placing the 208-keV state at the bottom of the level scheme. The ordering is in contrast to the recent findings of Ref. [43] where the 102- and 208-keV transitions are reversed in the level scheme.

The proposed level scheme for ^{59}Cr populated through the β decay of ^{59}V is shown in Figure 4.30. The logft values and β decay branching ratios are not shown due to the large number of decays that have not been placed into the level scheme. However, it should be noted that based on the number of β decays observed and the low intensity of the γ-ray transitions that have been placed directly feeding the ground state there is a significant β branch to the ground state of ^{59}Cr. The previous work performed on the isomeric ^{59}Cr decay established a tentative $9/2^+$ excited state at 503 keV which deexcites through an M2 γ emission [39] of 193 keV, then cascades through two γ-rays with energies of 102 and 208 keV, respectively [37]. The M2 transition from the $9/2^+$ 503-keV state suggests a J^π assignment for the 310-keV level of $5/2^-$. From the $\gamma\gamma$ coincidence spectra obtained by gating on transitions feeding the 310 keV state the efficiency corrected intensity ratio between the 102- and 208-keV transitions is approximately 60%. The discrepancy from the expected 100% can be resolved if the 102-transition is an E2 transition (E2 internal conversion coefficient $= 0.39$). This

leads to a $1/2^-$ assignment to the 208-keV level and a ground state of $3/2^-$. The previous suggestion of a $5/2^-$ ground state for ^{59}V [37] would lead to a large ground state branch in the ^{59}V $\rightarrow$ ^{59}Cr decay which is observed.

4.4.1 $\quad$ ^{59}Cr

The intensity of ^{59}V ions also allowed a study of the ^{59}Cr β decay. As mentioned above, the half-life for the ^{59}Cr β decay has been adopted as 1100 ± 100 ms following the analysis of the 1238-keV γ-gated decay curve shown in Figure 4.25. γ-coincidence spectra have also been extracted for transitions suspected to be in the daughter, ^{59}Cr, and are shown in Figure 4.31. The 662- and 1238-keV transitions were found to be in coincidence. Additionally, if the 112-keV and 1238-keV transitions were in coincidence there would be a significant peak at 112 keV in the 1238-keV $\gamma\gamma$-coincidence spectrum, which was unobserved. The statistics were too low to identify possible coincidences between the 662-keV and either the 112- or 1126-keV transitions. The level scheme for ^{59}Mn derived from the β decay of ^{59}Cr is given in Figure 4.32.
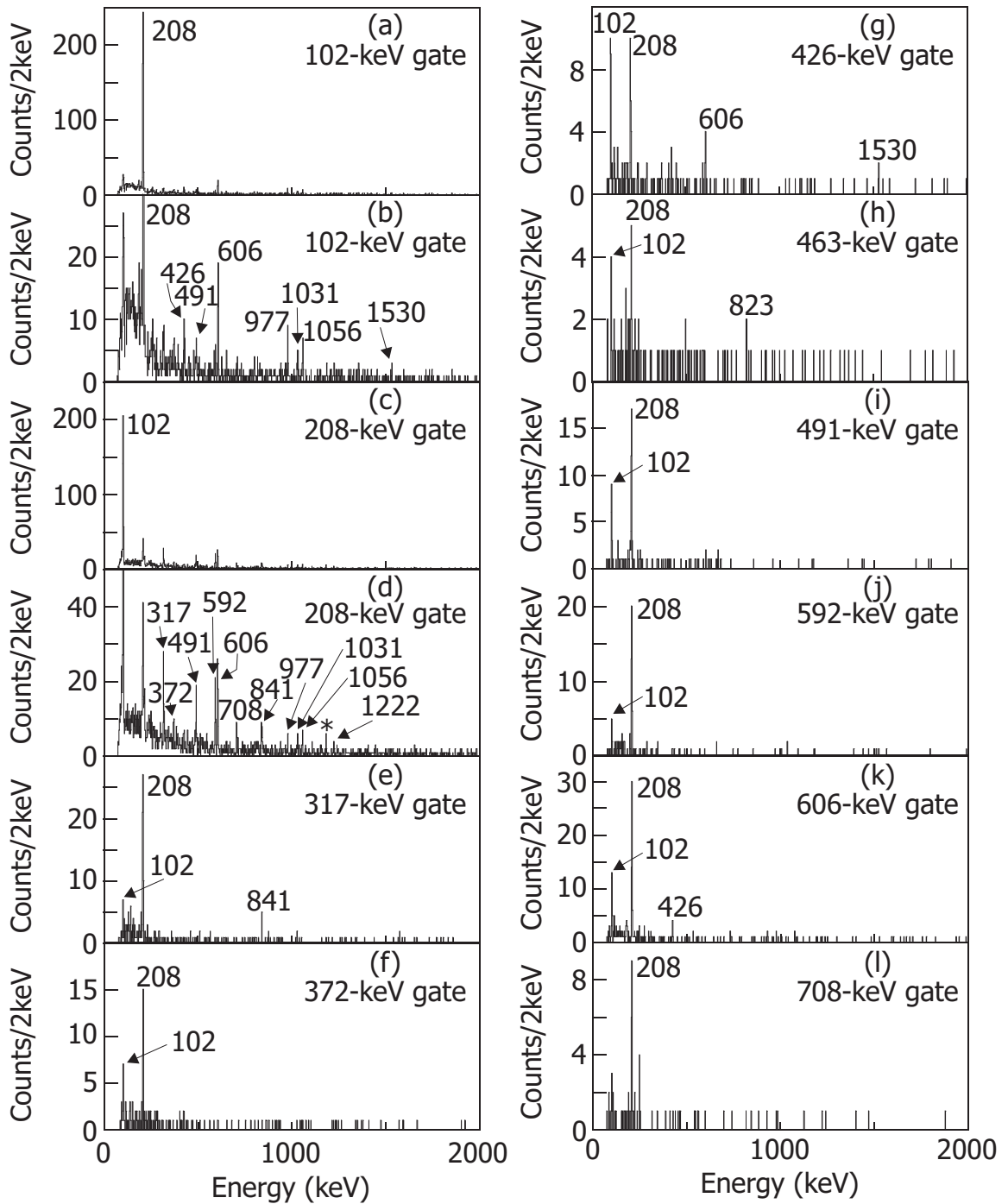
Figure 4.27: $\gamma - \gamma$ coincidence data following a ^{59}V β decay for the (a)102-, (b)102-, (c)208-, (d)208-, (e)317-, (f)372-, (g)426-, (h)463-, (i)491-, (j)592-, (k)606-, and (l)708-keV transitions.
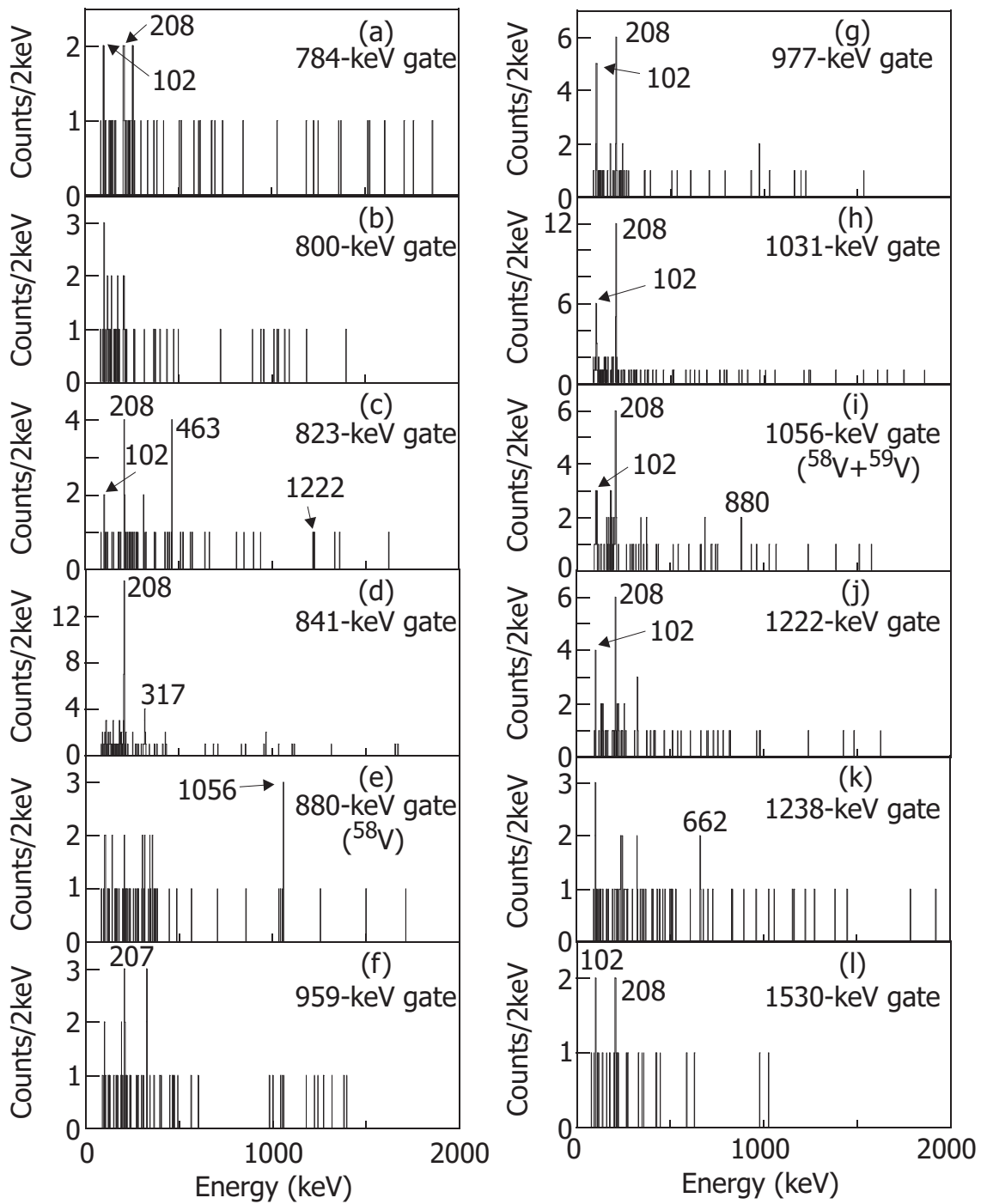
Figure 4.28: $\gamma-\gamma$ coincidence data for following a ^{59}V β decay for the (a)784-, (b)800-, (c)823-, (d)841-, (e)880-, (f)959-, (g)977-, (h)1031-, (i)1056-, (j)1222-, (k)1238-, (l)1530-keV transitions. Panel (e) and (i) contain contamination from ^{58}V due to a particle ID overlap.
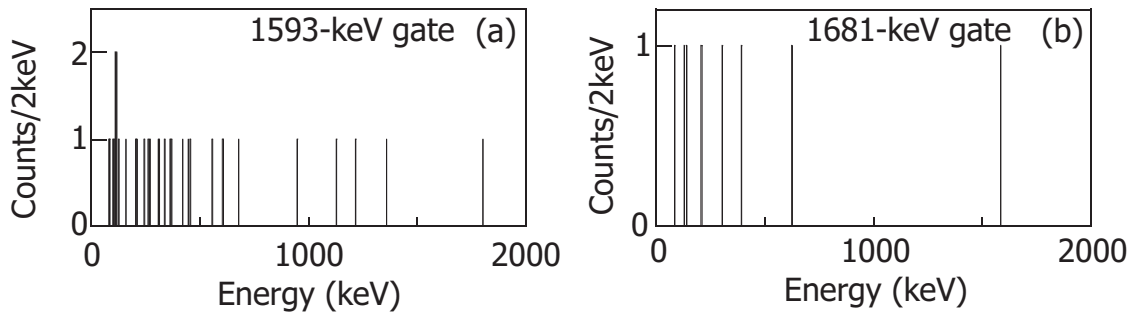
Figure 4.29: γ-γ coincidence data following a ^{59}V β decay for the (a) 1593-, (b)1681-keV transitions..

Figure 4.30: Proposed ^{59}Cr level scheme populated following the decay of ^{59}V. The number in brackets following the γ-ray decay energy is the absolute γ-ray intensity. The Q value was deduced from data in Ref. [32]. Observed coincidences are represented as filled circles.
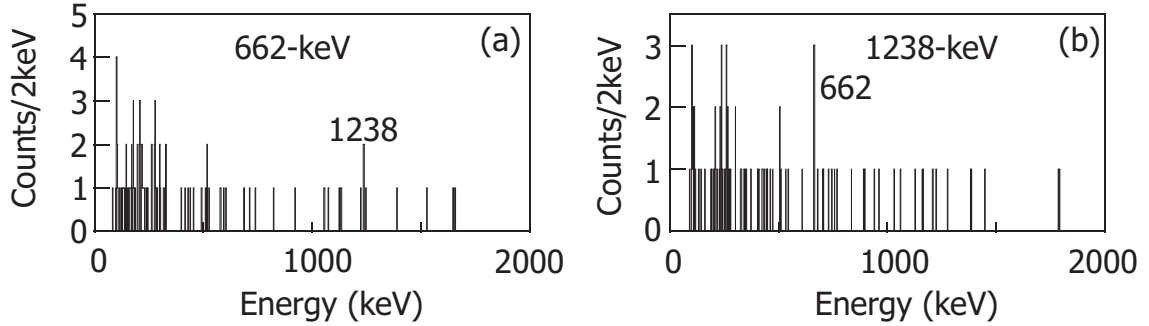
Figure 4.31: $\gamma\gamma$ coincidence spectra for two of the transitions suspected of belonging to the decay of ^{59}Cr. The 1238- and 662-keV transition are in coincidence. A coincidence between the 1238 and 112 keV transitions, if present, should be observable in the 1238-keV gated spectrum based on the intensity of the 662 keV peak. Intensities were too weak to determine coincidences between 662- and either 112- or 1126- keV transitions.
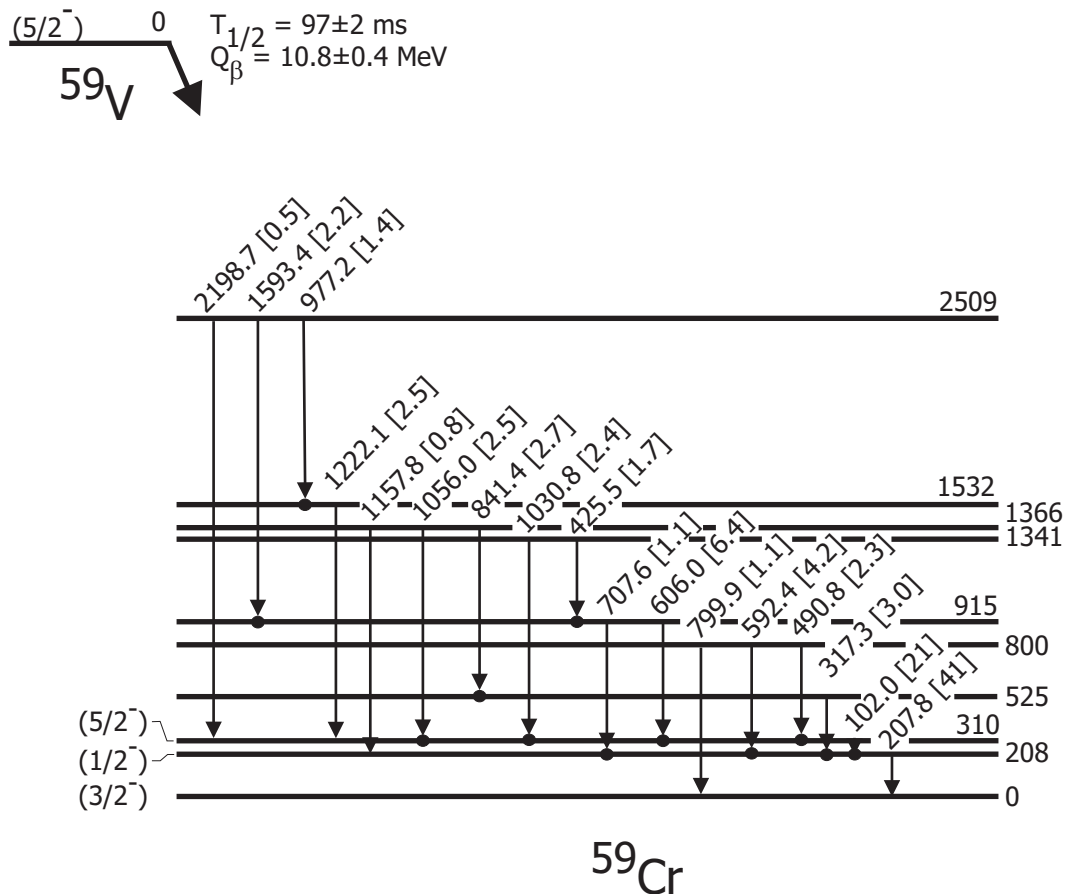

Figure 4.32: Proposed ^{59}Mn level scheme populated following the decay of ^{59}Cr. The number in brackets following the γ-ray decay energy is the relative γ-ray intensity. The Q value was deduced from data in Ref. [32]. Observed coincidences are represented as filled circles.
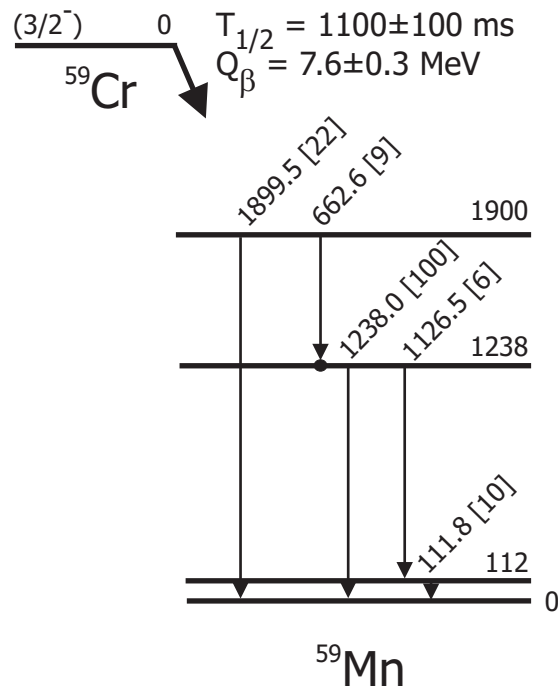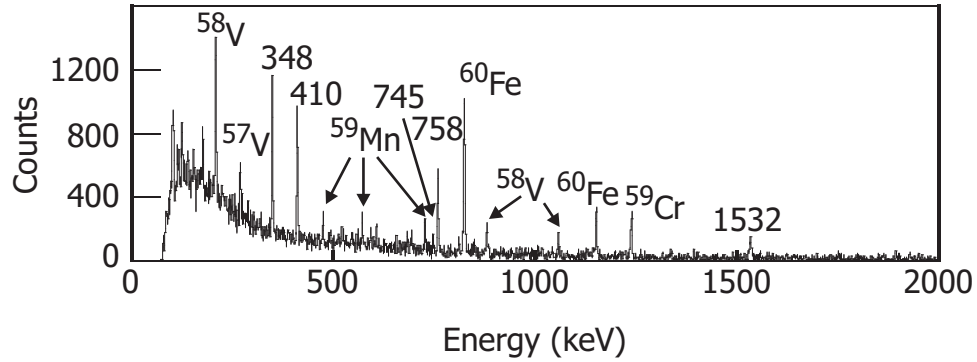
Figure 4.33: β-delayed γ-ray spectrum for those decays observed within 5 s of the implantation of a ^{60}Cr ion.

Table 4.8: ^{60}Cr β-delayed γ-rays with absolute γ-ray intensities and initial and final states for those transitions placed into the ^{60}Cr level scheme.

E(keV)	I_γ^{abs}(%)	Initial State (keV)	Final State (keV)
348.6 ± 0.4	6.4 ± 0.5	349	0
410.1 ± 0.4	5.2 ± 0.4	759	349
746.0 ± 0.6	0.9 ± 0.4		
758.2 ± 0.4	5.0 ± 0.5	759	0

4.5 ^{60}Cr

The β-delayed γ-ray spectrum for events that occurred within 5 s after a ^{60}Cr implantation event are shown in Figure 4.33. The correlation time was extended due to the longer half-life of ^{60}Cr. Observable in Figure 4.33 are numerous lines that belong to the decay of longer lived species, as seen from the $\beta\gamma$ spectra with different cuts on correlation time shown in Figure 4.34. The remaining γ rays, attributed to ^{60}Cr, are listed, along with their absolute γ-ray intensities, in Table 4.8.

The decay curve for those events that occurred within 5 s of a ^{60}Cr implantation is shown in Figure 4.35(a). From the shape of the decay curve below 1000 ms, it is apparent that the daughter, ^{60}Mn, has a shorter half-life than ^{60}Cr. Fitting the decay curve in Figure 4.35 with a parent exponential decay, an exponential growth and decay of the daughter, and a linear background, a half-life of 490 ± 10 ms for ^{60}Cr is deduced. The ^{60}Cr half-life agrees favorably with previous values of 510 ± 150 ms [42]
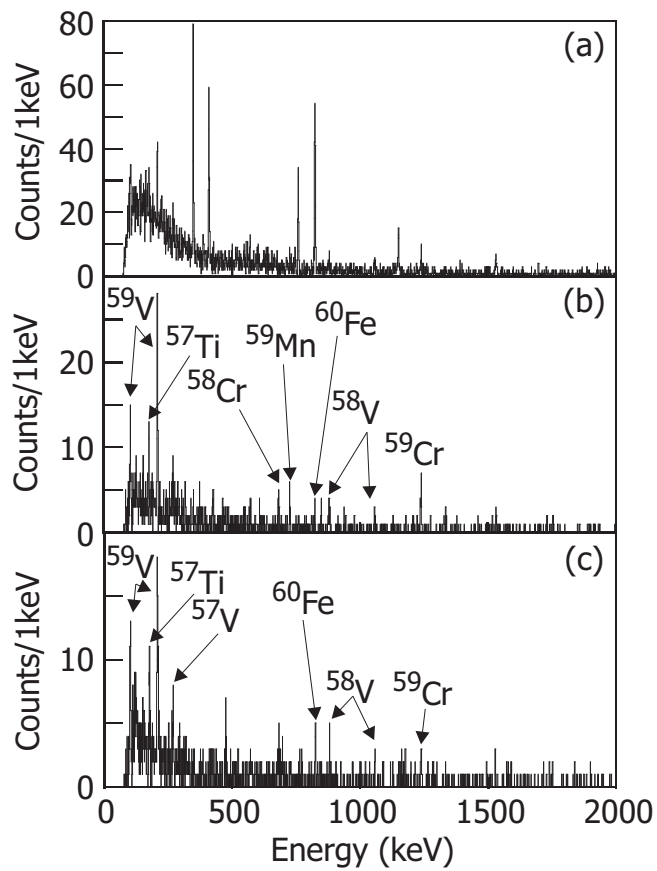
Figure 4.34: ^{60}Cr β-delayed γ spectra. β delayed γ ray spectrum for those decays observed within (a)0-1 s, (b) 4-5 s, and (c) 9-10 s following a ^{60}Cr implanted ion.

and 570 ± 60 ms [41]. The γ-gated decay curves are shown in Figures 4.35(b-d) and are consistent with the 490 ± 10ms half-life extracted from Figure 4.35(a). In the fit, the half-life of the daughter was considered a parameter, resulting in a value of 280 ± 20 ms for the ^{60}Mn half-life, in contrast to previous measurements in Refs. [41, 44, 45].

A half-life of 1.8 ± 0.1 s was deduced for a 3^+ isomeric state in ^{60}Mn at an energy of 272 keV [44, 45]. The half-life of the 0^+ ^{60}Mn ground state was first determined to be 51 ± 6 s [41] and it was suggested that the ^{60}Mn ground state β decay proceeded directly to the ^{60}Fe ground state. Later studies of ^{60}Mn suggest that 0^+ is the correct J^π assignment for the ^{60}Mn ground state but, due to contaminations from higher masses, the 51 ± 6 s half-life of ^{60}Mn is probably incorrect [46].

$\gamma\gamma$ coincidences following ^{60}Cr decay are shown in Figure 4.36. The level scheme determined from the $\gamma\gamma$ coincidence data is shown in Figure 4.37. From the absolute intensities there appears to be a large ground state branch to ^{60}Mn.

The ground state of ^{60}Cr should be 0^+. Therefore, the decay into ^{60}Mn should only populate low spin states and a significant fraction would be expected to proceed to the 0^+ ^{60}Mn ground state, which is observed. Similarly, β decay from the ^{60}Mn 0^+ ground state would be expected to populate low-spin states in ^{60}Fe. γ-ray transitions at 823 and 1150 keV match known transitions in ^{60}Fe. The 1532-keV transition could also be a transition between the second excited 0^+ at 2358 ± 3 keV and the 823 keV 2^+ state in ^{60}Fe, but such a transition has not been observed in previous β decay work. The β decay into levels of ^{60}Fe from ^{60}Mn is shown in Figure 4.38 The γ-gated decay curves for the 823-, 1150-, and 1532-keV transitions are shown in Figures 4.35(e-g). The decay curves in Figures 4.35(e,f) were fitted with an exponential daughter growth and decay, fixing the half-life of ^{60}Mn at 280ms. The resulting ^{60}Cr half-life was 450 ± 40 and 320 ± 30 for the 823- and 1150-keV transitions, respectively. It was not possible to fit the 1532-keV decay curve.
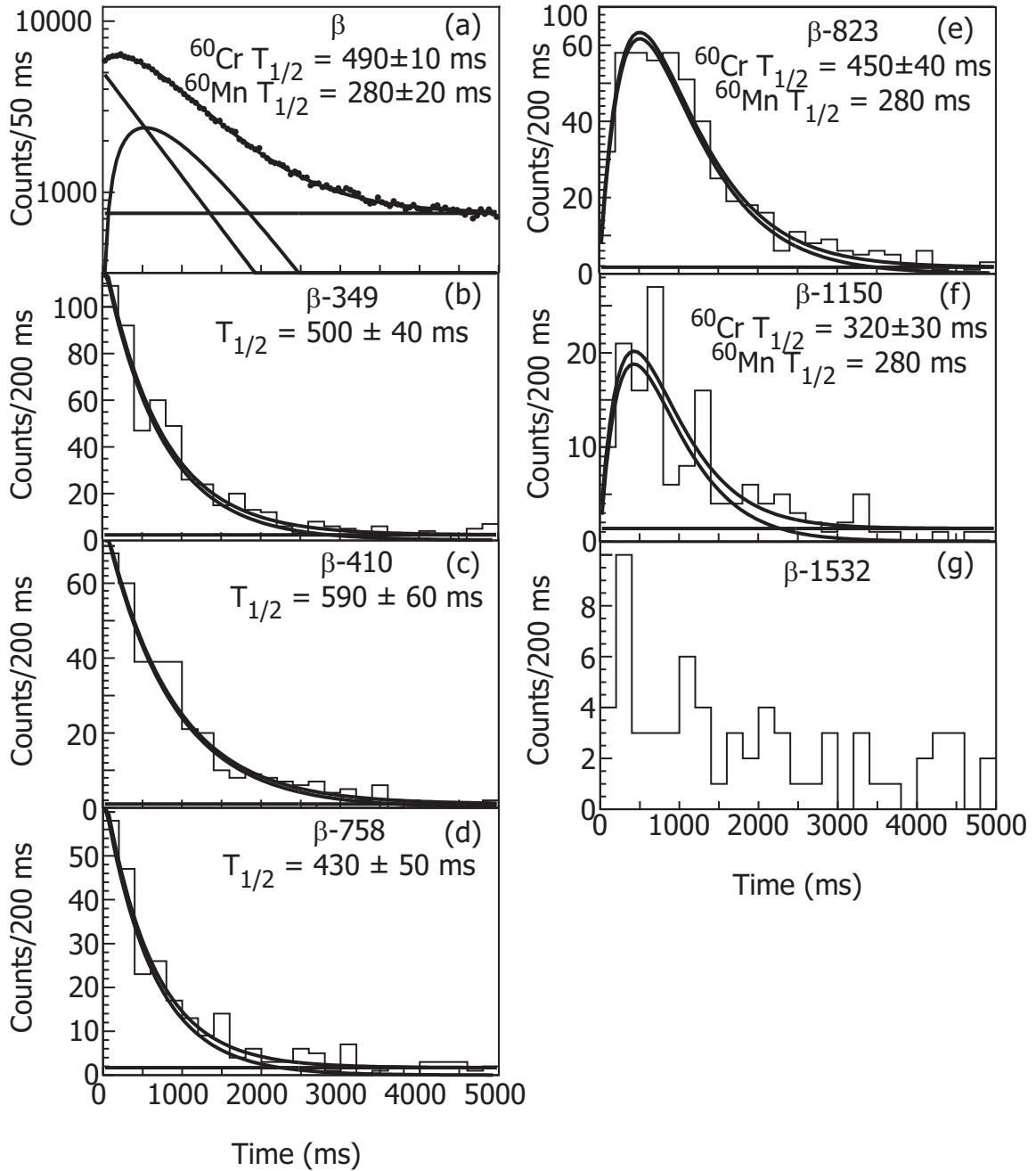
Figure 4.35: Decay curves for ^{60}Cr showing (a) fragment-β correlations where the data were fitted with an exponential parent decay, an exponential growth and decay for the daughter ^{60}Mn and a linear background, (b-d) fragment-β correlations with an additional requirement of a coincident gamma ray with an energy of (b) 349 keV, (c)410 keV and (d) 758 keV, (e-g) fragment-β correlations of transitions following the β decay of ^{60}Fe with an additional requirement of a coincident γ ray at an energy of (e) 823 keV, (f) 1150 keV, and (g) 1532 keV. Decay curves shown in (b-d) were fitted with an exponential decay and linear background. Decay curves shown in (e-f) were fitted with an exponential growth and decay and linear background.
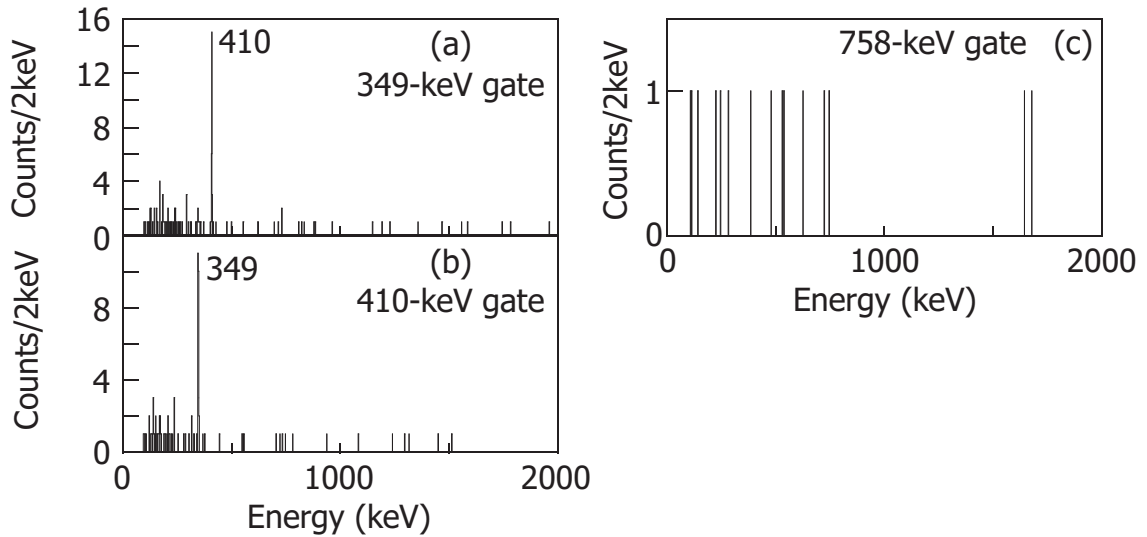
Figure 4.36: $\gamma\gamma$ coincidences for the (a)349-, (b)410-, and (c)758-keV transitions following the β decay of ^{60}Cr.
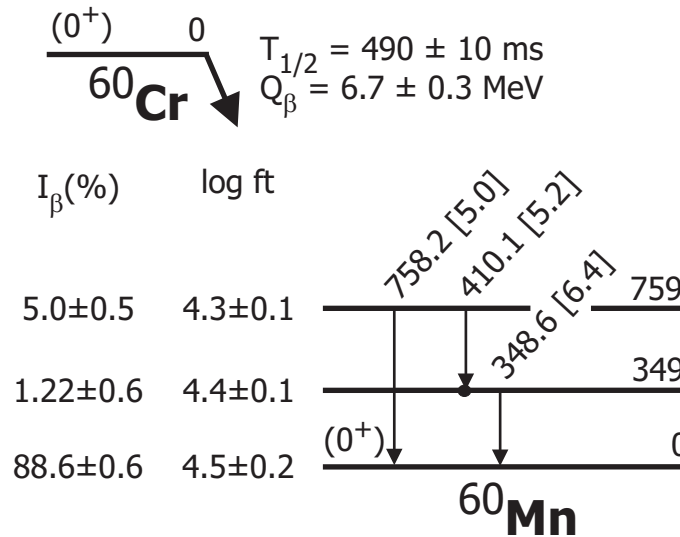
Figure 4.37: Level scheme deduced following the β decay of ^{60}Cr into excited levels in ^{60}Mn. β-decay branching ratios along with logft values calculated using Q_β from Ref. [33].
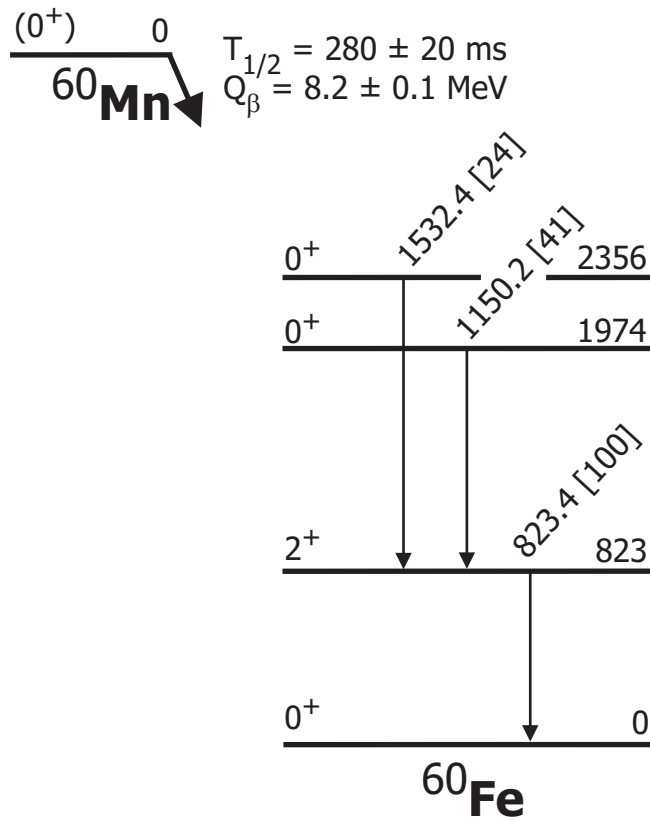
Figure 4.38: Levels in ^{60}Fe populated following the β decay of ^{60}Mn. Relative γ-ray intensities given in brackets following the γ decay energy. Q_β determined from Ref. [33].

Chapter 5

Discussion

At present, complete ab initio calculation of nuclei are only possible for the lightest nuclei, A $\leq$ 17. Beyond that the number of shell model orbitals and the amount of calculations are prohibitively large. One of the bases of shell model calculations is the presence of shell closures, allowing the computational problem to be divided into two parts; an inert core containing most of the nucleons coupled to 0^+ and a small number of valence nucleons outside the core constrained to a certain range of orbitals called the model space. The properties of the nucleus are then determined by the valence nucleons. Knowledge of the location of shell closures becomes important for the study of exotic regions of nuclei. As the locations of the traditional shell closures at 2,8,20,28,50,82, and 126 are based primarily on experiments performed with stable nuclei their extrapolation to exotic regions can be questioned. With the development of radioactive nuclear beams it has become possible to search for the appearance or disappearance of shell closures far from stability and numerous recent results suggest that shell closures, particularly in the neutron-rich region, may be dynamic [12,47–50]. A variety of different effects may result in so-called shell quenching. The proton-neutron monopole interaction discussed in the Introduction is such an effect and was already demonstrated in near-stable nuclei using the proton single-particle states in Sb (see Figure 1.3). While the monopole interaction is strong between orbits of similar
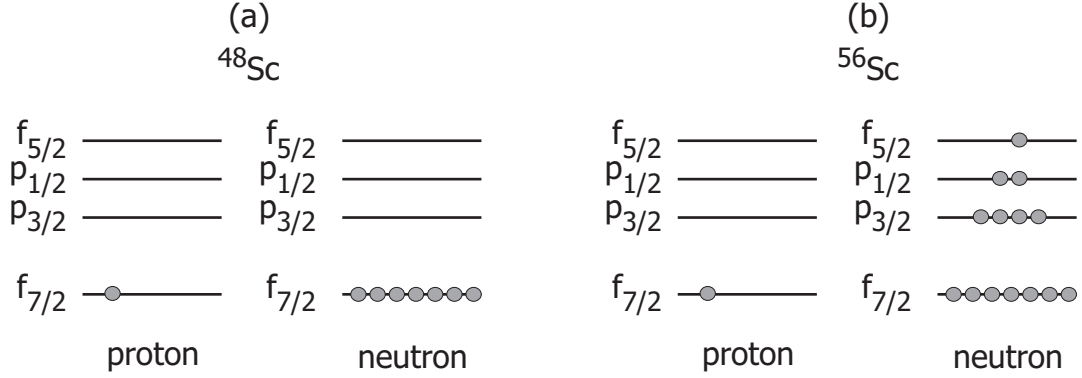
Figure 5.1: The large spin-orbit splitting prevents spin-orbit partners from being occupied simultaneously as in (a) for ^{48}Sc. Far from stability the spin-orbit partners will both be occupied, shown in (b) for ^{56}Sc, leading to strong proton-neutron monopole interactions.

l the most dramatic reordering of single-particle states should occur when the orbital angular momentum, l, is the same for both protons and neutrons [7]. Due to the large spin-orbit splitting, this condition will be satisfied in neutron-rich nuclei far from stability (see Figure 5.1). Dramatic changes in effective single-particle energies due to strongly attractive interactions between spin-orbit coupling partners has been discussed by Otsuka et $al.$ [10] in the context of the disappearing $N = 8, 20$ magic numbers for neutron-rich exotic nuclei.

The migration of the neutron effective single-particle energy due to the monopole interaction as a result of the filling of proton single-particle levels can be calculated using the equation below [51]:

$$\tilde{\varepsilon}_{j_\nu} = \varepsilon_{j_\nu} + \sum_{j_\pi} \langle j_\nu j_\pi | V_M | j_\nu j_\pi \rangle \nu_{j_\pi} \tag{5.1}$$

where $\tilde{\varepsilon}_{j_\nu}$ is the effective neutron single-particle energy, ε_{j_ν} is the 'bare' single-particle energy, and $\langle j_\nu j_\pi | V_M | j_\nu j_\pi \rangle$ is the two body interaction between protons in state j_π and neutrons in state j_ν, and ν_{j_π} is the occupancy of the proton orbit. The potential, V_M, in equation 5.1 is attractive in nature serving to lower the energy of the neutron single-particle state and is linearly dependent on the occupancies of the proton orbits. Evidence of a significant reordering in single-particle states can be seen in Figure 5.2
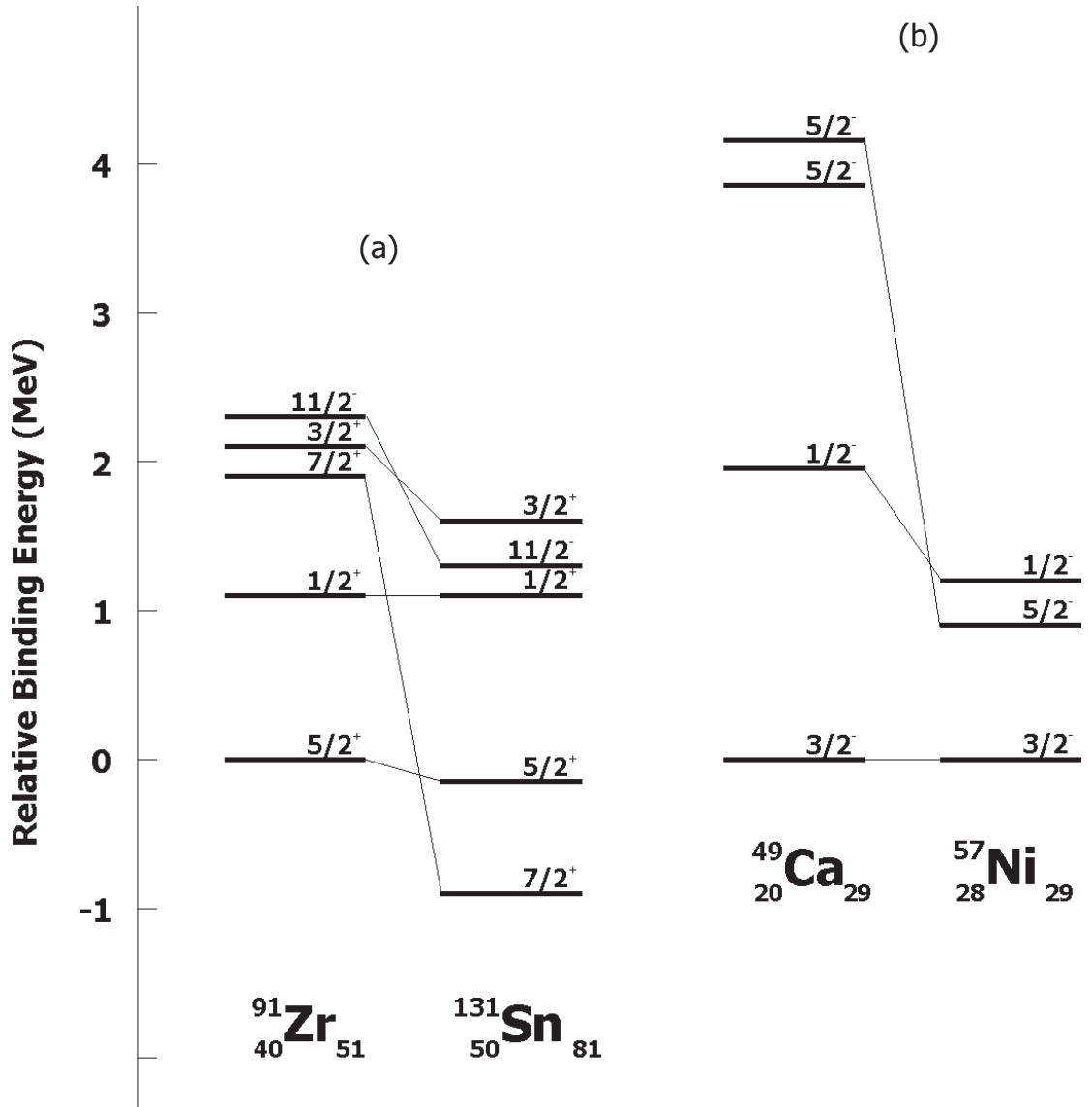
Figure 5.2: The proton-neutron monopole interaction between (a) the $\nu g_{7/2}$-$\pi g_{9/2}$ and (b) $\nu f_{5/2}$-$\pi f_{7/2}$. In both cases the reduction in energy of the neutron level resulting from the filling of the proton single-particle state is $\sim$3 MeV.

where a large drop in the energy of the $7/2^+$ state is observed as protons are added to the $g_{9/2}$ single-particle level from Zr to Sn. Information on the spectroscopic factor (S factor) provides the link between the single-particle state, $\nu g_{7/2}$, and the observed J^π of the low-energy level. The S factor describes the fraction of a particular state that is derived from a specific nuclear configuration and can vary between 0 and 1. The drop of the $7/2^+$ level observed in Figure 5.2 is attributed to the monopole interaction between the $\pi g_{9/2}$-$\nu g_{7/2}$ levels. Although the single-particle level density is high in

this mass region the drastic change in single-particle energies results in the formation of a shell gap at N = 56, evidenced by the high 2_1^+ energy in ^{96}Zr [52] compared to other Zr isotopes, that subsequently is washed out as the $\pi g_{9/2}$ state is filled, lowering the $\nu g_{7/2}$ level.

In regions of lower single-particle level density, such as the pf shells, the substantial reordering of single-particle states due to the proton-neutron monopole interaction make neutron-rich nuclei near N = 28 ideal candidates for the emergence of new shell structure. Between the Ca and Ni isotopes, as protons are added to the $f_{7/2}$ single-particle state the monopole interaction between $\pi f_{7/2}$ and $\nu f_{5/2}$ results in a decrease in the energy of the $f_{5/2}$ single-particle state, resulting in a reduced energy of the $5/2^-$ state, see Figure 5.2(b). As protons are removed from the $f_{7/2}$ single-particle level the neutron $f_{5/2}$ state increases in energy and could result in the formation of N = 32 and N = 34 subshell closures in the Ca and Ti isotopes due to the large energy separation between the $p_{3/2}$, $p_{1/2}$, and $f_{5/2}$ neutron single-particle states.

The low energy structure of the even-even neutron-rich isotopes beyond the $N = 28$ shell closure have been investigated to follow the evolution of possible new subshell closures at N = 32,34. As previously mentioned, the systematic variation of the E(2^+) in even-even nuclei gives an indication of shell closures. Along with the E(2^+) energies, the branching ratios of the β decay of the odd-odd parent into the even-even daughter allows the inference of a tentative spin and parity assignment to the parent ground state. The ground state J$^\pi$ assignments can be used to track the monopole migration of the $\nu f_{5/2}$ level as a function of protons in the $f_{7/2}$ state which can be compared to with shell model predictions to infer single-particle level ordering. With the current experimental data, the E(2^+) values for the N = 34 $_{22}$Ti and $_{24}$Cr isotopes can be compared with theoretical predictions to gauge the possible presence of an N = 34 subshell closure.
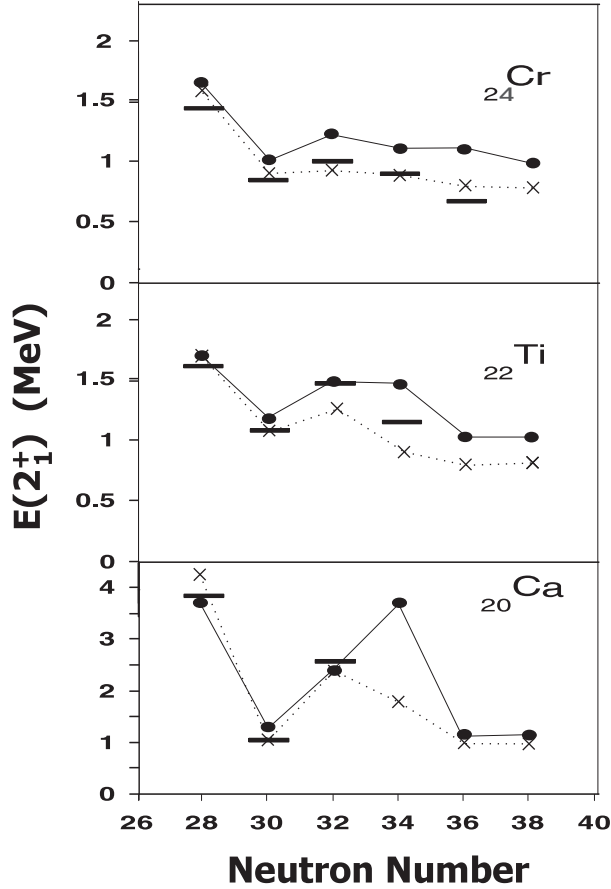
Figure 5.3: E(2^+) as a function of neutron number for the $_{24}$Cr, $_{22}$Ti, and $_{20}$Ca isotopes. The circles connected by lines represent the GXPF1 interaction. Crosses connected by lines correspond to KB3G interaction and the black bars are experimental points. GXPF1 does well at reproducing the N = 32 subshell closure in the Cr, Ti, and Ca isotopes while KB3G does not predict an N = 32 subshell closure in the Cr isotopes. GXPF1 predicts a shell closure at N = 34 in the Ti and Ca isotopes evidenced by the peak in E(2^+) values.

5.1 Comparison with Shell Model Results

Shell model calculations employing the GXPF1 [1,14] and KB3G [53] interactions are compared to the experimental energies of the first excited 2^+ state of the even-even $_{24}$Cr, $_{22}$Ti and $_{20}$Ca isotopes beyond the $N = 28$ shell closure in Figure 5.3, and were presented in Ref. [28]. The evolution of the N = 32 subshell gap, as described by the GXPF1 interaction, arises from the gradual migration of the $\nu f_{5/2}$ orbital, due to the proton-neutron monopole interaction, with the removal of protons from the $f_{7/2}$ leading to a increasing energy gap between the $\nu f_{5/2}$ and $\nu p_{3/2}$ orbitals. The widening

Figure 5.4: E(2^+) for the N = 32 isotones showing the rise in energy that is expected to parallel the increasing energy separation between the neutron $f_{5/2}$ and $p_{3/2}$ single-particle states.

energy gap between the $\nu f_{5/2}$ and $\nu p_{3/2}$ can be seen as well in the increasing energy of the E(2^+) in the N = 32 isotones as protons are removed from the nucleus, see Figure 5.4. The GXPF1 calculations also do well in reproducing the high-spin states observed in various neutron-rich Ti isotop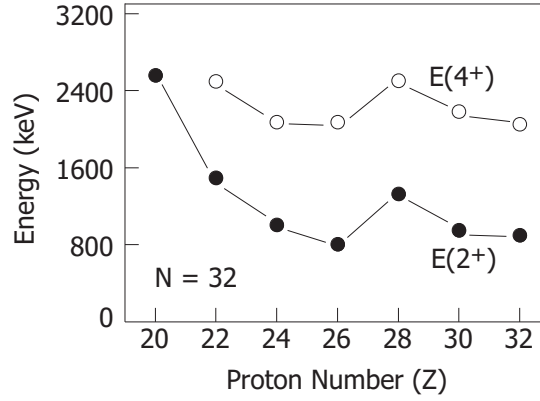es [13]. The GXPF1 and KB3G calculations diverge concerning the possible subshell closure at N = 34 in the Ti and Ca isotopes. The GXPF1 interaction predicts that as the last few protons are removed from the $f_{7/2}$ state the $\nu f_{5/2}$ single-particle state continues to increase in energy resulting in a significant energy gap between the $\nu p_{1/2}$ and $\nu f_{5/2}$ orbitals, and a new magic number at $N = 34$ for the $_{22}$Ti and $_{20}$Ca isotopes. A first indication of the subshell closure at $N = 34$ would be found in the systematic variation in $E(2^+_1)$ in Ti and Ca isotopes. Unfortunately, the energy of the 2^+ state in ^{56}Ti, only 1129 keV, does not bear out this possibility; falling midway between the GXPF1 and KB3G predictions [28].

Shell model calculations using the GXPF1 interaction were carried out and are compared to the β-decay properties of ^{56}Sc, along the lines of similar investigations for the neutron-rich V [26] and Ti [30] nuclides, and were presented in Ref. [31]. The calculations were performed using the codes OXBASH [54] and CMICHSM [55]. Both high- and low-spin β-decaying states have been observed in ^{56}Sc. The low-spin state decays primarily to the ground state of ^{56}Ti, with a measured branching ratio of $(65 \pm 13)\%$. The results of shell model calculations using the GXPF1 interaction
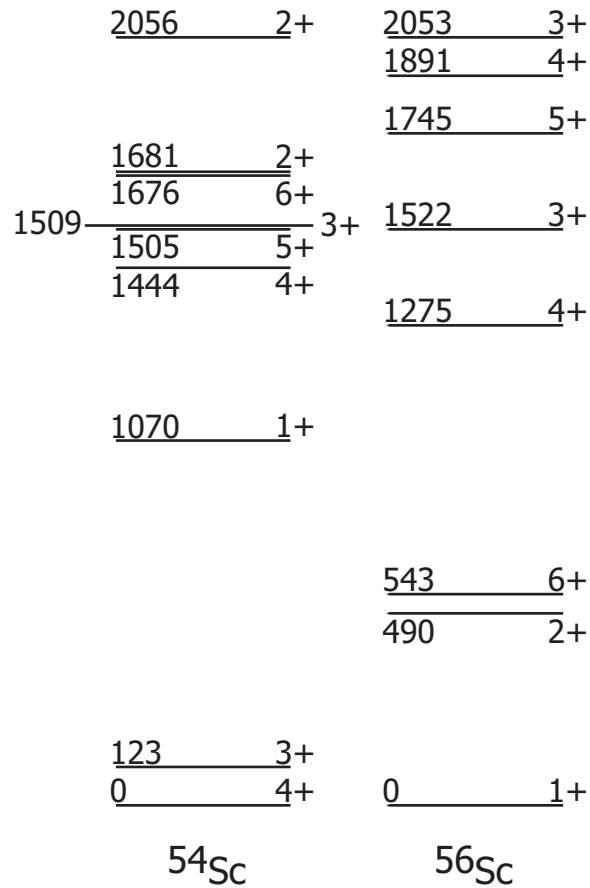
Figure 5.5: Low-energy level structure of ^{54,56}Sc from shell model calculations using the GXPF1 interaction.

predict a 42% β-branch for the ^{56}Sc 1^+ decay to the ground state of ^{56}Ti. Based on direct feeding to the first 6^+ state in the daughter ^{56}Ti, the spin and parity of the high-spin β-decaying state in ^{56}Sc has been tentatively assigned as $(6^+, 7^+)$. The shell model calculations performed predicted a 68% β-decay branching for the ^{56}Sc 6^+ decay to the first excited 6^+ state in ^{56}Ti, and this was the only direct feeding to excited states in ^{56}Ti below 4 MeV.

The calculated β-decay half-lives for the 1^+ and 6^+ states were 16 ms (35 ± 5 ms) and 110 ms (60 ± 7 ms), respectively, where the corresponding experimental numbers are given in parenthesis. For both calculations, a Q_β value of 13.7 MeV [32] was used, as the energy separation between and order of the high- and low-spin β-decaying states is unknown. The calculated half-lives were corrected by a factor of two to account for the reduction in calculated Gamow-Teller strength for neutron-rich nuclides in this region. The experimental half-lives for the two β-decaying states in ^{56}Sc fall within a factor of two of the shell model results.

The presence of two β-decaying states in ^{56}Sc can be described by studying the change in level structure between ^{54,56}Sc. The calculated low-energy level structures for odd-odd parents ^{54,56}Sc are shown in Figure 5.5. The ground state of ^{54}Sc is predicted to have spin and parity 4^+, and is separated by only 123 keV from the first excited state, which is calculated to have $J^\pi = 3^+$. A very different low-energy structure is expected for ^{56}Sc. The ground state of ^{56}Sc is predicted to have spin and parity 1^+, and a doublet of states with $J^\pi = 2^+, 6^+$ is calculated at an energy of ~ 500 keV above the ground state. The following discussion focuses on the significant changes to the low-energy structure and the β-decay properties of these nuclides that result from the addition of two neutrons in going from ^{54}Sc to ^{56}Sc.

The presence of an $E2$ isomeric transition with energy 110 keV in ^{54}Sc [31] provides an insight into the low-energy structure of the ^{54}Sc parent. The calculated position of the first 1^+ level in ^{54}Sc, which has composition $(\pi f_{7/2})^1 (\nu p_{3/2})^4 (\nu f_{5/2})^1$, compared to the ground state doublet, which is most likely $(\pi f_{7/2})^1 (\nu p_{3/2})^4 (\nu p_{1/2})^1$, furthers the

understanding of the relative position and energy separation of the $\nu f_{5/2}$ and $\nu p_{1/2}$ single-particle orbitals. If the monopole migration of the $\nu f_{5/2}$ is overestimated in the GXPF1 as suggested in Ref. [28], the 1^+ state may reside much closer to the ground state, and could give rise to the observed $E2$ isomeric transition.

^{56}Sc differs from ^{54}Sc by two neutrons, and the unpaired neutron is expected to occupy the $\nu f_{5/2}$ orbital. A 1^+ ground state is predicted for ^{56}Sc from the shell model calculations employing the GXPF1 interaction. Similar to the situation in ^{54}Sc, the separation between the $\nu f_{5/2}$ and $\nu p_{1/2}$ single-particle states is expected to be smaller than that reflected in the GXPF1 results shown in Figure 5.5. A condensed low-energy spectrum for ^{56}Sc may produce several isomers, which are observed experimentally. The three isomeric γ rays observed in ^{56}Sc have not been placed. The low statistics in the current experiment did not permit the analysis of coincidence relationships between the three γ rays. Additional data on the time evolution of each of the isomeric γ rays would also help to place these transitions in the level structure of the ^{56}Sc parent.

Calculations of the β decay of ^{57}Ti to low energy levels in ^{57}V have also been carried out using the GXPF1 interaction and compared with the ^{57}Ti $\rightarrow$ ^{57}V decay. GXPF1 calculations predicted a ground state J$^\pi$ of $5/2^-$ for ^{57}Ti with a first excited state, at 422 keV, assigned as a $1/2^-$ level. The low energy level structure of ^{57}V was also calculated, resulting in a ground state of $7/2^-$ with a $5/2^-$ excited state at an excitation energy of 95 keV. The calculated β decay of ^{57}Ti, using a $5/2^-$ ground state, to levels in ^{57}V, presented in Figure 5.6, shows a large ground state branch of 44% which compares favorably with the measured value of 54±3%. The β decay calculations also predict a significant amount of feeding to four states above 1500 keV which was also observed in the experimental level scheme. Considering that the lower detection limit for absolute intensities in the ^{57}Ti β decay was ∼0.7%, the experimental and calculated level scheme agree quite well and suggest that the ground state spin and parities of ^{57}Ti and ^{57}V are $5/2^-$ and $7/2^-$, respectively.

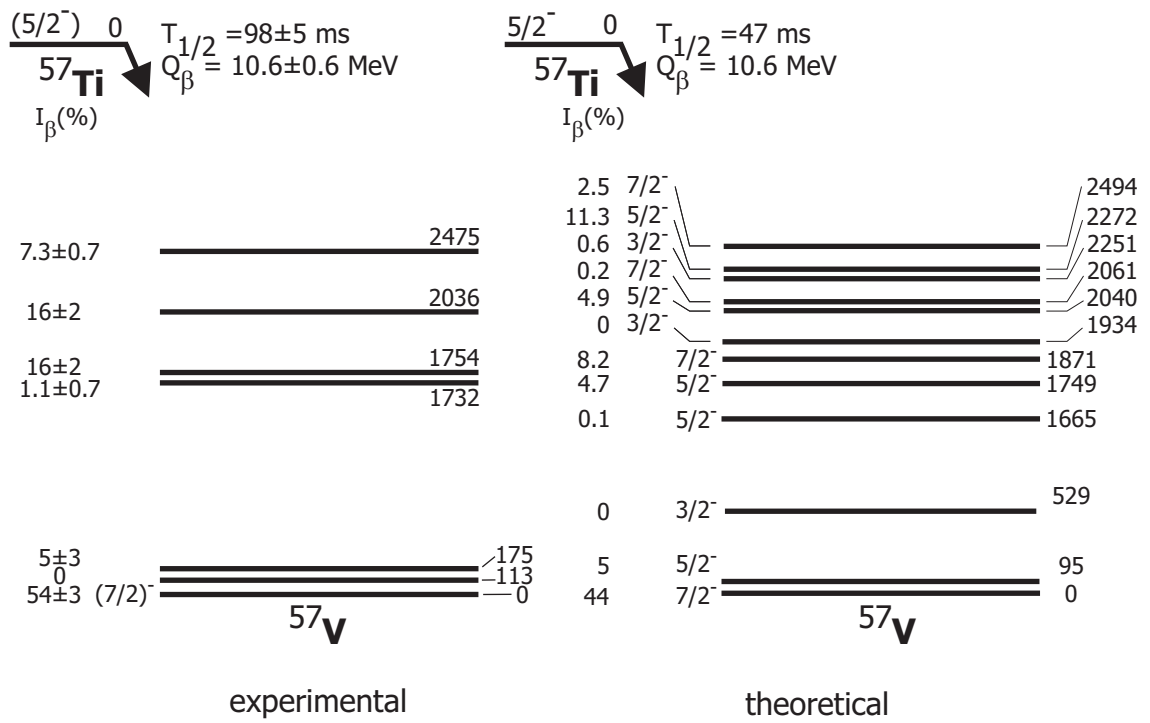Figure 5.6: The experimental decay scheme for levels in ^{57}V populated following the β decay of ^{57}Ti are shown on the left hand side of the figure. The theoretical calculations are shown on the right hand side of the figure and assume a ^{57}Ti ground state of $5/2^-$. There is overall very good agreement between the calculated and observed branching ratios, especially for the ground state branch
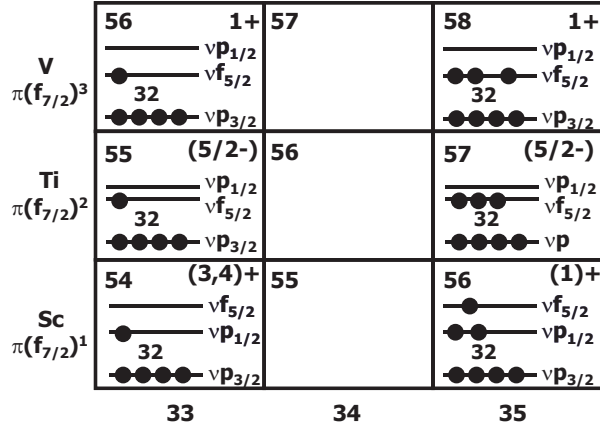
Figure 5.7: Spin and parities of odd-odd and odd-A nuclear ground states near N=32,34

A tentative $3/2^-$ ground state assignment has been previously put forward for ^{57}V based on the characteristics of the β decay into levels of ^{57}Cr [35], most importantly, a large ground state β branch of 55%. Later, the ^{57}V $\rightarrow$ ^{57}Cr ground state branch was remeasured and resulted in a value of 21% [26]. A comparison of the ^{57}V β decay characteristics with GXPF1 shell model calculations assuming a $3/2^-$, $5/2^-$, and $7/2^-$ ground state for ^{57}V found the $3/2^-$ ^{57}V ground state assignment was unable to reproduce the large ground state branch to ^{57}Cr. Calculations instead favored a $5/2^-$ or $7/2^-$ assignment to the ground state of ^{57}V, in agreement with the present tentative $7/2^-$ ^{57}V ground state.

5.2 Monopole Migration of $\nu f_{5/2}$ Based on Ground-State Spin and Parity Assignments

Using the tentative spin and parity assignments for the ^{54,56}Sc, ^{55,57}Ti, and ^{56,58}V isotopes, the monopole migration of the $\nu f_{5/2}$ state with removal of protons from the $\pi f_{7/2}$ level can be qualitatively described. The spins and parities for the ground states of Sc, Ti, and V nuclei around the $N = 32$ subshell closure, together with schematic neutron single-particle levels, are shown in Figure 5.7. Working from the N = 32

subshell closure, the extreme single-particle model was used to infer the proton and neutron orbitals that couple to produce the observed ground state spins and parities.

Starting in the $_{21}$Sc isotopes, the odd proton is located in the $\pi f_{7/2}$ state, as evidenced by the ground state spins and parities of odd-A Sc isotopes [31]. Coupling this proton to an odd neutron in the $\nu f_{5/2}$ orbital results in a range of spin and parity of (1-6)$^+$, while coupling an $f_{7/2}$ proton to an odd neutron in the $\nu p_{1/2}$ state would lead to spin and parity of 3$^+$ or 4$^+$. The ground state spin and parity of ^{54}Sc has been tentatively identified as (3,4)$^+$. Nordheim rules [56,57] argue against the coupling of a proton in the $\pi f_{7/2}$ to a neutron in the $\nu f_{5/2}$ level resulting in a (3,4)$^+$ ground state, suggesting that the 33rd neutron occupies the $\nu p_{1/2}$ orbital in agreement with shell model calculations. The tentative spin and parity of 1$^+$ in ^{56}Sc in a single-particle picture is only possible with the placement of the 35th neutron in the $\nu f_{5/2}$ level. From the schematic neutron levels, it is seen that the $\nu f_{5/2}$ level is located above the $\nu p_{1/2}$ state in the $_{21}$Sc isotopes.

In the $_{23}$V isotopes, the odd proton is still located in the $\pi f_{7/2}$ orbit. Both ^{56,58}V have been assigned 1$^+$ ground states, placing the both the 33rd and 35th neutrons in the $\nu f_{5/2}$ state and suggesting that the $\nu f_{5/2}$ orbital is lower than the $\nu p_{1/2}$ level in $_{23}$V nuclei.

The β decay of the odd-even nucleus ^{55}Ti has also been studied [30] and, while the spin and parity have not been firmly established, the complex feeding observed in the β decay of ^{55}Ti is not indicative of a dominant $\nu p_{1/2}$ single-particle configuration for the ^{55}Ti ground state. The results reported on the β decay of ^{55}Sc into the low-energy levels of ^{55}Ti suggest a significant β-decay feeding the ground state of ^{55}Ti [31]. Assuming $J = 7/2$ for the ^{55}Sc parent state, a β-decay branch directly to the daughter ground state also suggests that the ground-state spin of ^{55}Ti is greater than 1/2, limiting the J^π to (9/2, 7/2, 5/2)$^-$. In an extreme single-particle model, only a 5/2$^-$ assignment is possible by filling the odd neutron into the $f_{5/2}$ state.

The inclusion of the β decay of ^{57}Ti completes the picture. A tentative spin and

parity assignment of $5/2^-$ to the ground state is based on favorable comparisons to theoretical shell model calculations in the previous section, most importantly the large branch to the ground state of ^{57}V. In a single-particle picture, to obtain a $5/2^-$ spin and parity the odd neutron should be placed in the $f_{5/2}$ single-particle level. Thus ^{55,57}Ti suggest that the $\nu f_{5/2}$ state is lower in energy than the $\nu p_{1/2}$ state in agreement with observations in ^{55}Ti.

While the $\nu f_{5/2}$ and $\nu p_{1/2}$ single-particle level orderings, inferred from the spin and parity assignments to the ground states of odd-odd ^{54,56}Sc and ^{56,58}V isotopes, agree with shell model calculations, the present data on the low-energy levels of the neutron-rich Sc and Ti isotopes do not support a large energy separation between the $\nu f_{5/2}$ and $\nu p_{1/2}$ orbitals predicted using the GXPF1 interaction. As noted in Ref. [28], a reduction of ≈ 0.8 MeV in the single-particle energy of the $\nu f_{5/2}$ state would account for the absence of an $N = 34$ shell closure. To preserve calculated levels in other nuclei, a weaker monopole interaction should be considered to account for the slower rise in energy of the $\nu f_{5/2}$ state with the removal of protons from the $\pi f_{7/2}$ orbit [1] and a location of the first 2^+ state in ^{54}Ca around 4 MeV. However, the monopole migration of the $\nu f_{5/2}$ state is expected to continue with the removal of the last two protons from the $\pi f_{7/2}$ orbital in the $_{20}$Ca isotopes. Further investigation of the low-energy level structure of neutron-rich Ca nuclei is warranted to determine if a $\nu f_{5/2}$-$\nu p_{1/2}$ energy gap dominates at $N = 34$, resulting in a shell closure.

5.3   Summary

The β decay of (a large number) of neutron-rich nuclides was studied. The half-lives, branching ratios, and γ feeding patterns were determined for these nuclides. Among the most interesting, the low-energy levels of neutron-rich ^{56}Ti was studied through the β decay of the parent nuclide ^{56}Sc, respectively. The systematic variation in $E(2_1^+)$ for the even-even $_{22}$Ti isotopes reveal a peak at $N = 32$ indicative of a

subshell closure, similar to the increase in $E(2_1^+)$ at $N = 32$ observed for the $_{20}$Ca and $_{24}$Cr isotopes. Evidence for a shell closure at $N = 34$, predicted for the Ti isotopes by shell model calculations carried out using the new pf-shell interaction GXPF1, were not substantiated. Based on β-decay branching ratios, tentative spin and parity assignments were made for the odd-odd parent nuclei. A survey of the spin-parity assignments of the ground states of the odd-A and odd-odd nuclides in this region was used to analyze, in a schematic way, the monopole migration of the $\nu f_{5/2}$ orbital. While there is evidence that the $\nu f_{5/2} - \nu p_{1/2}$ level ordering changes between $_{23}$V and $_{21}$Sc, there is no substantial proof that a large energy gap between the $\nu f_{5/2}$ and $\nu p_{1/2}$ develops for the $_{22}$Ti isotopes. Support for this conclusion is found in the systematic variation of $E(2_1^+)$ for the even-even Ti isotopes and the presence of isomeric transitions in ^{54,56}Sc, which suggest a more compressed low-energy spectrum than predicted for these nuclides by the shell model results reported here using the GXPF1 interaction. It is important to continue to track the progression of the monopole migration to the $_{20}$Ca isotopes, which have no $f_{7/2}$ protons. The "full" monopole shift of the $\nu f_{5/2}$ orbital may lead to a large gap in the $\nu f_{5/2} - \nu p_{1/2}$ effective single particle energies, producing a shell closure at $N = 34$ for the Ca isotopes.

Chapter 6

Conclusions and Outlook

The shell structure of neutron-rich nuclei above ^{48}Ca has been investigated through the β decay of odd-odd and odd-A nuclides. Fast fragments from the NSCL facility were implanted in the DSSD and correlated with subsequent β decays on an event-by-event basis. Delayed γ rays, observed using twelve detectors from SeGA, have been observed. Half-lives and level structures were determined for ^{56}Sc, ^{57}Ti, ^{58,59}V and ^{60}Cr, representing a significant improvement in the knowledge of nuclear properties in this neutron-rich region. Tentative spin and parity assignments have been given, at a minimum, for the ground states of the studied nuclides. The possibility of an N = 34 shell closure was investigated. Shell model calculations, using the GXPF1 effective interaction, predicted that the strong proton-neutron monopole interaction between the spin-orbit partners $\pi f_{7/2}$-$\nu f_{5/2}$ would result in a gradual increase in the single-particle energy of the $\nu f_{5/2}$ level as protons were removed from the $\pi f_{7/2}$. Moreover, the rise in energy of the neutron $f_{5/2}$ would lead to the development of an N = 32 subshell closure and an N = 34 subshell closure in the Ti and Ca isotopes. While the N = 32 subshell closure has been identified experimentally, the E(2^+) value for $^{56}_{22}$Ti$_{34}$ was $\sim$400 keV lower than theoretical predictions, suggesting the absence of a subshell closure at N = 34 in the Ti isotopes. The spins and parities of the neighboring odd-odd nuclei were analyzed in an extreme single-particle framework

assuming N = 32 is a good subshell closure. The results suggest that the $f_{5/2}$ has risen in energy above the $p_{1/2}$ level as expected but there is not a large energy separation between the two orbitals to bring about a neutron subshell closure at N = 34. Further experiments on the neutron-rich Ca isotopes, in particular ^{54,56}Ca are warranted to determine if the subshell closure is present with the complete removal of protons from the $f_{7/2}$ state. However, the study of these very-neutron rich nuclides through β decay may have to wait for the next generation accelerator facility due to the extremely low production cross section. It may be possible to investigate these nuclei through Coulomb excitation or possibly deep-inelastic reactions. The monopole interaction might have a role in the evolution of shell structure in heavier neutron-rich nuclei. For example, the filling of the $\nu g_{9/2}$ level following the N = 40 subshell closure may alter the single-particle energy of the $\pi f_{5/2}$ and $\pi g_{9/2}$ states possibly affecting shell structure in the vicinity of ^{78}Ni [58]. Additionally, the proton-neutron monopole interaction between the spin-orbit partners $\pi g_{9/2} - \nu g_{7/2}$ and $\pi h_{11/2} - \nu h_{9/2}$ may affect the energy of the $\nu g_{7/2}$ and $\nu h_{9/2}$ single-particle states, disturbing the energies of the N = 82,126 shell closures [10].

Bibliography

[1] M. Honma, T. Otsuka, B.A. Brown, and T. Mizusaki. *Phys. Rev. C*, **69**:034335, 2004.

[2] http://www.nndc.bnl.gov/. .

[3] M.G. Mayers. *Phys. Rev.*, **75**:75, 1949.

[4] O. Haxel, J. Hans, D. Jensen, and H.S. Suess. *Phys. Rev.*, **75**:1776, 1949.

[5] K. S. Krane. *Introductory Nuclear Physics*. John Wiley & Sons, Inc., New York, 1988.

[6] R.A. Meyer, I. Morrison, and W.B. Walters. Proton-neutron interactions in the a = 100 nuclides. In *Exotic Nuclear Spectroscopy*. DNCT, American Chemical Society, 1990.

[7] P. Federman and S. Pittel. *Phys. Lett. B*, **69**:385, 1977.

[8] L. Grodzins. *Phys. Lett.*, **2**:88, 1962.

[9] A. Huck, G. Klotz, A. Knipper, C. Miehe, C. Richard-Serre, G. Walter, A. Poves, H.L. Ravn, and G. Marguier. *Phys. Rev. C*, **31**:2226, 1985.

[10] T. Otsuka, R. Fujimoto, Y. Utsono, B.A. Brown, M. Honma, and T. Mizusaki. *Phys. Rev. Lett.*, **87**:082502, 2001.

[11] X.L. Tu, X.G. Zhou, D.J. Vieira, J.M. Wouters, Z.Y. Zhou, H.L. Seifert, and V.G. Lind. *Z. Phys. A*, **337**:361, 1990.

[12] J.I. Prisciandaro, P.F. Mantica, B.A. Brown, D.W. Anthony, M.W.Cooper, A. Garcia, D.E. Groh, A. Komives, P.A. Lofy, A.M. Oros-Peusquens, S.L. Tabor, and M.Wiedeking. *Phys. Lett. B*, **510**:17, 2001.

[13] R.V.F. Janssens, B. Fornal, P.F. Mantica, B.A. Brown, R. Broda, P. Bhattacharyya, M.P. Carpenter, M. Cinausero, P.J. Daly, A.D. Davies, T. Glasmacher, Z.W. Grabowski, D.E. Groh, M. Honma, F.G. Kondev, W. Krolas, T. Lauritsen, S.N. Liddick, S. Lunardi, N. Marginean, T. Mizusaki, D. Seweryniak, H. Schatz, A. Stolz, S.L. Tabor, C.A.Ur, G. Viesti, I. Wiedenhover, and J. Wrzesinski. *Phys. Lett. B*, **546**:55, 2002.

[14] M. Honma, T. Otsuka, B.A. Brown, and T. Mizusaki. *Phys. Rev. C*, **65**:061301R, 2002.

[15] T. Glasmacher. *Annu. Rev. Nucl. Part. Sci.*, **48**:1, 1998.

[16] P.G. Hansen and J.A. Tostevin. *Annu. Rev. Nucl. Part. Sci.*, **53**:219, 2003.

[17] Q.R. Ahmad and SNO Collaboration. *Phys. Rev. Lett.*, **89**:011301, 2002.

[18] Y. Fukuda and Super Kamiokande Collaboration. *Phys. Rev. Lett.*, **81**:1562, 1998.

[19] S. S. M. Wong. *Introductory Nuclear Physics.* John Wiley & Sons, Inc., New York, 1998.

[20] G. Friedlander, J. W. Kennedy, E. S. Macias, and J. M. Miller. *Nuclear and Radiochemistry, 3rd ed.* John Wiley & Sons, Inc., New York, 1981.

[21] D. J. Morrissey, B.M. Sherrill, M. Steiner, A. Stolz, and I. Wiedenhoever. **204**:90, 2003.

[22] W. F. Mueller, J.A. Church, T. Glasmacher, D. Gutknecht, G. Hackman, P.G. Hansen, Z. Hu, K.L. Miller, and P. Quirin. *Nucl. Instr. and Meth. A*, **466**:492, 2001.

[23] J.I. Prisciandaro. *Beta Decay Studies of ^{69}Ni and ^{58}V: Development of subshell gaps within the N = 28 - 50 shell.* PhD thesis, Michigan State University, 2001.

[24] J.I. Prisciandaro, A.C. Morton, , and P.F. Mantica. *Nucl. Instr. and Meth. A*, **505**:140, 2003.

[25] G. F. Knoll. *Radiation Detection and Measurement.* John Wiley & Sons, Inc., New York, 2000.

[26] P.F. Mantica, A.C. Morton, B.A. Brown, A.D. Davies, T. Glasmacher, D.E. Groh, S.N. Liddick, D.J. Morrissey, W.F. Mueller, H. Schatz, A. Stolz, S.L. Tabor, M. Honma, M. Horoi, and T. Otsuka. *Phys. Rev. C*, **67**:014311, 2003.

[27] W.T. Milner. Oak Ridge National Laboratory, unpublished.

[28] S. N. Liddick, P.F. Mantica, R.V.F Janssens, R. Broda, B.A. Brown, M.P. Carpenter, B. Fornal, M. Honma, T. Mizusaki, A.C. Morton, W.F. Mueller, T. Otsuka, J. Pavan, A. Stolz, S.L.Tabor, B.E. Tomlin, and M. Wiedeking. *Phys. Rev. Lett.*, **92**:072502, 2004.

[29] B. Fornal, S. Zhu, R.V.F. Janssnes, M. Honma, R. Broda, P.F. Mantica, B.A. Brown, M.P. Carpenter, P.J. Daly, S.J. Freeman, Z.W. Grabowski, N. Hammond, F.G. Kondev, W. Królas, T. Lauritsen, S.N. Liddick, C.J. Lister, E.F. Moore, T. Otsuka, T.Pawlat, D. Seweryniak, B.E. Tomlin, and J. Wrzesiński. *Phys. Rev. C*, (in press).

[30] P. F. Mantica, B.A. Brown, A.D. Davies, T. Glasmacher, D.E. Groh M. Horoi, S.N. Liddick, D.J. Morrissey, A.C. Morton, W.F. Mueller, H. Schatz, A. Stolz, and S.L.Tabor. *Phys. Rev. C*, **68**:044311, 2003.

[31] S. N. Liddick, P.F. Mantica, R. Broda, B.A. Brown, M.P. Carpenter, A.D. Davies, B. Fornal, T. Glasmacher, D.E. Groh M. Honma, M. Horoi, R.V.F. Janssens, T. Mizusaki, D.J. Morrissey, A.C. Morton, W.F. Mueller, T. Otsuka, J. Pavan, H. Schatz, A. Stolz, S.L.Tabor, B.E. Tomlin, and M. Wiedeking. *Phys. Rev. C*, (in press).

[32] G. Audi and A. H. Wapstra. *Nucl. Phys. A*, **595**:409, 1995.

[33] G. Audi, A. H. Wapstra, and C. Thibault. *Nucl. Phys. A*, **729**:337, 2003.

[34] P. Möller, J.R. Mix, and K.-L. Kratz. *At. Data and Nucl. Data Tables*, **66**:131, 1997.

[35] O. Sorlin, V. Borrel, S. Grévy, D. Guilemaud-Mueller, A.C. Mueller, F. Pougheon, W. Böhmer, K.-L. Kratz, T. Mehren, P. Möller, B. Pfeiffer, T. Rauscher, M.G. Saint-Laurent, R. Anne, M. Lewitowicz, A. Ostrowski, T. Dörfler, and W.-D. Schmidt-Ott. *Nucl. Phys. A*, **632**:205, 1998.

[36] F. Ameil, M. Bernas, P. Armbruster, S.Czajkowski, Ph. Dessangne, H. Geissel, E. Hanelt, C. Kozhuharov, C. Mieha, C. Donzaud, A. Grewe, A. Heinz, Z. Janas, M. de Jong, W. Schwab, and S. Steinhäuser. *Eur. Phys. J. A*, **1**:275, 1998.

[37] O. Sorlin, C. Donzaud, L. Axelsson, M. Belleguic, R. Béraud, C. Borcea, G. Canchel, E. Chabanat, J.M. Daugas, A. Emsallem, M. Girod, D. Guilemaud-Mueller, K.-L. Kratz, S. Leenhardt, M. Lewitowicz, C. Longour, M.J. Lopez, F. de Oliveria Santos, L. Peitzon, B. Pfeiffer, F. Pougheon, M.G. Saint-Laurent, and J.E. Sauvestre. *Nucl. Phys. A*, **669**:351, 2000.

[38] T. Dörfler, W.-D. Schmidt-Ott, T. Hild, T. Mehren, W. Böhmer, P. Möller, P. Pfeiffer, T. Rauscher, K.-L. Kratz, O. Sorlin, V. Borrel, S.Grévy, D. Guillemand-Mueller, A.C. Mueller, F. Pougheon, R. Anne, M. Lewitowicz, A. Ostrowsky, M. Robinson, and M.G. Saint-Laurent. *Phys. Rev. C*, **54**:2894, 1996.

[39] R. Grzywacz, R. Beraud, C. Borcea, A.Emsallem, M. Glogowski, H. Grawe, D. Guillemaud-Mueller, M. Hjorth-Jensen, M.Houry, M. Lewitowicz, A.C. Mueller, A. Nowak, A. Plochocki, M. Pfu:tzner, K. Rykaczewski, M.G. Saint-Laurent, J.E. Sauvestre, M. Schaefer, O. Sorlin, J. Szerypo, W. Trinder, S. Viteritti, and J. Winfield. *Phys. Rev. Lett.*, **81**:766, 1998.

[40] U. Bosch, W.-D. Schmidt-Ott, P. Tidemand-Petersson, E. Runte, W. Hillebrandt, M. Lechle, F.-K. Thielemann, R. Kirchner, O. Klepper, E. Roeckl, K. Rykaczewski, D. Schardt, N. Kaffrell, M. Bernas, Ph. Dessagne, and W.Kurcewicz. *Nucl. Phys. A*, **164**:22, 1985.

[41] U. Bosch, W.-D. Schmidt-Ott, E. Runte, P. Tidemand-Petersson, P. Koschel, F. Meissner, R. Kirchner, O. Klepper, E. Roeckl, K. Rykaczewski, and D. Schardt. *Nucl. Phys. A*, **477**:89, 1988.

[42] T. Dörfler. *Phys. Rev.*, **120**:927, 1996.

[43] S.J. Freeman, R.V.F. Janssens, B.A. Brown, M.P. Carpenter, S.M. Fisher, N.J. Hammond, M. Honma, T. Lauritsen, C.J. Lister, T.L. Khoo, G. Mukherjee, D. Seweryniak, J.F. Smith, B.J. Varley, M. Whitehead, and S. Zhu. *Phys. Rev. C*, **69**:064301, 2004.

[44] E.B. Norman, C.N. Davids, M.J. Murphy, and R.C. Pardo. *Phys. Rev. C*, **17**:2176, 1978.

[45] E. Runte, K.-L. Gippert, W.D. Schmidt-Ott, P. TidemandPertersson, L. Ziegeler, R. Kirchner, O. Klepper, P.O. Larsson, E. Roeckl, D. Schardt, N. Kaffrell, P.Peuser, M. Bernas, P. Dessagne, M. Langevin, and K. Rykaczewski. *Nucl. Phys. A*, **441**:237, 1985.

[46] W.-D. Schmidt-Ott, K.Becker, U. Bosh-Wicke, T. Hild, F. Meissner, R.Kirchner, E.Roeckl, and K. Rykaczewski. *Inst. Phys. Conf. Ser.*, **132**:627, 1992.

[47] H. Simon, D. Aleksandrov, T. Aumann, L. Axelsson, T. Baumann, M.J.G. Borge, L.V. Chulkov, R. Collatz, J. Cub, W. Dostal, B. Eberlein, Th.W. Elze, H. Emling, H. Geissel, A. Grunschloss, M. Hellström, J. Holeczek, R. Holzmann, B. Jonson, J.V. Kratz, G. Kraus, R. Kulessa, Y. Leifels, A. Leistenchneider, T. Leth, I. Mukha, G. Mu:nzenburg, F. Nickel, T. Nilsson, G. Nyman, B. Petersen, M. Pfützner, A. Richter, K. Riisager, C. Scheidenberger, G. Schrieder, W. Schawb, M.H.Smedberg, J. Stroth, A. Surowiec, O. Tengblab, and M.V. Zhukov. *Phys. Rev. Lett.*, **83**:496, 1999.

[48] T. Motobayashi, Y. Ikeda, Y. Ando, K. Ieki, M. Inoue, N. Iwasa, T. Kikuchi, M. Kurokawa, S. Moriya, S. Ogawa, H. Murakami, S. Shimoura, Y. Yanagisawa, T. Nakamura, Y. Watanabe, M. Ishihara, T. Teranishi, H. Okuno, and R.F. Casten. *Phys. Lett. B*, **346**:9, 1995.

[49] D. Guillemaud-Mueller, C. Detraz, M. Langevin, F. Naulin, M. De Saint-Simon, C. Thibault, F.Touchard, and M. Epherre. *Nucl. Phys. A*, **426**:37, 1984.

[50] A. Ozawa, T. Kobayashi, T. Suzuki, K. Yoshida, and I. Tanihata. *Phys. Rev. Lett.*, **84**:5493, 2000.

[51] K. Heyde, J. Jolie, J. Moreau, J. Ryckebusch, and M. Waroquier. *Nucl. Phys. A*, **466**:189, 1987.

[52] Table of Isotopes. edited by R.B. Firestone. Wiley, New York, 1996.

[53] A. Poves, J. Sanchex-Solano, E. Caurier, and F. Nowacki. *Nucl. Phys. A*, **694**:157, 2001.

[54] B.A. Brown, A. Etchegoyen, and W.D.M. Rae. The computer code oxbash. MSU-NSCL Report 524, MSU-NSCL, 1998.

[55] M. Horoi, B.A. Brown, and V. Zelevinsky. *Phys. Rev. C*, **67**:034303, 2003.

[56] L. Nordeim. *Rev. Mod. Phys.*, **23**:322, 1951.

[57] M.H. Brennan and A.M. Bernstein. *Phys. Rev.*, **120**:927, 1960.

[58] A.M. Oros-Peusquens and P.F. Mantica. *Nucl. Phys. A*, **669**:81, 2000.